(2)

STRENGTHENING OF NiAl MATRIX COMPOSITES

ANNUAL REPORT

OF

N00014-91-J-1353

FROM

OFFICE OF NAVAL RESEARCH

PREPARED BY
R.J.ARSENAULT
METALLURGICAL MATERIALS LABORATORY
UNIVERSITY OF MARYLAND
COLLEGE PARK, MARYLAND

October 1991

SECURITY CLASSIFICATION OF THIS PAGE

REPORT DOCUMENTATION PAGE

1a. REPORT SECURITY CLASSIFICATION: Unclassified	1b. RESTRICTIVE MARKINGS
2a. SECURITY CLASSIFICATION AUTHORITY	3. DISTRIBUTION/AVAILABILITY OF REPORT
2b. DECLASSIFICATION/DOWNGRADING SCHEDULE	
4. PERFORMING ORGANIZATION REPORT NUMBER(S): MML-1991-1	5. MONITORING ORGANIZATION REPORT NUMBER(S)
6a. NAME OF PERFORMING ORGANIZATION: University of Maryland; 6b. OFFICE SYMBOL (If applicable)	7a. NAME OF MONITORING ORGANIZATION
6c. ADDRESS (City, State and ZIP Code): Dept. of Mat. & Nuclear Engr. University of Maryland College Park, MD 20742	7b. ADDRESS (City, State and ZIP Code)
8a. NAME OF FUNDING/SPONSORING ORGANIZATION: Office of Naval Research; 8b. OFFICE SYMBOL (If applicable)	9. PROCUREMENT INSTRUMENT IDENTIFICATION NUMBER
8c. ADDRESS (City, State and ZIP Code): Office of Naval Research Code 1131 S Arlington, VA	10. SOURCE OF FUNDING NOS.

PROGRAM ELEMENT NO.	PROJECT NO.	TASK NO.	WORK UNIT NO
			4311 875

11. TITLE (Include Security Classification): Strengthening of NiAl Matrix Composites

12. PERSONAL AUTHOR(S): Richard J. Arsenault

13a. TYPE OF REPORT	13b. TIME COVERED	14. DATE OF REPORT (Yr., Mo., Day)	15. PAGE COUNT
Annual	FROM Oct. 1990 TO Sep. 1991	1991 Oct.	

16. SUPPLEMENTARY NOTATION

17. COSATI CODES			18. SUBJECT TERMS (Continue on reverse if necessary and identify by block number)
FIELD	GROUP	SUB. GR	Intermetallic Matrix Composites TiB_2/NiAl

19. ABSTRACT (Continue on reverse if necessary and identify by block number)

Deformation of TiB_2/NiAl composites at high temperatures exhibit low temperature deformation characteristics, and grain size refinement in these composites could account for the strengthening of the composites.

Interfaces of TiB_2-NiAl and α-Al_2O_3-NiAl in TiB_2/NiAl composites have been investigated by analytical electron microscopy. Although no consistent crystallographic orientation relationships have been found between NiAl and TiB_2 or Al_2O_3, semicoherent interfaces between α-Al_2O_3 and NiAl have been observed by HREM in areas where the low indexed crystallographic planes of α-Al_2O_3 aligned with that of NiAl. No semicoherent interfaces between NiAl and TiB_2 have been observed. Silicon segregation was consistently detected by EDS at the TiB_2/NiAl interface region. Segregation has not been detected in the α-Al_2O_3-NiAl interface region. The segregation layer observed at the TiB_2-NiAl interface is too thin to absorb any of the thermal residual stress.

20. DISTRIBUTION/AVAILABILITY OF ABSTRACT	21. ABSTRACT SECURITY CLASSIFICATION
UNCLASSIFIED/UNLIMITED ☒ SAME AS RPT. ☐ DTIC USERS ☐	

22a. NAME OF RESPONSIBLE INDIVIDUAL	22b. TELEPHONE NUMBER (Include Area Code)	22c. OFFICE SYMBOL
Dr. S.G. Fishman	703-696-4401	ONR/1131S

DD FORM 1473, 83 APR EDITION OF 1 JAN 73 IS OBSOLETE.

Unclassified
SECURITY CLASSIFICATION OF THIS PAGE

Statement A per telecon
Dr. Steven Fishman
ONR/Code 1131
Arlington, VA 22207-5000
NWW 10/29/91

A-1

TABLE OF CONTENTS

MICROSTRUCTURE OF TiB_2/NiAl
L.Wang and R.J.Arsenault
Mater.Sci.Eng., A127, 1990,91.

DISLOCATIONS IN TITANIUM DIBORIDE
L.Wang and R.J.Arsenault
Phil.Mag., 63, 1991, 121.

LOCALIZED DEFORMATION OF SiC/Al COMPOSITES
R.J.Arsenault,N.Shi, C.R.Feng and L.Wang
Mater.Sci.Eng.A 131, 1991, 55.

STRENGTHENING OF COMPOSITES DUE TO MICROSTRUCTURAL CHANGES IN THE MATRIX
R.J.Arsenault.L.Wang and C.R.Feng
Acta Metall. 39, 1991,47.

THE FRACTURE MODE IN SiC/Al COMPOSITES
S.B.Wu and R.J.Arsenault
Mater.Sci.Eng., A138, 1991, 227

ANALYTICAL EVALUATION OF THE THERMAL RESIDUAL STRESS IN SiC/Al COMPOSITES
N.Shi and R.J.Arsenault
JSME, International Journal, 34 (1991), 143

I. SUMMARY

The high-temperature deformation behavior of TiB_2/NiAl composites were investigated through the measurement and analyses of the thermal activation parameters of the deformation process, such as the activation volume, the apparent activation energy, and the temperature dependence of yield stress. The stress exponent, n, and the apparent activation energies for deformation of TiB_2/NiAl composites are functions of stress, and volume fractions of the reinforcements. These apparent activation energies are considerably higher than that for self-diffusion in NiAl. Also, it strongly appears that the deformation process is not controlled by diffusion. However it may be assisted by diffusion. The yield stress strongly depends on the temperature for all 0, 10, and 20 V% TiB_2/NiAl composite, in the temperature range of 703-1273 K. A 20 V% TiB_2/NiAl composites is about two and a half times stronger than a 0 V% TiB_2/NiAl. Activation volumes of deformation in the temperature range of 813-1273 K for TiB_2/NiAl composites are similar to that of monolithic NiAl and resembles the low-temperature behavior of b.c.c. metals. Deformation of TiB_2/NiAl composites at 765 to 1273 K exhibit low-temperature characteristics, and grain size refinement in these composites could account for the strengthening of the composites.

Interfaces of TiB_2-NiAl and α-Al_2O_3-NiAl in TiB_2/NiAl composites have been investigated by analytical electron

microscopy. Although no consistent crystallographic orientation relationships have been found between NiAl and TiB_2 or Al_2O_3, semicoherent interfaces between α-Al_2O_3 and NiAl have been observed by HREM in areas where the low indexed crystallographic planes of α-Al_2O_3 aligned with that of NIAl. No semicoherent interfaces between NiAl and TiB_2 have been observed. Silicon segregation was consistently detected by EDS at the TiB_2/NiAl interface region. Segregation has not been detected in the α-Al_2O_3-NiAl interface region. The segregation layer observed at the TiB_2-NiAl interface is too thin to absorb any of the thermal residual stress.

II. LIST OF PUBLICATIONS AND PRESENTATIONS

1. Papers Published and Submitted

   1. Microstructure of TiB_2/NiAl
      L.Wang and R.J.Arsenault
      Mater.Sci.Eng., A127, 1990,91.

   2. Dislocations in Titanium Diboride
      L.Wang and R.J.Arsenault
      Phil.Mag., 63, 1991, 121.

   3. Localized Deformation of SiC/Al Composites
      R.J.Arsenault,N.Shi, C.R.Feng and L.Wang
      Mater.Sci.Eng.A 131, 1991, 55.

   4. Strengthening of Composites Due to Microstructural CHANGES IN THE MATRIX
      R.J.Arsenault.L.Wang and C.R.Feng
      Acta Metall. 39, 1991,47.

   5. The Fracture Mode in SiC/Al Composites
      S.B.Wu and R.J.Arsenault
      Mater.Sci.Eng., A138, 1991, 227

6. Analytical Evaluation of the Thermal Residual Stress in SiC/Al Composites
N.Shi and R.J.Arsenault
JSME, International Journal, 34 (1991), 143

7. Interfaces in XD^{TM} Processed TiB_2/NiAl Composites
Accepted for publication in Metall. Trans.

8. Comments on Miller and Humphrey's Paper
Accepted for publication in Scripta Metall.

9. A FEM Study of the Deformation Process of SiC/Al Composites
N.Shi, R.J.Arsenault and B.Wilner
Submitted for publication

10. Strengthening of Composites Due to Microstructural Changes in the Matrix
Book Title: Proceedings of the China-MRS International '90

11. Mechanical Properties of Discontinuous Metal Matrix Composites
R.J.Arsenault, N.Shi, C.R.Feng and L.Wang
Book Title: Proceedings of the American Society for Composites, 1990

12. Deformation Mechanisms and the Dislocation Structure of TiB_2/NiAl Composites
L.Wang and R.J.Arsenault
Book Title: The 8th International Conference on Composites
Materials, 1991. Ed. by S.Tasi and G.W.Springer SAMPE 21.A2

13. Strengthening and Deformation Mechanisms in SiC/Al Composites
L.Wang, N.Shi and R.J.Arsenault
Book Title: The 8th International Conference on Composite Materials, 1991, Ed. by S.Tasi and G.Springer SAMPE 25-A

14. Microstructural Changes in Metal Matrix Composites Due the Reinforcement
R.J.Arsenault, L.Wang and C.R.Feng
Book Title: Advances in Composite Materials, Ed.by P. Ramakrishnan, Oxford & IBH Publishing Co. New Delbi, 1991, 359.

15. Strengthening of NiAl by TiB_2

L.Wang and R.J.Arsenault
Book Title: Advance High Temperature Composites
Ed. by M.Gungor

16. The Dislocation Structure and Deformation Mechanisms of TiB_2/NiAl Composites
L.Wang and R.J.Arsenault
MRS 213, 1991, 1063

17. Plasticity of SiC/Al Composites
N.Shi and R.J.Arsenault
Ed. by G.Haritos, ASME

18. Microstructural Changes in Metal Matrix Composites Due to the Reinforcement
R.J.Arsenault, L.Wang and C.R.Feng
Advances in Composite Materials, Ed. by P.Ramakrishnan, Oxford & IBH Publishing, New Delhi, 1991, p.359.

19. Intermetallic Matrix Composites
Advanced Structural Inorganic Composites, Ed. by P.Vincenzini, Elsevier, 1991, p.675

20. The Strengthening and Deformation of Mechanisms of Discontinuous Metal Matrix composites
The 9th International Conference on the Strength of Metals and Alloys, 1991, Ed. by D.G Brandon, R.Chaim and A.Rosen, Freund Publishing House, LTD. London, p.31.

2. Presentations

1. ASM/TMS Fall Meeting, 1990, "An Overview of the Mechanical Properties of Discontinuous Metal Matrix Composites"

2. Japan Institute of Metals, 1990, "The Strengthening Mechanisms of Discontinuous Metal Matrix Composites"

3. University of Utah, 1991, "Interfaces in IMC"

4. The 9th International Conference on Strength of Metals and Alloys, 1991 (Plenary speaker), "The Strengthening and Deformation Mechanisms of Discontinuous Metal Matrix Composites"

5. Burgess Memorial Lecture, 1991, "Strengthening and Deformation Mechanisms in Metal Matrix Composites"

6. 8th ICCM, 1991, "Strengthening and Deformation Mechanisms of TiB_2/NiAl Composites"
L.Wang and R.J.Arsenault

7. 8th ICCM, 1991, "Strengthening and Deformation Mechanisms of SiC/Al Composites"
L.Wang, N.Shi and R.J.Arsenault

III. PUBLICATIONS

Materials Science and Engineering, A127 (1990) 91–98

Microstructure of TiB_2–NiAl

L. WANG and R. J. ARSENAULT

Metallurgical Materials Laboratory, University of Maryland, College Park, MD 20742 (U.S.A.)

Received September 15, 1989; in revised form December 4, 1989

Abstract

The addition of 20 vol.% titanium diboride in particulate form (1–3 μm) to nickel aluminide (TiB_2–NiAl) results in a twofold increase in the high temperature strength of NiAl. There are at least two theories that have been proposed to account for the high temperature strength of discontinuous reinforced metal matrix composites. However, they cannot be adequately used as a basis to explain the observed strengthening.

An investigation was undertaken of NiAl, 10vol.%TiB_2–NiAl and 20vol.%TiB_2–NiAl in the annealed condition and after deformation, allowed to cool slowly. There is a low dislocation density in the annealed samples and the dislocation density did increase slightly as a result of deformation. However, deformation did produce some intriguing dislocation arrangements; for example, it was found that there was a high dislocation density within the TiB_2 in the deformed higher volume fraction composites and the dislocation density within the NiAl matrix was not uniform.

1. Introduction

1.1. Background

The interest in intermetallic compounds for high temperature applications extends back in time for a number of years [1] and there has been a continued interest since then [2–26]. There are numerous obvious advantages for the consideration of aluminides and silicides, *e.g.* they have good oxidation resistance at high temperatures. However, they are not widely used in structural applications, but they are (*e.g.* NiAl) used as coatings on superalloys for oxidation resistance. The reason that NiAl is not used in high temperature structural applications is that its strength is at least a factor of 10 weaker than conventional superalloys. For example, at 1300 K and a strain rate of 10^{-5} s^{-1} the stress required for UDIMET 115 [27] is about 200 MPa whereas for NiAl it is less than 20 MPa [26].

Another deterrent to the use of NiAl in structural applications is its lack of ductility, especially in the large grain size condition [13]. The fracture toughness as measured by Charpy impact testing is about 0.08 ft lb (0.1 J) [28]. It was assumed that the fracture toughness of SiC measured by Charpy impact testing was low, but in that case the fracture toughness is 1 ft lb [29].

The lack of high temperature strength and the low temperature ductility can probably be improved by the addition of TiB_2, *i.e.* to produce a discontinuous composite of TiB_2–NiAl. The major advantage of TiB_2 is that it is inert with respect to the NiAl matrix [30], and in high temperature applications the matrix should not react with the reinforcement. If a reaction takes place, it is possible that reinforcement will be consumed during the reaction.

1.2. Mechanism or mechanisms of strengthening

The high temperature creep of composites as an indication of their high temperature strength has been analyzed in terms of a classical continuum composite-strengthening mechanism [31]. Simply, this means that there is a reduction of the stress in the matrix owing to the load transfer to the reinforcement. However, if these mechanisms are applied to a discontinuous spherical reinforcement, the load transfer is very small, *i.e.* 5%, which would mean that the predicted decrease in the creep rate of the spherical reinforced composite would be very small compared with that of the matrix material.

If one attempted to perform a more rigorous analysis by the use of the Eshelby method, there is a restriction which is presently placed on the Eshelby method which requires that the matrix has to be treated as a newtonian fluid, *i.e.* the stress exponent n would have to be unity. The

0921-5093/90/$3.50

observed stress exponents are much greater than unity, *i.e.* in the range 5–20 [32].

Another approach would be to consider the dislocation mechanisms that have been proposed to predict creep behavior. However, very few detailed mechanisms have been proposed which take into account the presence of large second-phase particles [32, 33].

From a consideration of a dislocation climb over second-phase particles, it is possible to obtain the following equation [32] for the creep rate:

$$\frac{\dot{\varepsilon}}{D} = \frac{(1+\nu)^{2/3}}{2.83\pi} \frac{\lambda^{-2/3} b^{-2/3} E \rho_m}{r^2 kT} \left(\frac{\sigma_c}{E}\right)^{5/3} \times \frac{1}{1-(1+\nu)^{4/3}(\lambda/b)^{4/3}(\sigma_c/E)^{4/3}} \quad (1)$$

where D is the diffusion coefficient for the matrix, ν is Poisson's ratio, λ is the interparticle spacing, E is the Young modulus of the matrix, ρ_m is the density of mobile dislocations, σ_c is the effective climb stress, b is the Burgers vector, r is the radius of the particle, k is Boltzmann's constant and T is the temperature. If it is assumed that the second phase is approximately spherical, then there is a simple relationship [33] between λ and r:

$$\lambda = 0.306 r \left(\frac{\pi}{V_f}\right)^{1/2} \quad (2)$$

where V_f is the volume fraction of the reinforcement. As one would guess intuitively, for a constant V_f, $\dot{\varepsilon}/D$ is greater for a larger size reinforcement and decreases with an increase in the volume fraction of reinforcement. If the actual $\dot{\varepsilon}$ *vs.* σ_c is determined for a composite of 20 vol.% and particles of radius 0.5 μm in the NiAl matrix, then eqn. (1) predicts a stress of less than 6.9×10^{-3} MPa for an $\dot{\varepsilon}$ of 10^{-7} s^{-1}. This stress is at least three orders of magnitude smaller than the strength of the matrix. There are other possible dislocation models which have been proposed by Blum and Reppich [33], but the result is that if the Orowan stress is low for the composite, the effect of the reinforcement on the creep rate is small.

There have been a few transmission electron microscopy (TEM) investigations of dislocations overcoming large particles at high temperatures, but details of the rate-controlling mechanisms are not given [34].

It can be concluded that there is a large difference in the predicted high temperature strengths, *i.e.* as manifested by the creep rates of discontinuous composites as predicted by the continuum mechanics and dislocation models. If we consider the preliminary data obtained, there is approximately a factor-of-2 increase of the strength of the composite (20 vol.%) *vs.* the matrix.

The purpose of this investigation was to determine the microstructures of TiB_2–NiAl samples which were deformed at high temperatures, and from these determinations to obtain some insight into the possible strengthening mechanism.

2. Materials

The materials used in this investigation were purchased from the Martin Marietta Corporation and consisted of 0, 10 and 20 vol.% TiB_2 in NiAl. The materials were ground into compression samples with a height-to-diameter (h/d) ratio of 1.5–2, which were then compression tested at 1140 and 1300 K to various strain levels. The samples were also annealed at the test temperature for periods of time from 2 to 12 h.

3. Testing methods

The samples were tested in compression at various strain rates ranging from 10^{-4} to 10^{-2} s^{-1} at 1140 and 1300 K. A decision was made to deform the samples well past initial yielding, since if there was a substantial increase in dislocation density, the assumption was made that there would be a greater chance of retaining this higher density, because at the completion of testing the

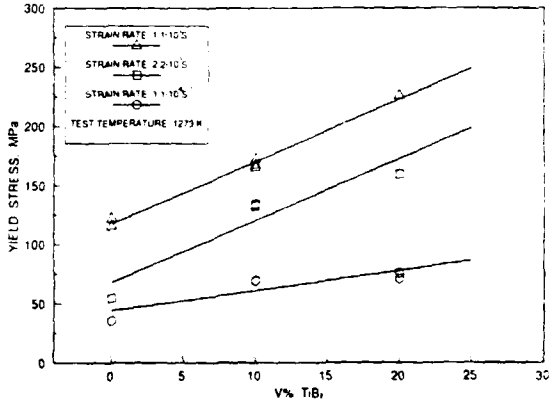

Fig. 1. The yield stress at 1000 °C (1273 K) of TiB_2–NiAl composites as a function of strain rate and volume fraction of TiB_2–NiAl sample.

samples were not cooled rapidly; *i.e.* they were cooled over a 15 min period and not in a time frame of less than 2 min [35].

After compression testing and/or after annealing, the samples were cut into 3 mm discs with a thickness of 0.5 mm by electrical discharge machining. After lightly grinding to remove the debris on the surface, the discs were dimple ground until the thickness reached 0.07–0.1 mm in the center. The final electropolishing was performed using 5% perchloric acid–ethanol solution at 253 K or below until a small hole appeared at the center of the sample. The applied voltage was 50–70 V.

An investigation was also carried out both optically and by scanning electron microscopy (SEM) to determine the particle size and distribution. This was then followed by an X-ray powder diffraction investigation to determine the content of TiB_2.

The TEM was carried out at the high voltage electron microscopy (HVEM) facility at Argonne National Laboratory.

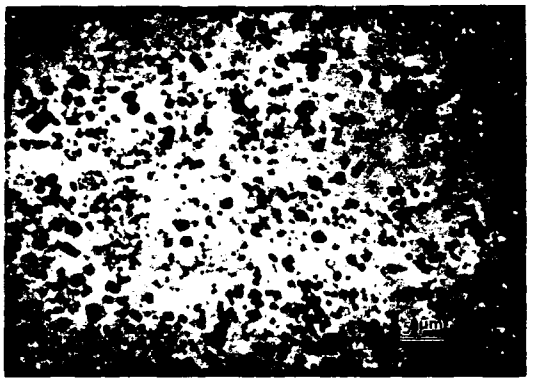

Fig. 2. SEM micrograph of a 20vol.%TiB_2–NiAl sample.

4. Experimental results and discussion

The yield stress σ_y, which is only slightly less than the ultimate stress, was determined as a function of volume fraction of TiB_2 and strain rate. As expected, σ_y increases with increasing volume fraction (Fig. 1) and increasing strain rate. However, the increase in σ_y with increasing volume fraction of TiB_2 is greater at faster strain rates.

Figure 2 is an SEM micrograph of a 20vol.%-TiB_2–NiAl sample. There are particles other than TiB_2 and these have been tentatively identified as α-Al_2O_3 from an examination of TEM selected area diffraction patterns. The dark particles in Fig. 2 are TiB_2 and the light particles (α-Al_2O_3)

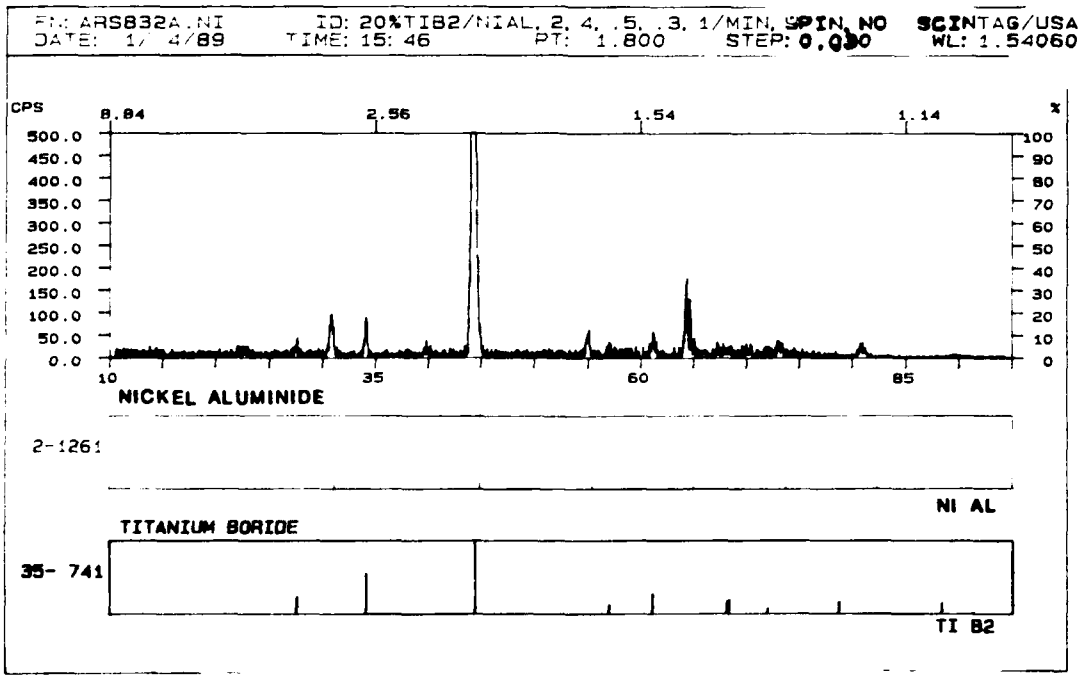

Fig. 3. X-ray powder diffraction pattern obtained from a 20vol.%TiB_2–NiAl powder sample.

can constitute as high as 10 vol.%. Figure 3 is an X-ray powder diffraction pattern obtained from a 20% TiB_2 powder sample. The purpose of the X-ray investigation was to obtain some insight as to what were in the SEM micrographs, *i.e.* an attempt to determine the nature of the other particles.

Figures 4 and 5 are TEM micrographs of 0 vol.% samples deformed 30% at 1143 K (870 °C). It is evident that the second-phase particles are acting as barriers to dislocation motion. Figures 6 and 7 are again of 0vol.%TiB_2–NiAl matrix samples and show the formation of a network which is prevalent in these alloys. It is also evident that the dislocation structure is not planar, *i.e.* there is no well-defined slip plane, and the dislocations have convoluted shapes as shown in Fig. 8. This result agrees with the observations on crept single-crystal NiAl [36].

Another phenomenon which is only observed in 0 vol.% NiAl matrix samples, especially those which were deformed at higher strain rates, are bands or regions of very high dislocation density

Fig. 4. TEM micrograph of a 0vol.%TiB_2–NiAl sample, 30% deformed, most of the dislocation having a Burgers vector of $a[100]$.

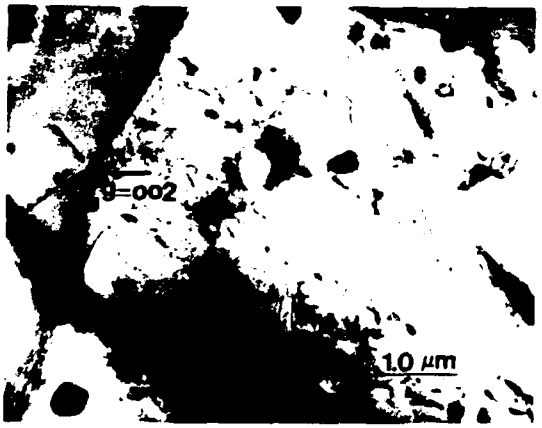

Fig. 5. TEM micrograph of a 0vol.%TiB_2–NiAl sample, 30% deformed, most of the dislocation having a Burgers vector of $a[100]$.

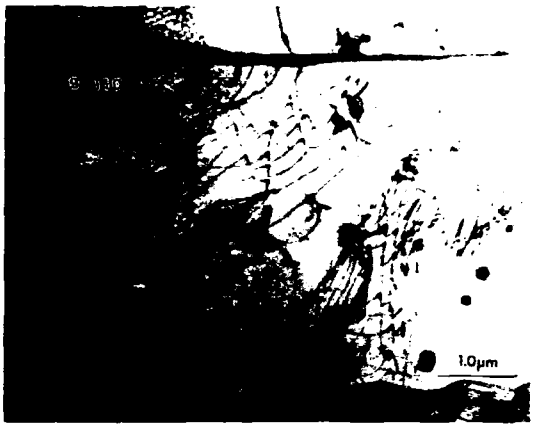

Fig. 6. TEM micrograph of a 0vol.%TiB_2–NiAl sample, 30% deformed. Networks formed by reactions of $[100]+[010]=[110]$ and $[010]+[001]=[011]$.

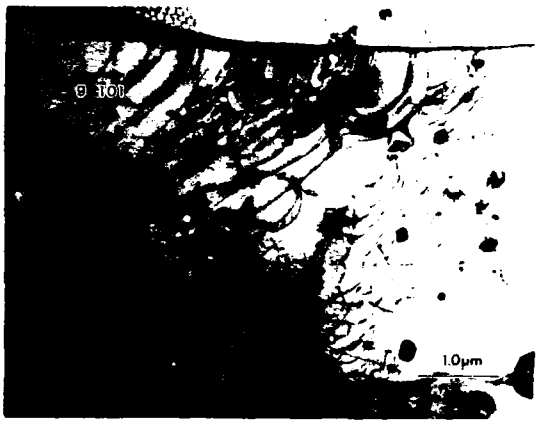

Fig. 7. TEM micrograph of a 0vol.%TiB_2–NiAl sample, 30% deformed. Networks formed by reactions of $[100]+[010]=[110]$ and $[010]+[001]=[011]$.

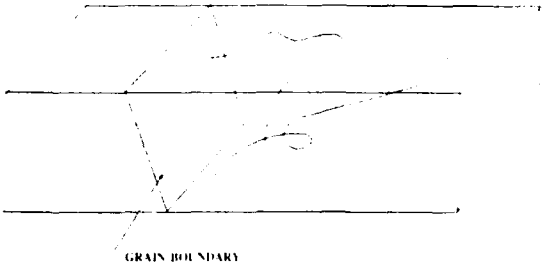

Fig. 8. Schematic illustration for convoluted shape dislocations.

which we define as shear bands. They could be the same type of bands which were observed [36] in crept single-crystal NiAl by using surface replicas. Figure 9 is an example of these shear bands in a sample which was deformed at 1140 K. The shear bands appear to go straight across the grain boundary without any apparent shifting of the grain boundary or of the shear band.

If we now consider the samples containing TiB_2 particulate, several things become evident. Figure 10 is a low magnification TEM micrograph of 20vol.%TiB_2–NiAl which was deformed 30%. There is a very high dislocation density in the area with higher than average volume fraction of TiB_2, whereas in regions of lower than average TiB_2 concentration there is a very low dislocation density. Also, it is evident in these pictures that within the TiB_2 there are a large number of dislocations.

This difference in dislocation density which depends upon the local volume fraction of TiB_2 is evident in Figs. 11 and 12 where there are two different localized volume fractions of TiB_2. Figure 11 contains a very high dislocation density in the matrix whereas in Fig. 12 there is a very low dislocation density in the matrix.

It is generally observed that there are localized regions of high dislocations in the deformed (10–20)vol.%TiB_2–NiAl composites. However, if the average dislocation density is considered, then for the composite the dislocation density is less than the average dislocation density in the deformed 0vol.%TiB_2–NiAl matrix material.

Returning to a consideration of the plastic deformation which occurs in the TiB_2, there are several unique observations as shown in Figs. 13 and 14. First, the TiB_2 particles are not uniformly deformed in all cases. Secondly, in the TiB_2 particles which contain a variable dislocation density there is a variable dislocation density in the surrounding matrix. There is an inverse relationship: if a portion of a particle has a high dislocation density, then the dislocation density in the matrix immediately surrounding this portion of the particle has a low dislocation density; if a portion of the particle has a low dislocation density, then the

Fig. 9. TEM micrograph of a 0vol.%TiB_2–NiAl sample, 30% deformed. Shear bond structure.

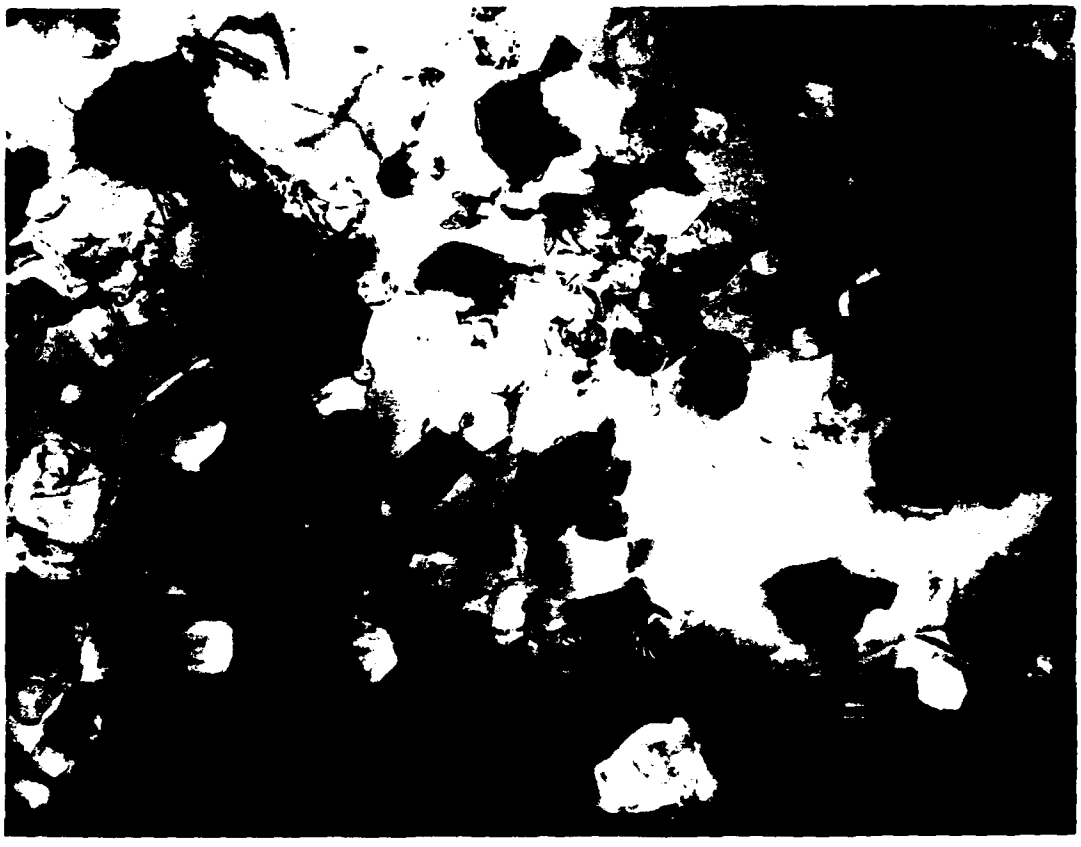

Fig. 10. TEM micrograph of a 20vol.%TiB_2–NiAl sample. 30% deformed.

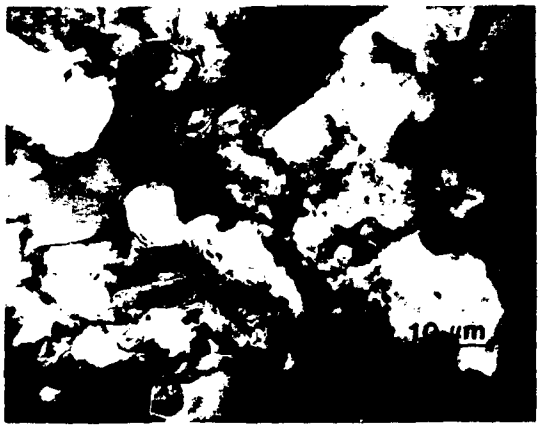

Fig. 11. TEM micrograph of a 20vol.%TiB_2–NiAl sample. 30% deformed. Highly concentrated TiB_2 area.

Fig. 12. TEM micrograph of a 20vol.%TiB_2–NiAl sample. 30% deformed. Low concentration of TiB_2.

matrix immediately surrounding this portion of the particle has a high dislocation density.

As stated in the introduction, the purpose of this investigation was to determine the changes in microstructure of TiB_2–NiAl composites deformed at high temperatures for the purpose of obtaining insight into possible strengthening mechanisms in this composite. The results obtained do not appear to support any of the presently proposed mechanisms. The theories of

Fig. 13. TEM micrograph of a 20vol.%TiB_2–NiAl sample, 30% deformed. Non-uniformly deformed TiB_2 particles. Deformed matrix always in contact with dislocation-free end of TiB_2 particle.

Fig. 14. TEM micrograph of the same area as in Fig. 13, except deformed end of TiB_2 particle with a practically dislocation-free area surrounding matrix.

Taya and Lilholt [31] which are based on the load transfer concept require that there should be zero or very little plastic deformation of the reinforcement. This requirement does not seem to be satisfied owing to high dislocations within the TiB_2 particles. The theories of dislocation climb based on climb over second-phase particles are inadequate, since they predict strengthening which is three orders of magnitude too small [32, 33]. Finally, the theories of composite strengthening proposed by Arsenault and coworkers [37–45] which are based on an increased dislocation density and reduced subgrain size cannot be applied. The average dislocation density in the 10–20 vol.% composites is less than the average dislocation density in the 0 vol.% matrix material. Therefore an entirely new approach to causes of strengthening will have to be considered.

5. Conclusions

From a consideration of the data, there are several conclusions at which we can arrive.

First, in regard to the NiAl matrix:

(1) there are other particles present within the matrix, possibly constituting as much as 10 vol.%;

(2) the Burgers vector is a {100} type with no defined slip plane;

(3) deformation at low strain rates results in no large change in dislocation densities, while at higher strain rates shear bonds are observed in the 0vol.%TiB_2–NiAl.

Secondly, in regard to the TiB_2–NiAl composites:

(1) there is heterogeneous distribution of dislocations in the TiB_2–NiAl deformed samples;

(2) the TiB_2 is deformed;

(3) at present, a strengthening mechanism is not obvious.

Acknowledgments

This research was supported by the Office of Naval Research under Contract N00014-K-85-0007. The positive interactions with Dr. S. Fishman of the Office of Naval Research are to be greatly acknowledged. The authors wish to acknowledge the assistance of Dr. S. B. Wu in the performance of the high temperature compression tests. The authors wish to acknowledge the continued support of the Argonne National Laboratory HVEM facility, especially that of Dr. E. Ryan.

References

1 J. H. Westbrook, *J. Electrochem. Soc., 103* (1956) 54.
2 E. M. Grala, in J. H. Westbrook (ed.), *Mechanical Properties of Intermetallic Compounds*, Wiley, New York, 1960, pp. 358–404.
3 E. P. Lautenschlager, D. A. Kiewit and J. O. Brittain, *Trans. Metall. Soc. AIME, 233* (1965) 1297.
4 A. G. Rozner and R. J. Wasilewski, *J. Inst. Met., 94* (1966) 169.
5 A. Ball and R. E. Smallman, *Acta Metall., 14* (1966) 1349.
6 R. R. Vandervoort, A. K. Mukherjee and J. E. Dorn, *Trans. Am. Soc. Met., 59* (1966) 930.
7 R. T. Pascoe and C. W. A. Newey, *Metall. Sci. J., 2* (1968) 138.

8 P. R. Strutt, R. A. Dodd and G. M. Rowe, *Creep in Stoichiometric NiAl; Second Int. Conf. on the Strength of Metals and Alloys*, Vol. III, American Society for Metals, Metals Park, OH, 1971, pp. 1057–1061.
9 W. J. Yang and R. A. Dodd, *Metall. Sci. J.*, 7 (1973) 41.
10 L. A. Hocking, P. R. Strutt and R. A. Dodd, *J. Inst. Met.*, *99* (1971) 98.
11 J. Bevk, R. A. Dodd and P. R. Strutt, *Metall. Trans.*, *4* (1973) 159.
12 H. L. Fraser, R. E. Smallman and M. H. Loretto, *Phil. Mag.*, *28* (1973) 651.
13 E. M. Schulson and D. R. Barker, *Scr. Metall.*, *17* (1983) 519.
14 J. D. Whittenberger, *Mater. Sci. Eng.*, 57 (1983) 77.
15 J. D. Whittenberger, *Mater. Sci. Eng.*, *73* (1985) 87–96.
16 W. R. Kanne Jr., P. R. Strutt and F. A. Dodd, *Trans. Metall. Soc. AIME*, *245* (1969) 1259.
17 R. T. Pascoe and C. W. A. Newey, *Metall. Sci. J.*, 5 (1971) 50.
18 G. F. Hancock and B. R. McDonnell, *Phys. Status Solidi A*, *4* (1971) 143.
19 A. E. Berkowitz, F. E. Jaumot Jr. and F. C. Nix, *Phys. Rev.*, *95* (1954) 1185.
20 A. Lutze-Birk and H. Jacobi, *Scr. Metall.*, *9* (1975) 761.
21 S. Shankar and L. L. Siegle, *Metall. Trans. A*, *9* (1978) 1467.
22 A. Lasalmonie, *J. Mater. Sci.*, *17* (1982) 2419.
23 E. P. Lautenschalager, T. C. Tisone and J. O. Brittain, *Phys. Status Solidi*, *20* (1967) 443.
24 O. D. Sherby, R. H. Klundt and A. K. Miller, *Metall. Trans. A*, *8* (1977) 843.
25 J. D. Whittenberger, *Mater. Sci. Eng.*, *77* (1986) 103.
26 J. D. Whittenberger, *J. Mater. Sci.*, *22* (1987) 394.
27 R. R. Jensen and J. K. Tien, *Metall. Trans. A*, *16* (1985) 1049.
28 R. W. Guard and A. M. Turkalo, in J. H. Westbrook (ed.), *Mechanical Properties of Intermetallic Compounds*, Wiley, New York, 1960, p. 141.
29 R. J. Arsenault and S. B. Wu, unpublished investigation, University of Maryland.
30 A. K. Misra, Thermodynamic analysis of compatibility of several reinforcement materials with beta phase NiAl alloys, *NASA Contractor Rep. 4871*, 1988.
31 M. Taya and H. Lilholt, to be published.
32 J. H. Hassenlet and W. Nix, *Acta Metall.*, *25* (1977) 1491.
33 W. Blum and B. Reppich, in B. Wilshire and R. Evans (eds.), *Creep Behavior of Crystalline Solids*, Pineridge Press, Swansea, 1985, p. 85.
34 F. J. Humphreys and P. B. Hirsch, *Proc. Fourth Int. Conf. on Strength of Metals and Alloys*, Vol. 1, Laboratoire de Physique de Solide, E.N.S.-M.I.M.-I.N.P.L., Nancy, 1976, p. 204.
35 I. Kramer, C. R. Feng and R. J. Arsenault, *Metall. Trans. A*, *15* (1984) 1571.
36 W. R. Kanne Jr., P. R. Strutt and R. A. Dodd, *Metall. Trans.*, *245* (1969) 125[illegible]
37 R. J. Arsenault, *Mater. Sci. Eng.*, *64* (1984) 171.
38 R. J. Arsenault and M. Taya, *Acta Metall.*, *35* (1987) 651.
39 M. Vogelsang, R. J. Arsenault and R. M. Fisher, *Metall. Trans. A*, *17* (1986) 379.
40 R. J. Arsenault and S. B. Wu, *Mater. Sci. Eng.*, *96* (1987) 77.
41 R. J. Arsenault and N. Shi, *Mater. Sci. Eng.*, *81* (1986) 175.
42 Y. Flom and R. J. Arsenault, *Mater. Sci. Eng.*, *75* (1985) 151.
43 Y. Flom and R. J. Arsenault, *Mater. Sci. Eng.*, *77* (1986) 191.
44 M. Taya and R. J. Arsenault, *Scr. Metall.*, *21* (1987) 349.
45 R. J. Arsenault, *J. Comp. Tech. Res.*, *10* (1988) 140.

PHILOSOPHICAL MAGAZINE A, 1991, VOL. 63, NO. 1, 121-130

Dislocations in titanium diboride

By L. WANG and R. J. ARSENAULT

Metallurgical Materials Laboratory, University of Maryland, College Park, Maryland 20742, U.S.A.

[*Received 21 November 1989 and accepted 23 January 1990*]

ABSTRACT

In this investigation, it was shown that titanium diboride would plastically deform at a temperature of 1273 K and at a stress level much lower than predicted by previous experimental data. The crystal structure of titanium diboride is a topologically hexagonal structure which allows for a number of possible slip systems. Experimentally, it was observed that three slip directions were present: [0001], $\frac{1}{3}\langle 2\bar{1}\bar{1}0\rangle$ and $\frac{1}{3}\langle 2\bar{1}\bar{1}3\rangle$. The probable slip planes are (0001), $\{10\bar{1}0\}$ and $\{10\bar{1}1\}$.

§ 1. INTRODUCTION

Titanium diboride (TiB_2) is an interesting material. It has a high-temperature strength which is greater than other ceramics such as silicon carbide (SiC) and aluminium oxide (Al_2O_3) (Ramberg and Williams 1987). Also, TiB_2 is a reinforcement candidate in high-temperature composite for it is inert with respect to potential matrix materials. One of the composite systems which has received some attention is TiB_2 in nickel aluminide (NiAl) (Wang and Arsenault 1990). It was found that the addition of 30 vol.% particulate TiB_2 resulted in a threefold increase in the yield stress at 1273 K. The reason why this increase occurs is not evident.

A microstructural investigation was undertaken of these composites to determine the effect of the addition of TiB_2 on the dislocation arrangement and density within the NiAl matrix. It was assumed that the TiB_2 did not deform at 1273 K, for the yield stress at 1273 K which is obtained by a lower limit extrapolation would be 2000 MPa (Ramberg and Williams 1987). The stress concentration in the TiB_2 that could occur owing to load transfer would not be large enough to exceed 2000 MPa. However, it should be pointed out that the TiB_2 used by Ramburg and Williams (1987) contained titanium carbide (TiC) precipitates.

In the investigation of dislocation configuration and density (Wang and Arsenault 1990) in the NiAl matrix of TiB_2–NiAl composites deformed at 1273 K, it was observed that there was a high density of dislocations within TiB_2 particles. Therefore, at least two questions arose.

(1) Did the dislocations within the TiB_2 arise from deformation of the composites?
(2) What types of dislocation are within the TiB_2 particles?

There appears to be a large number of possibilities.

Nakano, Imura and Takenchi (1973) and Nakano, Matsubar and Imura (1974) in an investigation of the high-temperature hardness of TiB_2 concluded that the primary slip system was $\{1010\}\langle\bar{1}2\bar{1}0\rangle$. However, Ramberg and Williams proposed two other systems: $\{10\bar{1}0\}[0001]$ and $(0001)\langle 10\bar{1}0\rangle$.

0141-8610/91 $3.00

Fig. 1

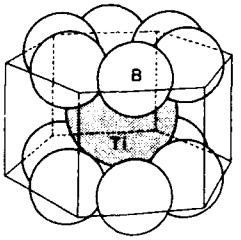

Ball model of TiB_2. Boron atoms form a net connection only. Titanium atoms sit in the open centre of the net (Westbrook 1967).

Table 1. Yield stress of 10 vol.% TiB_2–NiAl deformed at 1273 K.

Strain rate (s^{-1})	Yield stress (MPa)	
	Annealed at 1673 K	Not annealed
$1{\cdot}1 \times 10^{-4}$	80·9	70·6
$2{\cdot}2 \times 10^{-4}$	84·6	81·6
$2{\cdot}2 \times 10^{-3}$	136·1	111·3

The reason that so many possibilities exist is related to the crystal structure of TiB_2 which is schematically shown in fig. 1. The crystal structure could be defined as a topologically hexagonal structure (Parthe 1967), in which the boron atoms form a net connection only. For the case of packing of touching spheres (Laves 1956), the ideal $c/a = 1{\cdot}07$, and $c/a = 1{\cdot}063$ for TiB_2. From an examination of fig. 1, it is evident that there is no well defined close-packed plane, but the closest-packed plane is (0001) and the shortest repeat distance in this plane is $\frac{1}{3}[11\bar{2}0]$.

The purpose of the present investigation was to determine whether an increase in the dislocation density did indeed occur upon deformation of the TiB_2 NiAl composite, and to characterize the various types of dislocation Burgers vector that were assumed to be present in the TiB_2 particles within the deformed TiB_2–NiAl composite.

§2. Materials and experimental procedures

The TiB_2 NiAl composite used in this investigation was purchased from Martin Marietta Corporation. The composite contained 10 or 20 vol.% TiB_2 and the TiB_2 particles were of various shapes and size but on average the largest dimension was 3 μm.

Prior to testing, the compression samples, with a length-to-diameter ratio of two, were annealed at 1273 and 1673 K for periods of time of 2–12 h. Variation in annealing times had no effect on the strength of the composite. Surprisingly, annealing at 1673 K resulted in a slight increase in strength. The samples were tested at 1273 K at various strain rates and a summary of the results is given in table 1 (details of the testing have been given elsewhere (Wang and Arsenault 1990)). The transmission electron microscopy (TEM) foils were obtained from the deformed composite samples and examined at both 100 kV and 1 MeV. Further details of the foil preparation have been given elsewhere (Wang and Arsenault 1990). Since it is assumed that there will be a large number of possible Burgers vectors, it is necessary to use a number of operating

diffraction vectors. However, if the relative intensity of the operating diffraction vector is low, then the dislocations would be in very low contrast. Therefore all micrographs in this paper were taken under operating conditions where the relative intensity is large enough to show the difference between the residue contrast of invisible dislocations and the image of visible dislocations.

§ 3. Results and discussion

The initial portion of the investigation was to determine whether the dislocation density within the TiB_2 increased as a result of a deformation of the composite. In annealed samples, there is a low dislocation density in both the matrix and the TiB_2, as shown in fig. 2 (*a*), except in the case where some of the particles are in contact with each other. A comparison of TEM micrographs of annealed samples and deformed samples clearly shows that the density of dislocations within the TiB_2 is significantly higher in the deformed composite sample, as shown in figs. 2 and 3.

It was found that the planar sides of a TiB_2 particle were almost always parallel to the (0001) plane. The dislocations labelled A and B do not lie on the plane of the foil but lie on a plane whose trace is parallel to the bottom edge of the particle. In other words, dislocations A and B lie on the (0001) plane which is perpendicular to the plane of the foil. Under conditions of 0001 and $\bar{2}02\bar{1}$ operating diffractions, dislocations labelled A in fig. 3 (*a*) are almost completely invisible. Therefore, the dislocations labelled A have Burgers vectors of $\frac{1}{3}[1\bar{2}10]$. The dislocation labelled B in figs. 3 (*a*) and (*c*) which is only invisible under the operation diffraction 0001 has a Burgers vector of $\frac{1}{3}[\bar{2}110]$ or $\frac{1}{3}[11\bar{2}0]$.

If the electron beam is exactly parallel to the basal plane, then the projection of dislocations on the basal plane should be straight lines. However, there are exceptions if climb occurs as indicated by the arrow in fig. 3 (*a*). Also, it has been found that stacking faults exist on the basal plane in TiB_2 (Mersol, Lynch and Vahldiek 1968). Again, if the electron beam is parallel to the basal plane as in fig. 4 (*a*), the dislocation on the basal plane should project as a straight line labelled A. If the sample is tilted as shown in fig. 4 (*b*), then stacking-fault ribbons are evident. The presence of stacking faults is not universal; only a few TiB_2 particles contained stacking faults.

It is suspected that slip on the prism plane also occurs and that prismatic punching into the TiB_2 particles from the interface takes place, that is the dislocations labelled C in figs. 5 (*a*) and (*b*). If different operation diffractions are used ($\bar{1}010$ and $\bar{2}110$), then prismatically punched dislocations become invisible (figs. 5 (*c*) and (*d*)) in areas that the Burgers vector of prismatically punched dislocations is [0001].

There are dislocations with other Burgers vectors within this particle. The dislocations labelled E in figs. 5 (*a*) and (*c*) are out of contrast under the diffraction vector 0001 (fig. 4 (*d*)). The dislocations which have Burgers vectors of $\frac{1}{3}\langle\bar{2}110\rangle$ obviously do not lie on the basal plane. It is therefore possible that slip directions of the $\frac{1}{3}\langle\bar{2}110\rangle$-type can occur on other slip planes.

Besides dislocations with Burgers vectors of $\frac{1}{3}\langle\bar{2}110\rangle$ and [0001], there are still other dislocations with different Burgers vectors, for example the dislocations labelled D in fig. 5. It was difficult experimentally to find two independent extinction conditions for these dislocations because of the tilting limit of the sample stage. Every operating diffraction condition was employed which had an intensity high enough to show the difference between the residual contrast of invisible dislocations and the contrast of visible dislocations in the $(1\bar{2}10)^*$, $(0\bar{1}10)^*$, $(0\bar{1}11)^*$ and $(1\bar{2}13)^*$ reciprocal planes. However, the Burgers vector of dislocations labelled D could not be determined.

Fig. 2

(*a*)

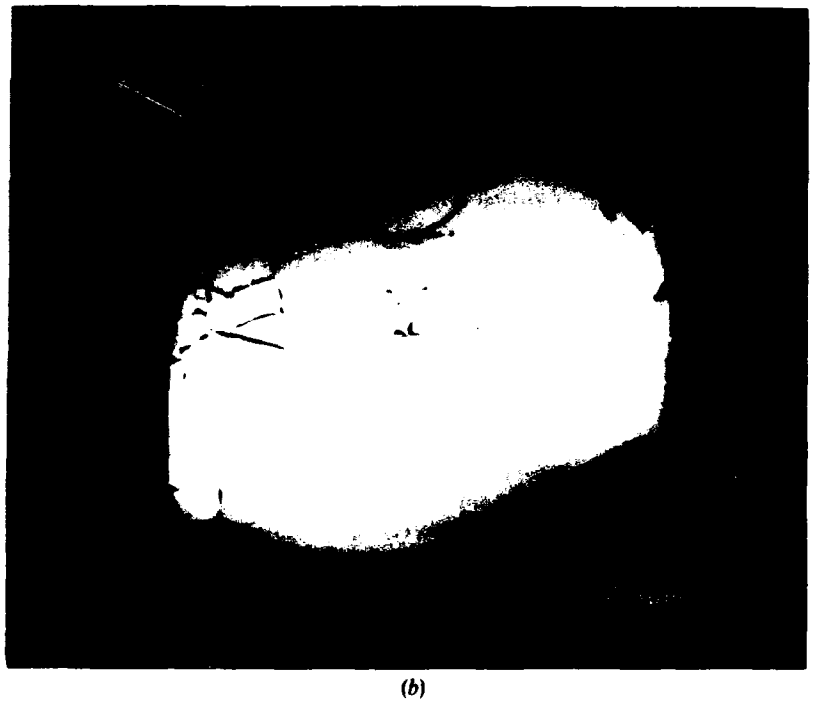

(*b*)

TEM micrographs of (*a*) annealed 20 vol.% TiB_2–NiAl composite (low dislocation density both in matrix and TiB_2) and (*b*) a TiB_2 particle in annealed 20 vol.% TiB_2–NiAl composite.

Fig. 3

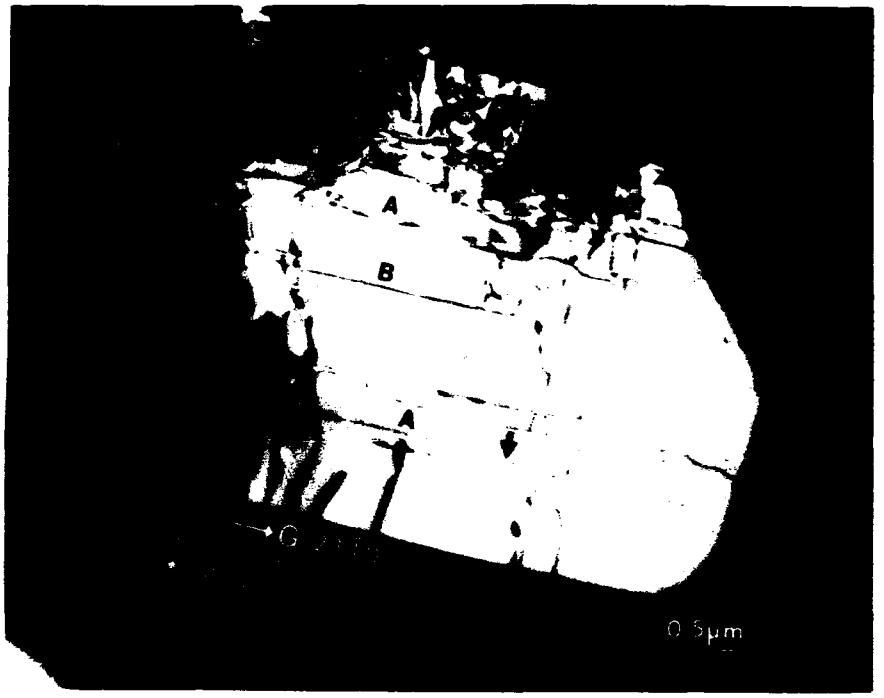

(*a*)

(*b*)

(*c*)

TEM micrographs of a TiB_2 particle in deformed 20 vol.% TiB_2–NiAl composite with different operating diffractions: (*a*) dislocation with Burgers vector of $\frac{1}{3}\langle\bar{2}110\rangle$ type on the basal plane are visible; (*b*) all $\frac{1}{3}\langle\bar{2}110\rangle$-type dislocations are invisible; (*c*) only dislocations with Burgers vector of $\frac{1}{3}[1\bar{2}10]$ are invisible.

It is possible to obtain the Burgers vector of dislocations labelled D by considering the dislocation reaction which occurs at the arrow in figs. 5(*b*)–(*d*). Dislocations labelled A which have a Burgers vector of $\frac{1}{3}[\bar{2}110]$ reacted with the dislocation labelled D which results in the short segment of dislocation indicated by the arrow in these pictures. This short segment of dislocations has a Burgers vector of [0001], for it followed the same extinction conditions as the dislocation labelled C which has a Burgers vector of [0001]. Therefore the reaction can be written as

$$\mathbf{b}_A + \mathbf{b}_D = \mathbf{b}_C.$$

The subscripts denote the dislocations labelled in fig. 5. Since $\mathbf{b}_A$ is $\frac{1}{3}[\bar{2}110]$ and $\mathbf{b}_C$ is [0001], then the dislocations labelled D must have a Burgers vector of the type $\frac{1}{3}\langle\bar{2}113\rangle$. The reason why it is so difficult to find two independent extinction conditions to determine the Burgers vector of dislocation labelled D directly is that only the $(\bar{1}0\bar{1}1)$ diffraction condition satisfies the extinction condition. This one extinction condition is not enough to determine the Burgers vector of these dislocations. It was impossible to obtain extinction conditions owing to the limitations of the sample tilting stage.

The possible combinations of slip directions and slip planes are listed in table 2. The three directions were determined in this investigation, and the planes listed are the three of highest atomic packing.

Fig. 4

(*a*)

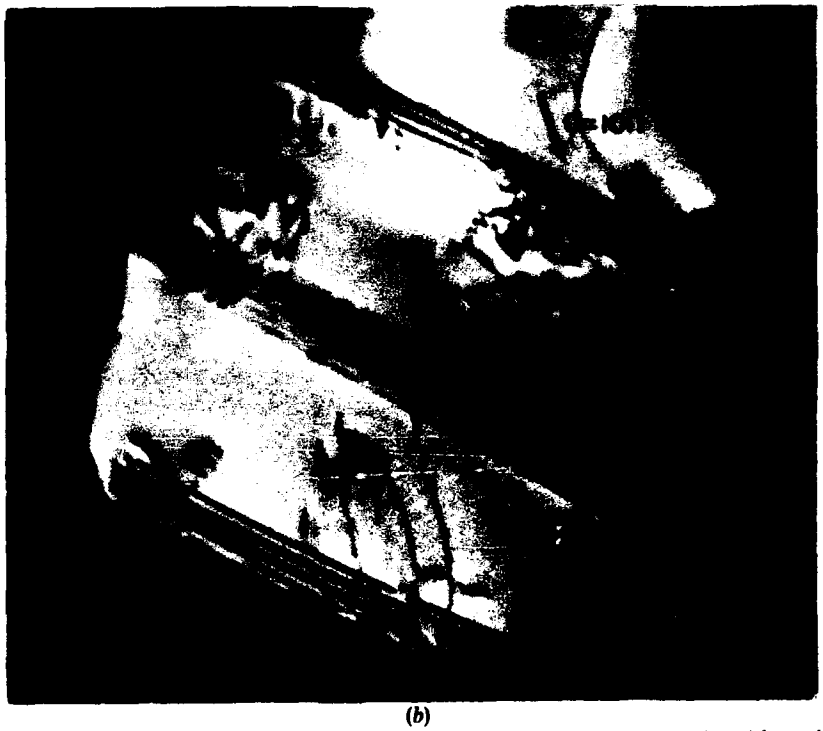

(*b*)

TEM micrographs of a TiB_2 particle in deformed 20 vol.% TiB_2–NiAl composite with stacking faults on the basal plane: (*a*) basal plane is parallel to the electron beam; (*b*) basal plane is not parallel to the electron beam.

Fig. 5

(*a*)

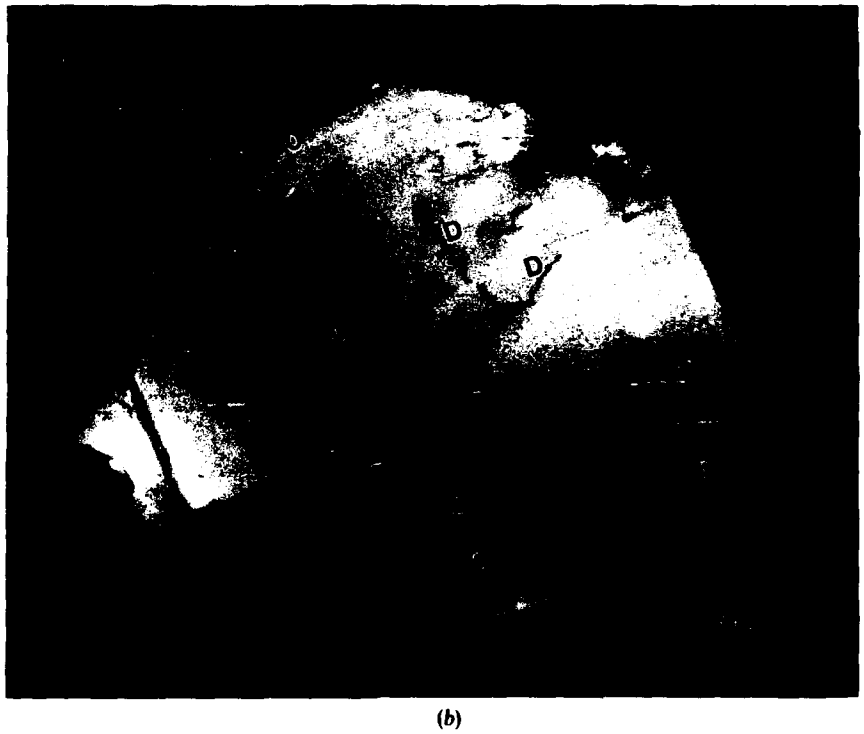

(*b*)

(*c*)

(*d*)

TEM micrographs of a TiB_2 particle in deformed 20 vol.% TiB_2–NiAl composite: (*a*) many-beam condition, all the dislocations are visible; (*b*) all the $\frac{1}{3}\langle\bar{2}110\rangle$-type dislocations are invisible; (*c*), (*d*) prismatically punched dislocation out of contrast.

Table 2. Slip systems in titanium diboride.

Slip direct s	Presence of slip system in the following slip planes		
	(0001)	$\{10\bar{1}0\}$	$\{10\bar{1}1\}$
[0001]		Yes	
$\frac{1}{3}\langle\bar{2}110\rangle$	Yes	Yes	Yes
$\frac{1}{3}\langle\bar{2}113\rangle$			Yes

§4. Conclusions

From the data obtained in this investigation, it is possible to arrive at the following conclusions.

(1) The TiB_2 particles within a deformed TiB_2–NiAl composite can be plastically deformed as shown by the increased dislocation density within the TiB_2 particles.
(2) Three slip directions were observed within the TiB_2 particles; they are $\frac{1}{3}\langle\bar{2}110\rangle$, [0001] and $\frac{1}{3}\langle\bar{2}113\rangle$.
(3) Dislocations with Burgers vectors of the type $\frac{1}{3}\langle\bar{2}110\rangle$ on the basal plane could split into two partials with a stacking fault between the partials.
(4) Most of the dislocations in TiB_2 had Burgers vectors of [0001] or $\frac{1}{3}\langle\bar{2}113\rangle$.

Acknowledgments

The authors wish to acknowledge the continued encouragement of Dr S. Fishman of the Office of Naval Research and the assistance of Dr E. Ryan of the Argonne National Laboratory High Voltage Electron Microscopy Facility. The authors also wish to acknowledge the clarification and correction suggested by the reviewer. This research was supported by the Office of Naval Research under Contract N00014-85-K-0007.

References

Laves, F., 1956, *Theory of Alloy Phases* (Metals Park, Ohio: American Society for Metals).
Mersol, S. A., Lynch, C. T., and Vahldiek, F. W., 1968, *Anisotropy in Single-Crystal Refractory Compounds* (New York: Plenum), p. 41.
Nakano, K., Imura, T., and Takenchi, S., 1973, *Jap. J. appl. Phys.*, **12**, 186.
Nakano, K., Matsubar, H., and Imura, T., 1974, *Jap. J. appl. Phys.*, **13**, 1005.
Parthe, E., 1967, *Intermetallic Compounds* (New York: Wiley), p. 212.
Ramberg, J. R., and Williams, W. S., 1987, *J. Mater. Sci.*, **22**, 1815.
Wang, L., and Arsenault, R. J., 1990, *Mater. Sci. Engng* (to be published).
Westbrook, J. H., 1967, *Intermetallic Compounds* (New York: Wiley), p. 138.

Materials Science and Engineering, A131 (1991) 55–68

Localized Deformation of SiC–Al Composites

R. J. ARSENAULT, N. SHI, C. R. FENG and L. WANG

Metallurgical Materials Laboratory, Dept. of Mat. and Nuclear Eng., University of Maryland, College Park, MD 20742-2115 (U.S.A.)

(Received December 27, 1989; in revised form May 30, 1990)

Abstract

Tensile tests of SiC–6061 Al composites containing various volume fractions of whiskers or particles (20, 5 and 0 vol.%) showed that for samples containing a high volume fraction (20 vol.%) the fracture process was very localized, i.e. a very narrow neck. As the volume fraction of whiskers or particles decreased, the deformed region spread out. One might expect that the microstructure should correspond to the macroscale changes. In the highly deformed region the dislocation density is expected to be higher, in the less deformed regions the dislocation density should be lower, and if the deformation is very localized, then the high dislocation density should also be limited to a very narrow region.

Overall, there is good agreement between the microstructure (dislocation density) change and the macroscale deformation of SiC–Al composite tensile samples. The mechanism proposed to account for this change in deformation behavior as a function of volume fraction of SiC in aluminum is related to the expansion of the plastic zone (due to differences in thermal coefficients of expansion between SiC and aluminum) when the external stress is applied. Also, the localized deformation is related to localized clusters of SiC particles. There is a cooperative effect which leads to a region of very localized plastic deformation.

1. Introduction

There are many unusual deformation characteristics associated with SiC–Al discontinuous metal matrix composites. One of them is that the ductility and fracture toughness of SiC–Al composites are very low [1]. Generally, examinations of the fracture surface do not reveal the presence of SiC particulates or whiskers in the quantities corresponding to their volume fraction [1]. The fracture process is very localized, very little "necking" is observed (in high volume fraction composites), but the fracture surface has both brittle and ductile characteristics. There is no indication of fracture of SiC when the size of SiC is less than 10 μm. The fracture may initiate at large intermetallic inclusions, clusters of SiC particulates or whiskers and voids associated with the SiC particulates or whiskers [1].

The results [2] of tensile tests of SiC–6061 Al composites with various volume fractions of whiskers or particulates (20, 5 and 0 vol.%) indicated that for high volume fraction samples (20 vol.%) the fracture process was very localized. As the volume fraction of whiskers or particulates decreased, the deformed region "spreads out". Figure 1 demonstrates how "necking" changes

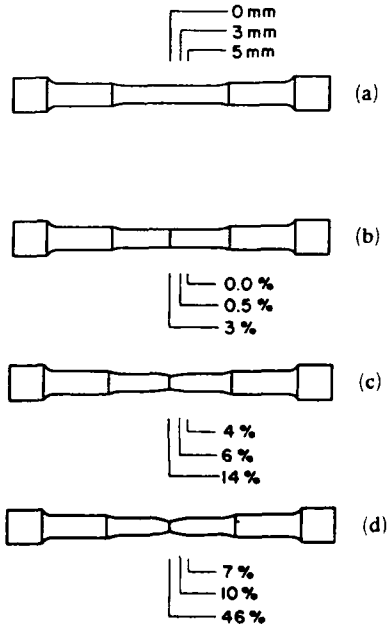

Fig. 1. Reduction in area at various distances from fracture surface for SiC–Al composite tensile samples: (a) undeformed; (b) 20 vol.% SiC; (c) 5 vol.% SiC; (d) 0 vol.% SiC.

0921-5093/91/$3.50

with a decrease in volume fraction. In the case of the 20 vol.% composite the reduction in area at the fracture surface was only 3%, and 5 mm away from the fracture surface the reduction in area was *zero*. However, in the case of the 5 vol.% composite, at the fracture surface the reduction in area was 14%, and 5 mm away from the fracture surface the reduction in area was 4%.

One might expect in a highly deformed region that the dislocation density is very high and in the less deformed region the dislocation density should be lower. In other words, the high dislocation density should be limited to a very narrow region. It is also of interest to know that previous work [1] has indicated that along the fracture path the local density of SiC particles is higher than the average volume fraction of the SiC. In other words, the fracture path is attracted to the particle clusters. However, it is still unclear whether such a "particle friendliness" is only restricted to the fracture process or if it also governs the onset of plastic deformation.

If there are high dislocation densities in regions containing a larger-than-average volume fraction of SiC, this indicates that is where deformation is taking place. This is intuitively difficult to understand. It has been clearly shown that if the volume fraction of SiC is increased in an aluminum matrix, the strength increases. Therefore the question arises: why should deformation begin and be restricted to regions of higher-than-average volume fraction of SiC? The logical assumption would suggest that deformation should begin in regions of less-than-average volume fraction of SiC.

There have been numerous investigations and several theories of the ductile fracture of two-phase alloys where the second phase is a discrete, non-deforming precipitate or particle [3–19]. All the theories are based on the assumption that a void nucleates at the interface of a non-deforming particle and then grows, leading to an ultimate fracture. An examination of transverse sections by optical microscopy and scanning electron microscopy (SEM) methods indicated that there are very few voids near the fracture surface. It is possible that the voids nucleated are very small and can only be observed by transmission electron microscopy (TEM) techniques.

To answer the questions raised above, an investigation was proposed to determine the dislocation density along the tensile axis of the gauge section by using transmission electron microscopy to relate macro- and microstructural changes to the plastic deformation and to determine if a correlation exists between slip line generation and density and the localized volume fraction of SiC in the SiC–Al composite. Also, the purpose of this investigation was to determine if there was a higher density of voids near the fracture surface in SiC–Al composites.

To investigate the underlying mechanism for such a phenomenon, a set of two-dimensional finite element method (FEM) meshes were generated to simulate the effect of inhomogeneous distribution of the SiC reinforcement whiskers, *i.e.* the effect of clustering. Furthermore, it is also of importance to know the plastic deformation process around each SiC whisker. Therefore a three-dimensional FEM mesh was generated to monitor the behavior of plastic zones around whiskers.

2. Experimental procedures

2.1. Materials

SiC-whisker- or particulate-reinforced 6061 Al alloy composites which were obtained commercially were used for this investigation.

The composites with 20, 5 and 0 vol.% SiC whiskers (SiC_w–Al) were purchased from ARCO SILAG (presently, Advanced Composite Materials) in the form of extruded rods 15.5 mm in diameter. The composites with 20 and 5 vol.% SiC particulates (SiC_p–Al) were purchased from DWA Composite Specialties in the form of plates 15.9 mm thick. All materials were fabricated by the powder metallurgy method. The whiskers [20] were small in diameter, ranging from 0.1 to 1 μm, and the average aspect ratio was 2. The particulates were platelet shaped, 5–7 μm long and had an aspect ratio of 2–3.

Sample blanks were cut from the rods and plates, then machined into tensile samples. The doubly reduced samples were required to ensure that the fracture occurred in the gauge section and not in the transition region [20]. The dimensions of the samples are given in Fig. 2. Those that were to be heat treated were given a modified T6 heat treatment, which means a solutionizing step of 3 h (modified) as opposed to the standard 1 h. The modified heat treatment was used in case a divorced eutectic formed during the processing. The others were annealed for 12 h at a solutionizing temperature of 810 K and furnace cooled. The method of producing the "melted"

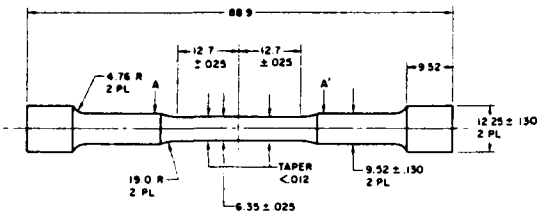

Fig. 2. Dimensions of a round tensile sample (in millimeters).

250 μm SiC_p–1100 Al alloy composites has been described elsewhere [21].

2.2. Tensile testing

All samples were tested in an Instron testing machine at room temperature. Most of the samples were tested to failure; however, some were tested to a strain where a measurable "neck" occurred in the sample.

2.3. TEM thin foil preparation and examination

The method of TEM foil preparation has been given elsewhere [22]. In a recent publication by Arsenault *et al.* [23] it has been clearly shown that in order to obtain representative dislocation densities it is necessary to examine the foils at a high operating voltage. All the foils were observed in the AEI-EM7 high voltage electron microscope (HVEM) operated at 1 MeV at the Argonne National Laboratory.

The TEM foil thickness was determined by counting the extinction fringes or from stereo-pairs. All the micrographs were taken under two beam conditions with the diffraction vectors being $\boldsymbol{g}=[111]$ or [200], but in most cases the diffraction vector was $\boldsymbol{g}=\{111\}$. If a higher order of diffraction vectors such as $\boldsymbol{g}=\{220\}$ is used, the contrast is reduced, which results in difficulties in determining the dislocation density. Since the Burgers' vector of aluminum is of $\frac{1}{2}\{110\}$ type and there are six specific Burgers' vectors, any given $\{111\}$ reflection will result in three of the six being visible. Therefore in calculating the dislocation density the measured density was multiplied by a factor of 2.

For each TEM foil examined in the HVEM a minimum of 10 micrographs were taken and there could be as many as 100. The procedure was to examine the micrographs and make a visual selection, removing the micrographs which had extremely high or low dislocation densities. This selection procedure greatly reduced the time necessary to determine the dislocation density of a given foil.

2.4. Dislocation density calculation

The dislocation densities from the selected micrographs were determined by the method proposed by Keh [24]. In this method a grid of two sets of lines, normal to each other but with different spacing, is placed over the TEM micrograph and then the intersection of dislocations is given by

$$\rho=\frac{N_1/L_1+N_2/L_2}{t} \tag{1}$$

where L_1 and L_2 are the lengths of the grid lines normal to each other, N_1 and N_2 are the intersections along the lines and t is the thickness of the foil in the area where the micrograph was taken.

The average density was determined for a given foil by simply taking the numerical average of the examined foils. This same procedure was followed for all foils of a given condition, *e.g.* the same distance from the fracture surface. The error bar associated with data points of dislocation *vs.* distance from the fracture surface simply covers the range of the averages.

The upper limit [25] of dislocation density calculated by using eqn. (1) is about 10^{15}–10^{16} m^{-2}. In some micrographs the dislocations were so dense that it was impossible to see the individual dislocation. The dislocation density was estimated by using the width of the micrograph divided by the width of the dislocation image. Clearly, the value of dislocation density was underestimated.

In the case of very high dislocation densities it may be argued that the weak beam technique should be employed. However, the weak beam technique fails because it is extremely sensitive to the diffraction condition, *i.e.* the $\boldsymbol{s}$ vector. For a sample with a very high dislocation density the $\boldsymbol{s}$ vector does change from point to point within the sample. This is especially true in the thicker foils which are used in the HVEM.

2.5. Slip line analysis

While composite samples with a small reinforcement size are more suitable for TEM analyses, composites with larger reinforcement are preferred for optical observation of slip lines. As a result, melted 250 μm particulate-reinforced

composite material was chosen for the analysis. From this melted particulate-reinforced composite, rectangular samples 8 mm wide by 50 mm long and 1.5 mm thick were electrical discharged machined and polished. The samples were glued to an E. Fullam tensile substage model 18202 JEOL JSM-35. The substage was mounted on a specially constructed holder to fit on to a Zeiss ICM-405. The entire effective gauge was photographed. Then the sample was deformed by a small amount and the area which contained slip lines was re-photographed, and again the sample was deformed and re-photographed where slip lines occurred. This process was repeated until the sample fractured.

2.6. FEM procedures

2.6.1. Two-dimensional FEM procedures

In the present study the composites are represented by a periodic array of transversely aligned whiskers as shown in Fig. 3, *i.e.* an infinite two-dimensional array of SiC whiskers embedded in the aluminum matrix in the plane strain condition. In order to consider the effect of clustering, the array is transformed in such a manner that an array of periodic geometric cluster centers was selected and the neighboring whiskers (in this case, four whiskers (Fig. 4)) were attracted toward their cluster centers so that a periodic array of clusters were formed as shown in Fig. 5. The degree of clustering was defined by the values of S_v/V and S_h/H in Fig. 5.

In applying the above geometric transformation scheme, a commercially available ADINA FEM code was employed. To represent the reality, the material is assumed to be stress free at the annealing temperature, *i.e.* 773 K, and is subsequently cooled to room temperature. Therefore the effect of thermal residual stresses is implicitly considered. After thermal treatment the composites, clustered and unclustered, were uniaxially loaded in the whisker directions. Owing to the periodic arrangement, the condition of symmetry can be so utilized that a "unit cell" was selected as a basic building block such that only a quadrant of whisker (cluster) is contained, as shown in Figs. 6(a) and 6(b), and multiconstraint boundary conditions were employed to represent the symmetry conditions at the boundary.

2.6.2. Three-dimensional FEM procedure

In this case the reinforcement particles are hexagonally distributed through three-dimensional space. Because of the symmetry, the response of the composite can be fully represented simply by considering a building block

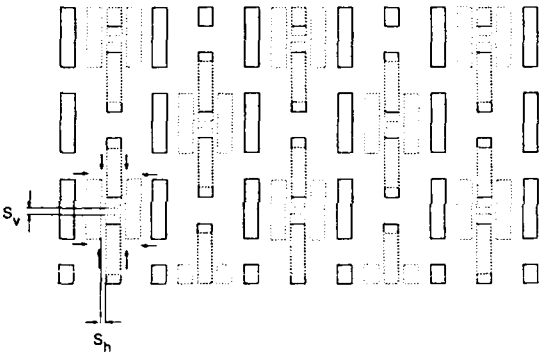

Fig. 4. This figure shows how SiC whiskers move to their geometric cluster center to form a periodic array of clusters. Whiskers with dotted boundaries represent the final locations of the whiskers after the movement indicated by the arrows in the figure, and S_v and S_h show the degree by vertical and horizontal clustering.

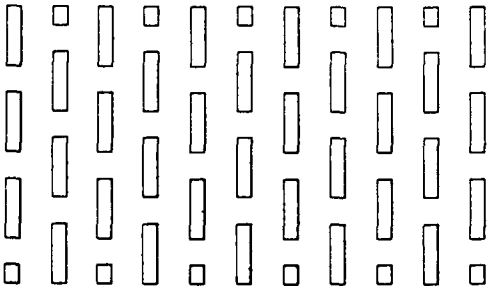

Fig. 3. Periodic hexagonal arrangement of the SiC reinforcement of the whisker. The shaded areas are SiC whiskers.

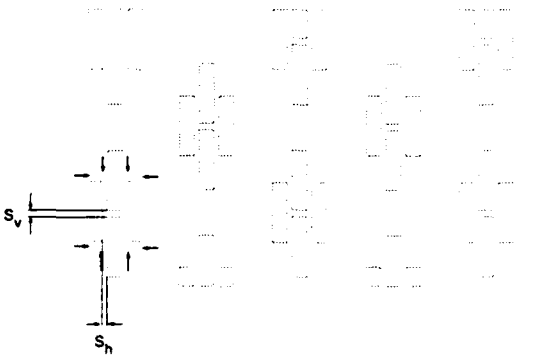

Fig. 5. Configuration of clustered composites.

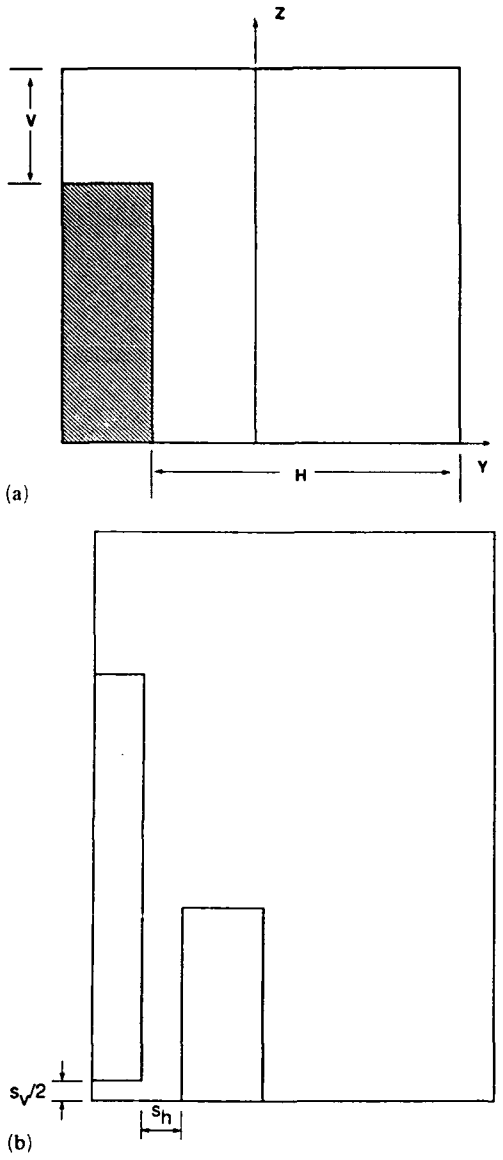

Fig. 6. (a) Unit cell for the uniform distribution of whiskers employed by the FEM analysis, where "h" and "v" stand for the horizontal and vertical half-spacing. (b) Unit cell for the clustered whisker configuration employed by the FEM analysis, where S_v and S_h are defined in the same way as in Fig. 4.

which only contains one-eighth of the reinforcement particle, as shown in Fig. 7, and, in consideration of symmetry, multipoint constraint equations were employed in the boundary conditions. As in the case of two-dimensional analysis, the composites were assumed stress free at 773 K, which is the annealing temperature for

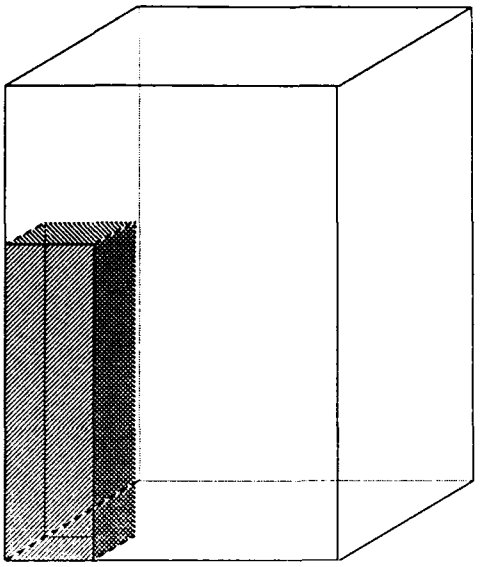

Fig. 7. Unit cell employed for the three-dimensional analysis.

SiC–Al composites, and the sample was subsequently cooled to room temperature. Owing to a large difference in thermal expansion coefficient between SiC and aluminum, severe thermal residual stress would be generated around particles. As a result, it is apparent that a plastic zone will form around each particle. Upon further uniaxial loading, such a plastic zone will certainly respond to the external load. Depending on how such a response would be, it will be helpful to understand the deformation mechanism of the composites. Therefore it is our intention to monitor the geometric change of the plastic zone as a result of external load. This can be done simply by imaginarily slicing the sample longitudinally along the loading direction and monitoring the two-dimensional change of the plastic zone in each plane.

3. Experimental results

The discussion of the experimental results will be divided into four parts: (a) dislocation density *vs.* distance, (b) slip line analysis, (c) FEM results and (d) voids.

3.1. Dislocation density vs. distance

3.1.1. 20 vol.% SiC–Al composite

The plot of dislocation densities (ρ) *vs.* distance from the fracture surface (x) is shown in

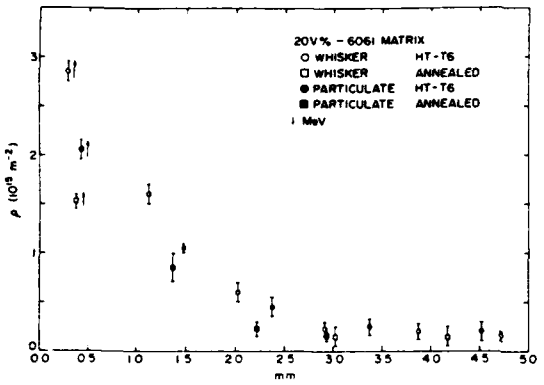

Fig. 8. Dislocation density *vs.* distance from fracture surface for 20 vol.% SiC–Al composite.

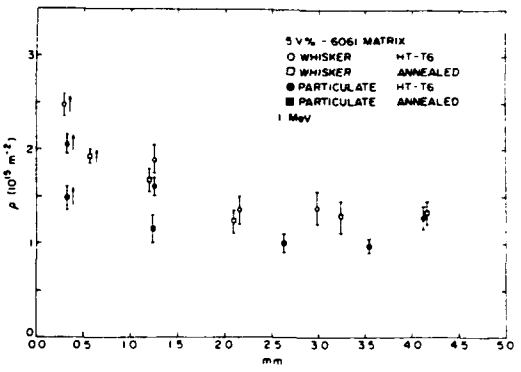

Fig. 9. Dislocation density *vs.* distance from fracture surface for 5 vol.% SiC–Al composite.

Fig. 8. The value of ρ is higher near the fracture surface region and decreases as x increases. When the distance is 3 mm or more, ρ is constant and the value of ρ is approximately equal to the value of ρ for an undeformed sample. This value is about one order of magnitude lower than that in the 0.3–0.5 mm region, *i.e.* near the fracture surface region. In general, the values of ρ are higher in the whisker-reinforced heat-treated samples.

The difference between the dislocation densities of each micrograph in the same foil increases as x increases, which means the dislocation densities are more uniformly distributed near the fracture surface region.

In some foils the difference in the dislocation densities is quite large (it may exceed two orders of magnitude). To avoid confusion, the reported data are the average values of micrographs taken from each location rather than those of a single micrograph.

Several attempts were made to deform 20 vol.% SiC–Al composites until a "neck" occurred, then stopping the test prior to fracturing the sample, and then cutting TEM foils from the sample in the "neck" region. All attempts were failures; either the sample fractured before the test was stopped or upon examination of the TEM foils. There was no difference in density between the perceived "neck" region and the region away from the "neck".

3.1.2. 5 vol.% SiC–Al composite

The plot of dislocation densities (ρ) *vs.* distance from the fracture surface (x) is shown in Fig. 9. Similar to the 20 vol.% composite (Fig. 8), at 0.3–0.5 mm, *i.e.* near the fracture surface region, ρ is higher and approximately equals that of the 20 vol.% samples in the same region; then ρ decreases as x increases. However, at 3 mm and beyond, ρ remains constant and the values of ρ are 3–5 times higher than that of undeformed samples, a result which is different from the 20 vol.% samples. Also, in agreement with the 20 vol.% samples, ρ is higher in the whisker-reinforced heat-treated samples.

As in the case of the 20 vol.% SiC–Al composite, several samples were tested until a "neck" had formed. Then TEM foils were cut from the "neck" region and the ends of the samples. Figure 10(a) is a TEM micrograph of the end region of the sample and Fig. 10(b) is a TEM micrograph showing the high dislocation density in the "neck" region. The variation of the dislocation density from the "neck" region to the ends of the sample is shown in Fig. 11.

3.1.3. 0 vol.% SiC–Al composite

The plot of dislocation densities (ρ) *vs.* distance from the fracture surface (x) is shown in Fig. 12. Near the fracture surface region (0.3–0.5 mm), ρ is higher, but the value of ρ is about one-third of that for the 20 vol.% samples in the same region and, unlike the 20 and 5 vol.% samples, as x increases, ρ decreases at a much slower rate. The values of ρ in this plot are about two orders of magnitude higher than for an undeformed sample. Similar to the 20 and 5 vol.% samples, ρ is higher in the heat-treated samples.

In summary, from the aforementioned experimental observations, a fact can be clearly stated that, irrespective of the reinforcement morphol-

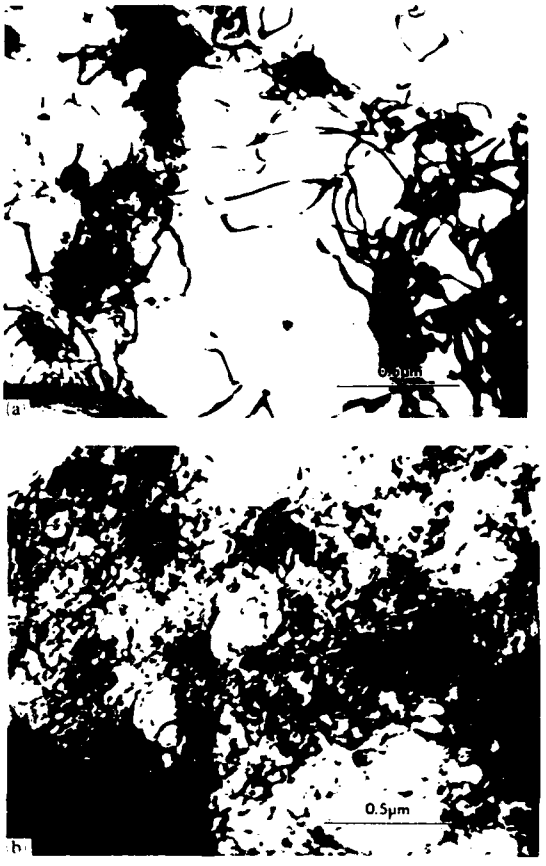

Fig. 10. (a) TEM micrograph of foil taken from the end section of 5 vol.% whisker SiC–Al tensile sample. (b) TEM micrograph of foil taken from the neck section of 5 vol.% whisker SiC–Al tensile sample.

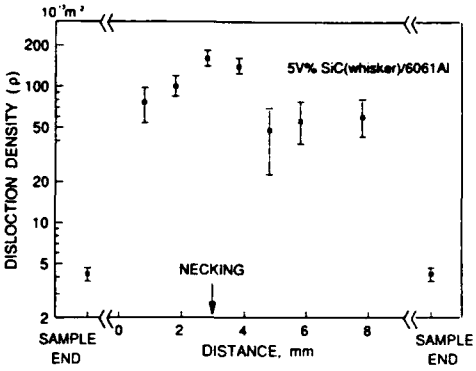

Fig. 11. Plot of dislocation density in the neck region and the end sections of a tensile sample which has been deformed to produce a neck.

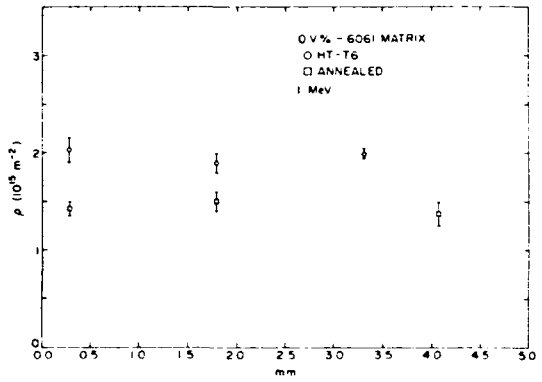

Fig. 12. Dislocation density *vs.* distance from fracture surface for 0 vol.% SiC–Al composite.

ogy, a high dislocation density is restricted to the vicinity of the fracture surface, which represents the highest plastic deformaton site, *i.e.* plastic deformation is very localized.

3.2. Slip line analysis

The initial slip lines began in a region which contained a higher-than-average density of SiC particles *i.e.* a cluster). The very first slip lines in this region occur at the corners of SiC particles, as shown in Fig. 13. Slip lines were observed at the corners of other SiC particles through the gauge length of the sample. By successive incremental loadings, the gauge section of the sample was examined to determine the local density of slip lines. The region with the initial higher-than-average density of SiC particles contains almost all the subsequent increase in slip line density. Figures 14–16 are micrographs taken at successive loadings. In other areas of the sample there are no or very few slip lines.

3.3. FEM

3.3.1. Two-dimensional FEM

The global stress–strain curves of the composites produced by the calculation are shown in Fig. 17. It is clear that the more the whiskers are clustered together, *i.e.* the smaller S_v and S_h in Fig. 6(b), the lower is the yield stress. This is consistent with the experimental data described in the previous subsection, *i.e.* plastic deformation is initiated within the region where there is a higher localized particle concentration (cluster) and this clustering results in a reduction of composite flow stress. This leads to an intuitively obvious conclusion: the more uniform the

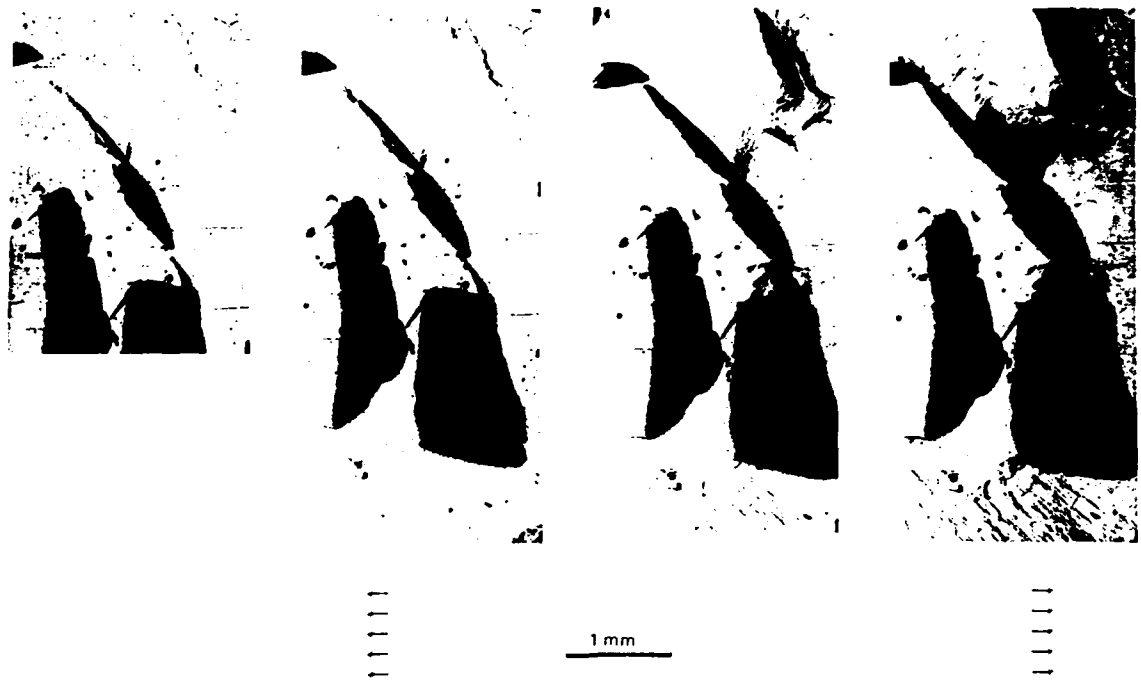

Fig. 13. Sequence of slip line formation as a result of incremental loading along the direction shown by the arrows. As the load increases (from left to right), slip lines first form around the corners of the SiC particles; then, as the load further increases, slip lines formed around each particle will propagate and interconnect and finally form a set of densely packed slip bands.

arrangement of discontinuous reinforcement, the stronger is the composite.

It should be pointed out that while localization of plastic deformation is evident throughout the experimental observations, as we described previously, FEM modeling on a parallelpiped array is best suited for a whisker composite. The results only give a qualitative approximation for the particulate composite.

3.3.2. Three-dimensional FEM

It was found that the plastic zone extended about one particle diameter from the edge of the particle, which is in agreement with the experimental results [26], and the nature of the arrangement of the residual stress along the longitudinal direction is such that at the whisker end the matrix is under compression while the rest of the matrix is under tension. Also, it was found that the plastic zone expanded transversely upon loading the sample in tension, which is in agreement with the slip line analysis, whereas longitudinally it contracts near the whisker ends owing to the compressive nature of the plastic zone in that part of the matrix. However, this process generally means the generation of dislocations of opposite sign; annihilation of dislocations does not make a significant contribution to the process.

3.4. Voids

The TEM micrographs were examined to determine the density of voids at the interface between the matrix and the SiC whiskers or particles. Voids were found; however, the density of voids near the fracture surface was greater than the density of voids in the non-deformed regions of the samples.

4. Discussion

The discussion of the experimental results will be related almost exclusively to explaining how and why the deformation is so localized in the SiC–Al composites. There will be a brief discussion of the lack of voids.

The evidence obtained from the dislocation density and slip line investigations is overwhelming: deformation in the higher volume fraction composites is very localized. From an analysis of the configuration of SiC particles in the samples

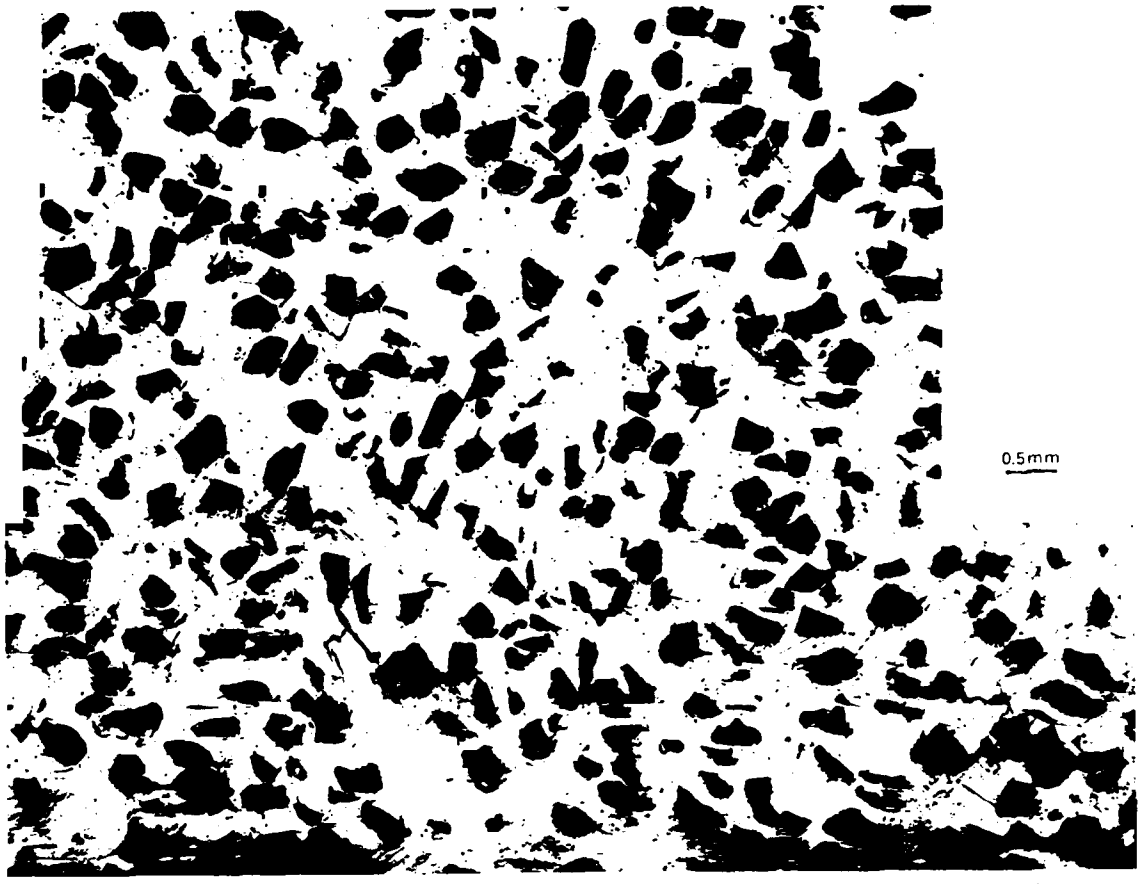

Fig. 14. The sample is slightly deformed. It can be seen that slip lines begin to emerge from the particle–matrix interface and the slip line density is higher where there is higher localized particle density.

which were used for the slip line analysis, it is evident that the slip lines began in regions which contained a clustering of SiC particles. The slip propagated from one cluster region to another, and deformation in the remainder of the samples is almost zero. The data obtained from the TEM investigation also indicated that the deformation is very localized in the higher volume fraction discontinuous composites. In the case of the 20 vol.% SiC–Al alloy composite, only in a small region (less than 3 mm from the fracture surface) is there an increase in dislocation density over that of the annealed sample in a sample which has been tested in tension to failure. The phenomenon of localized deformation was duplicated by an FEM analysis.

As the volume fraction of SiC is decreased, the degree of localization decreases, *i.e.* the 5 vol.% SiC–Al composite has a dislocation density (ρ) *vs.* distance from the fracture surface (x) relationship which is approaching that of the 0 vol.% composite. This is a change which one would intuitively guess at, and the reason that this ρ *vs.* x relationship is different from that of the 20 vol.% SiC–Al composite is due to the statistical nature of the clustering. The higher the volume fraction of the particles, the greater is the probability of obtaining a cluster containing a given number of particles and the greater is the probability of finding clusters within close proximity.

Although the FEM analysis can account for the localized deformation, the following question still remains to be addressed: why should plastic deformation initiate in the clustered region where there is a local high volume fraction of reinforcement when it is obvious that the higher the volume fraction of reinforcement, the stronger is the material and the less prone it should be to

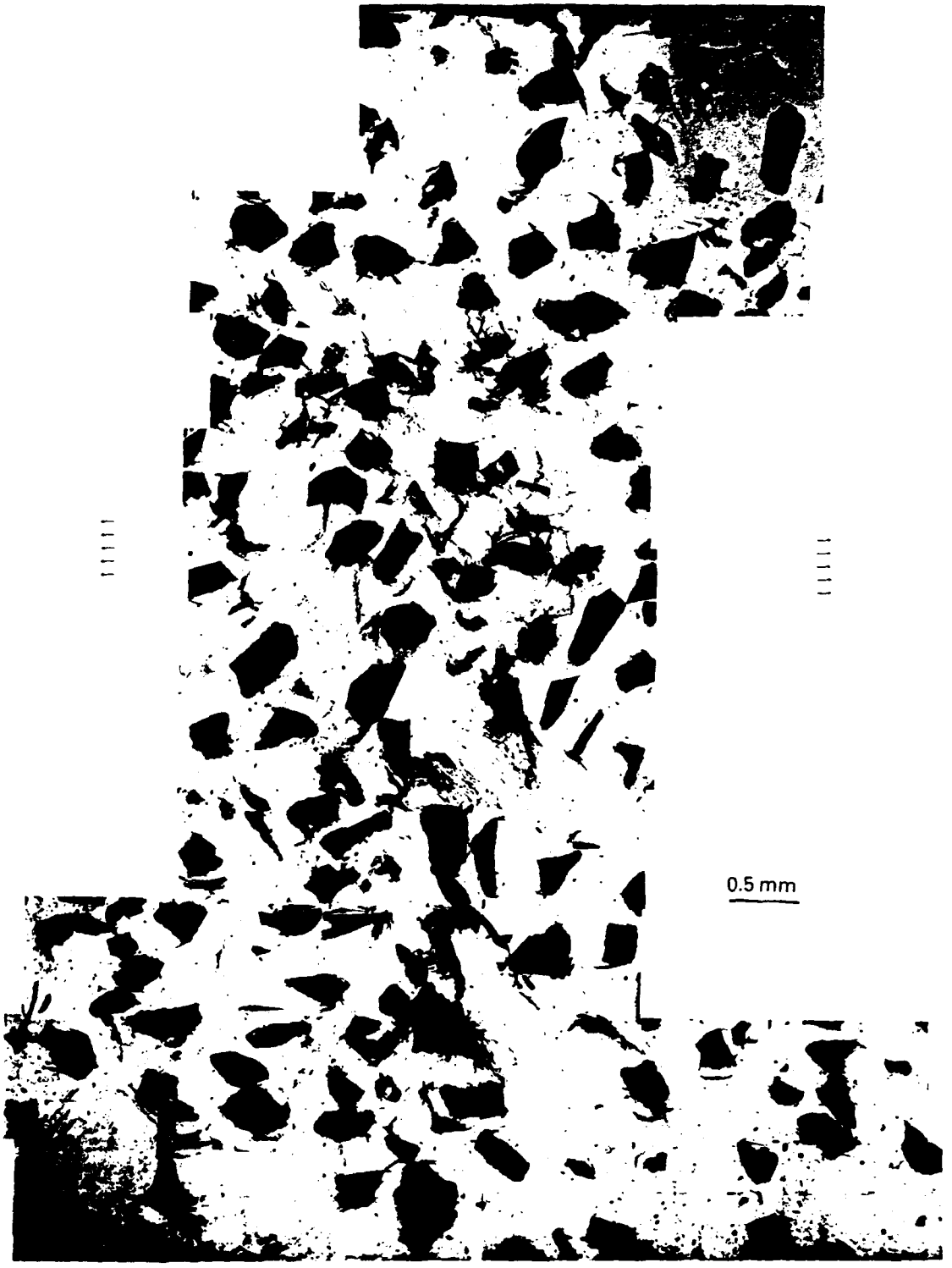

Fig. 15. Upon further straining, the density of the slip lines increases. However, they are limited to the localized region where there is a higher particle volume fraction. (The arrows indicate the direction of loading.)

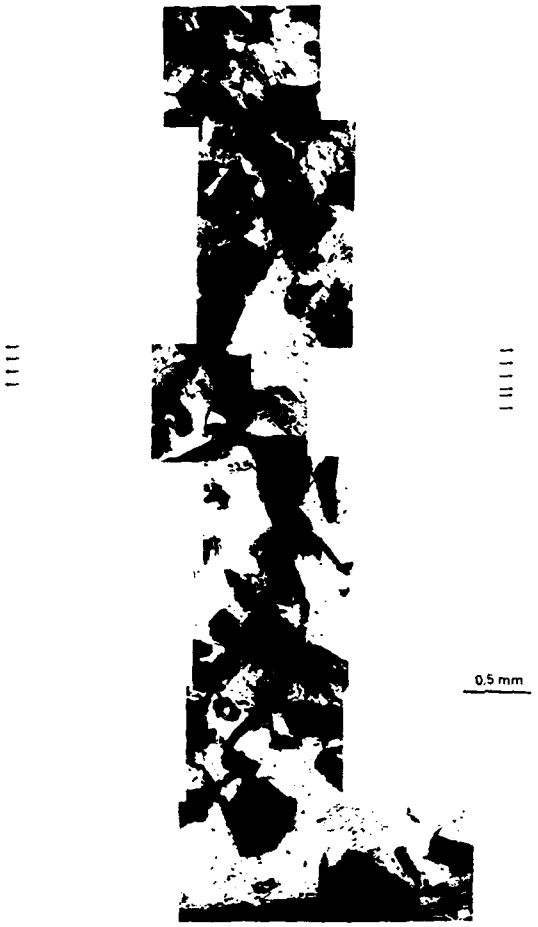

Fig. 16. As the external load increases, plastic deformation becomes more localized and finally a crack is formed within such a highly deformed region. (The arrows indicate the direction of loading.)

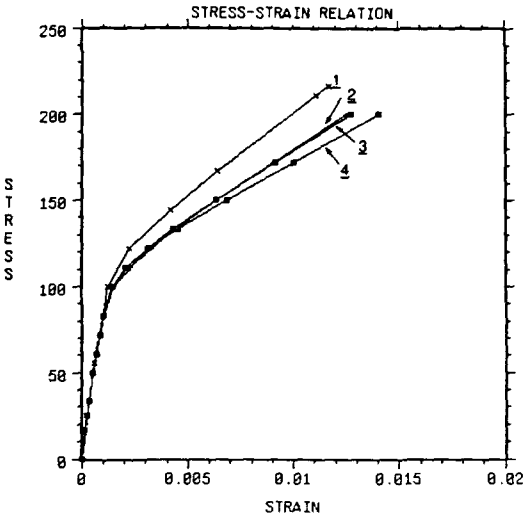

Fig. 17. Stress–strain curves produced as a result of clustering: curve 1, $S_v/2V = 1$, $S_v/2H = 1$; curve 2, $S_v/2V = 0.75$, $S_h/2H = 0.429$; curve 3, $S_v/2V = 0.5$, $S_h/2H = 0.143$; curve 4, $S_v/2V = 0.25$, $S_h/2H = 0.071$.

plastic deformation? To explain this phenomenon fully, it is necessary to consider the fact that deformation compatibility has to be satisfied when there is an inhomogeneous distribution of reinforcement particles, *i.e.* clustering. Since the clusters are stiffer, upon satisfying deformation compatibility, the stress would be distributed in such a way that the clusters would bear more load than the rest of the matrix. Secondly, since the local volume fraction is higher within clusters, for the same amount of deformation, the cluster must activate more slip systems in the matrix to accommodate the same amount of deformation. Figure 18(a) shows effective plastic strain as a function of global strain at various locations within the matrix as shown in Fig. 18(b). From the plot it can easily be seen that there exists a strong deformation gradient and the plastic strain as a function of external applied load between the fiber ends in the cluster is much higher than elsewhere in the matrix. The divergence of effective plastic strain at various locations in the matrix as the global applied strain approaches zero indicates that there is a large gradient on plastic deformation in the matrix owing to initial thermal residual stresses, and the initial flat region on some of the curves is an indication that the initial deformation in these regions is purely elastic, which may include possible unloading as in the case of that at the whisker tip. Figure 18(c) shows a comparison of effective plastic strain at the whisker ends in a regular and a clustered whisker distribution. From the figure it can be clearly seen that although whiskers within a regular distribution of whiskers have a higher plastic deformation rate at the whisker end as compared to the rest of the matrix [27], the clustered distribution has both a higher effective plastic strain rate and a higher effective plastic strain value. This signifies that the matrix material within the cluster is prone to plastic deformation, which is what is observed experimentally, as discussed in the previous section.

In order to characterize the response of the effective plastic strain to the external load at different locations in the matrix, the response of an imaginary homogeneous material was incor-

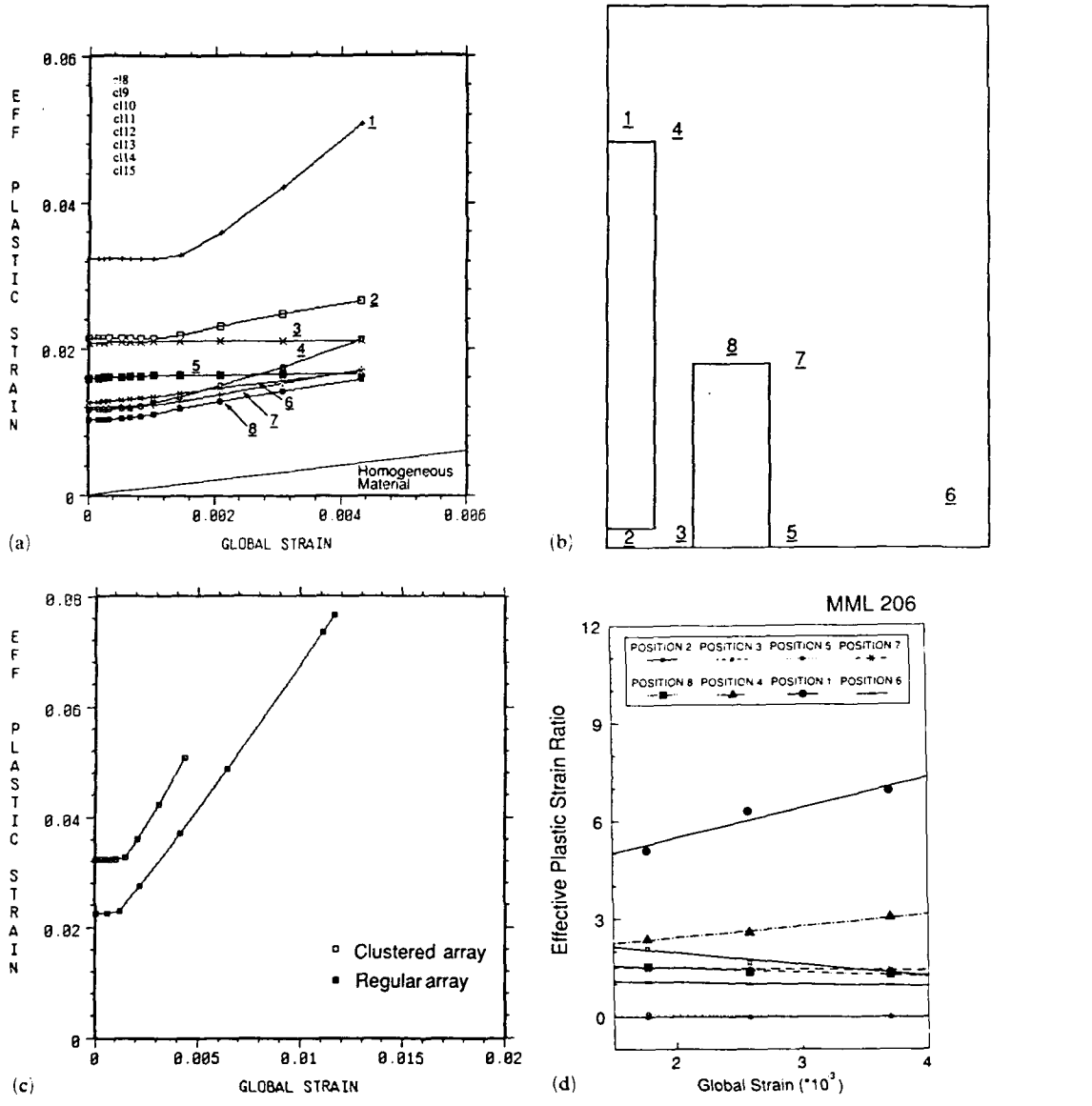

Fig. 18. (a) Localized effective plastic strain at various locations *vs.* global strain. "Homogeneous material" applies to a homogeneous material subject to a tensile load. (b) Locations where effective plastic strain is taken. (c) Effective plastic strain *vs.* global strain at whisker ends for clustered and regular arrays (at location 1) for clustered array as shown in (b). It is clearly seen that the clustered array has a higher effective plastic strain rate for the same global strain increment, which simply means the clustered arrangement of the reinforcement particles is more susceptible to external loading in terms of plastic deformation. (d) The deformation rate is higher within the reinforcement cluster except at locations near the longitudinal matrix-whisker interface.

porated into the plot. Because of the nature of homogeneity, the internal effective plastic strain is always equal to the external applied global strain. Furthermore, if localized deformation exists in the cluster, the ratio of the increase of the internal effective plastic strain to the increase of the external applied global strain, which may be defined as the internal effective plastic ratio, should be larger than that of a homogeneous material, which has a value of unity. Figure 18(d) shows internal effective plastic strain rate *vs.* applied global strain at various locations in the matrix. It

is clearly seen that except in the immediate region near the vertical interface of the reinforcement and matrix, the effective plastic strain ratio within the cluster is greater than that of a homogeneous material, while the ratio approaches unity at locations away from the cluster in the matrix. The effective plastic strain ratio of a homogeneous material is always unity.

The lack of voids at the matrix–whisker interface is probably related to several phenomena. First, it has been shown [28] that the bond between SiC and aluminum is very good. This bond is several times stronger than the bond between Fe_3C and iron. Secondly, there is a region of cold work, *i.e.* a high dislocation density region, around the whisker. As a result of this hardened region around the whisker, a triaxial stress develops in the matrix some distance away from the whisker. It is into this region that the crack propagates. The end result is that very few voids are found at the interface between SiC and aluminum.

5. Conclusions

From the experimental results and the FEM calculations it is possible to arrive at several conclusions.

(1) In discontinuous metal matrix composites containing a high volume fraction of particles and whiskers, the deformation is highly localized.

(2) There are manifestations of three distinct localized deformations: (a) there are very narrow "necks" in fracture samples; (b) the close-in dislocation density is confined to a small region very close to the fracture surface; (c) the slip line generation is confined to a localized region.

(3) The FEM study has shown that the effectiveness of strengthening from the reinforcement in the composites is reduced if there is clustering of the reinforcement. Internal deformation maps generated by FEM have shown that deformation is more localized in comparison to composites with uniformly distributed reinforcement, and deformation in the cluster is more severe in the reinforcement cluster than in the remainder of the matrix.

Acknowledgments

This research was supported by the Office of Naval Research under Contract N00014-K-85-0007. The positive interactions with Dr. S. Fishman of the Office of Naval Research are greatly acknowledged. The authors wish to acknowledge the assistance of Dr. S. B. Wu in the performance of the tensile tests. The authors wish to acknowledge the continued support of the Argonne National Laboratory HVEM facility, especially Dr. E. Ryan.

References

1 R. J. Arsenault, Y. Flom, K. N. Subramanian and M. A Iman (eds.), *Structure and Deformation of Boundaries*, AIME, New York, 1986, p. 261.
Y. Flom and R. J. Arsenault, *J. Met., 38* (1986) 31.
2 Unpublished results, Metallurgical Materials Laboratory, University of Maryland, 1986.
3 B. I. Edelson and W. M. Baldwin, *Trans. Am. Soc. Met., 55* (1962) 55.
4 J. Gurland and J. Plateau, *Trans. Am. Soc. Met., 56* (1963) 442.
5 A. Gangullee and J. Gurland, *Trans. Metall. Soc. AIME, 239* (1967) 269.
6 J. Gurland, *Trans. Metall. Soc. AIME, 227* (1963) 1146.
7 C. T. Liu and J. Gurland, *Trans. Metall. Soc. AIME, 224* (1968) 1535.
8 C. T. Liu and J. Gurland, *Trans. Metall. Soc. AIME, 61* (1968) 156.
9 J. Gurland, Fracture of metal-matrix particulate composites, in L. J. Broutman and R. H. Krock (eds.), *Modern Composite Materials*, Addison-Wesley, New York, 1969, p. 170.
10 I. L. Mogford, *Metall. Rev., 114* (1967) 12, 49.
11 R. H. Van Stone, R. H. Merchant and J. R. Low Jr., *ASTM Spec. Tech. Publ. 556* (1974) 93.
12 T. B. Cox and J. R. Low, *Metall. Trans., 5* (1974) 1457.
13 G. T. Hahn and A. R. Rosenfield, *Metall. Trans. A, 6* (1975) 653.
14 G. G. Garret and J. F. Knott, *Metall. Trans. A, 9* (1978) 1187.
15 K. H. Schwalbe, *Eng. Fract. Mech., 9* (1977) 795.
16 G. LeRoy, J. D. Embury, G. Edwards and M. F. Ashby, *Acta Metall., 29* (1981) 1509.
17 R. C. Bates, Modeling of ductile fracture by microvoid coalescence for prediction of fracture toughness, in J. M. Wells and J. B. Landes (eds.), *Proc. 113th AIME Conf.*, AIME, New York, 1985, p. 117.
18 W. W. Gerberich, Interaction of microstructure and mechanism in defining K_{IC}, K_{ISCC} or K_{th} values, in J. M. Wells and J. B. Landes (eds.), *Proc. 113th AIME Conf.*, AIME, New York, 1985, p. 49.
19 D. Firrao and R. Roberti, On the mechanism of ductile fracture nucleation ahead of sharp crack, in J. M. Wells and J. B. Landes, *Proc. 113th AIME Conf.*, AIME, New York, 1985, p. 165.
20 R. J. Arsenault, *Mater. Sci. Eng., 64* (1984) 171.
21 R. J. Arsenault and S. B. Wu, *Scr. Metall., 22* (1988) 762.
22 M. Vogelsang, R. J. Arsenault and R. M. Fisher, *Metall. Trans. A, 17* (1986) 379.

23 R. J. Arsenault, L. Wang and C. R. Feng, *Acta Metall.*, (1991) in the press.
24 A. S. Keh, *Direct Observation of Lattice Defects in Crystals*, Wiley-Interscience, New York, 1962, p. 213.
25 P. B. Hirsch, A. Howie, R. B. Nicholson, D. W. Pashely and M. J. Whelan, *Electron Microscopy of Thin Crystals*, Butterworths, London, 1965, p. 416.
26 Y. Flom and R. J. Arsenault, *Mater. Sci. Eng.*, *75* (1985) 151.
27 N. Shi and R. J. Arsenault, submitted to *J. Comput. Tech. Res.*
28 Y. Flom and R. J. Arsenault, *Mater. Sci. Eng.*, *77* (1986) 191.

Acta metall. mater. Vol. 39, No. 1, pp. 47–57, 1991
Printed in Great Britain.

0956-7151/91 $3.00 + 0.00

STRENGTHENING OF COMPOSITES DUE TO MICROSTRUCTURAL CHANGES IN THE MATRIX

R. J. ARSENAULT, L. WANG and C. R. FENG
Metallurgical Materials Laboratory, University of Maryland, College Park, MD 20742-2115, U.S.A.

(*Received* 23 *December* 1989; *in revised form* 22 *June* 1990)

Abstract—The addition of discontinuous silicon carbide (SiC) to aluminum (Al) alloys can result in a five-fold increase in the yield stress. The magnitude of the increase is obviously a function of the volume fraction and the particle size of the SiC. Previously, it was proposed that the strength increase due to SiC addition to Al alloys was the result of change in the matrix strength, i.e. an increase in dislocation density and a reduction of subgrain size. The data obtained from a series of experiments indicate that dislocation density increases with an increase in volume fraction of SiC and decreases with an increase in particle size. The subgrain size decreases as the volume fraction increases and increases as the particle size increases. There is a good correlation between the microstructural changes in the matrix and the changes in the yield stress of the composites.

Résumé—L'addition de carbure de silicium (SiC) discontinu à des alliages d'aluminium (Al) peut conduire à une élévation d'un facteur 5 de la limite élastique. La grandeur de cette augmentation est évidemment fonction de la fraction volumique et de la taille des particules de SiC. On a déjà suggéré que l'augmentation de la résistance mécanique due à l'addition de SiC dans les alliages d'aluminium est le résultat d'un changement de la résistance mécanique de la matrice, c'est à dire d'une augmentation de la densité de dislocations et d'une réduction de la taille des sous-grains. Les données obtenues pour une série d'expériences indiquent que la densité de dislocations croît lorsque la fraction volumique de SiC augmente et décroît lorsque la taille des particules croît. La taille des sous-grains décroît lorsque la fraction volumique augmente et croît lorsque la taille des particules diminue. Il existe une bonne corrélation entre les changements microstructuraux dans la matrice et les variations de la limite élastique des composites.

Zusammenfassung—Zugabe von diskontinuierlichem Siliziumkarbid (SiC) zu Aluminium (Al)-Legierungen kann die Fließspannung verfünffachen. Diese Erhöhung hängt offenkundig vom Volumantiel und der Teilchengröße des SiC ab. Früher wurde dargelegt, daß diese Festigkeitserhöhung von einer Änderung in der Matrixfestigkeit, d.h. einem Anstieg in der Versetzungsdichte und einer Verringerung der Subkorngröße, herrührt. Eine Reihe von erhaltenen experimentallen Ergebnissen zeigt, daß die Versetzungsdichte mit zunehmenden Volumantiel von SiC ansteigt und mit zunehmender Teilchengröße abnimmt. Die Subkorngröße nimmt mit zunehmendem Volumanteil ab und mit zunehmender Teilchengröße zu. Zwischen den Änderungen in der Mikrostruktur der Matrix und den Änderungen der Fließspannung des Materials besteht gute Korrelation.

1. INTRODUCTION

The concept of strengthening due to an increase in dislocation density has been in existence for several decades, probably since shortly after the original proposal of edge dislocations by Orwan *et al.* [1]. Over the subsequent years, there have been numerous investigations which have correlated a strength increase with an increase in dislocation density. The strengthening due to a reduction in subgrain size is not as old as the concept of strengthening due to an increase in the dislocation density [2]. However, the correlation has been demonstrated quite clearly by several individuals; in particular, by McQueen *et al.* [3].

It had been proposed by Arsenault [4] a few years ago that the strengthening of Al and Al alloys due to the addition of discontinuous SiC reinforcements occurred as a result of generation of dislocations which produced an increase in dislocation density and a reduced subgrain size in the matrix. The generation is due to a difference in thermal coefficient of expansion between the matrix and the reinforcement (ΔCTE). The presence of the high dislocation density within the matrix has been demonstrated along with a very small subgrain size. An *in situ* investigation has demonstrated the validity of the ΔCTE mechanisms as a means by which the high dislocation density is produced within the matrix [5].

Further, it has been shown that a very simple model based on prismatic punching is capable of producing an adequate dislocation density [6]. However, it should be clearly pointed out that this model will only predict the lower limit of the dislocation density. Attempts to calculate the upper limit of the dislocation density due to the ΔCTE effect have

proven unsuccessful, for all of the calculations predicted a very high dislocation density, i.e. approaching infinity, which obviously is not correct.

However, there remain several questions pertaining to the details of the strengthening mechanism of discontinuously reinforced metal matrix composites based on the strengthening of the matrix due to a change in the microstructure of the matrix.

The first question is related to transmission electron microscopy (TEM) procedures for determining dislocation densities; (a) does the sample preparation technique, i.e. dimpling and ion milling, introduce damage into the TEM foil? and (b) if a thin region of the foil is examined (i.e. the viewing region) at 100–200 kV, will a lower dislocation density be observed? In regard to (b) of the above question, there have been a few investigations which have determined the dislocation density as a function of foil thickness and the most recent are by Fajita *et al.* [7–9]. In the case of pure Al, it was found that the foil thickness had to be greater than 1 μm to obtain a bulk dislocation density. The question arises, since SiC/Al is not high purity Al, does this requirement of foil thickness still apply?

The second question: is there an overall relationship between dislocation density (ρ), subgrain size (λ), reinforcement particle size (D) and volume fraction (V), and the increase in the yield stress of the composite? There have been several investigations where the dislocation density was determined for a specific particle size and volume fraction, but there have been no systematic investigations of these parameters. Also, there are no systematic investigations of the subgrain size as a function of particle size and volume fraction.

Another question: is it possible to increase the strength of the matrix sufficiently to account for the strengthening? In other words, if the Al matrix alone (with no SiC present) had the same dislocation density as in the composite, would the Al matrix have the same strength as the composite? Is it possible to increase the dislocation density and reduce the subgrain size within the Al alloy matrix by cold working to approach the yield strength of a composite containing 20 V% reinforcement in the same Al alloy matrix.

An investigation was undertaken to address the questions raised above.

2. MATERIALS AND TESTING

A discussion of materials and testing will be divided into three portions corresponding to:

2.1. Composite materials;
2.2. Cold rolled 0 V% 1100 Al alloy;
2.3. High purity Al.

†Now, Advanced Composite Materials of Greer, South Carolina.
‡Composite Specialties of Chatsworth, California.

2.1. Composite materials

All of the composite materials were produced by a powder metallurgical procedure. The Al alloy powders were mixed with particulate or whisker SiC, hot-compacted and hot-extruded into 12.7 mm diameter rods or hot pressed into a plate. The 0, 5 and 20 V% SiC whiskers/6061 Al alloy composites plus the 0 V%/1100 Al alloy composites were purchased from ARCO Silag†. The 20 V% SiC-250 μm particulate/1100 Al alloy composite was purchased from DWA‡ in the form of a plate. The remainder of the material was produced in the Metallurgical Materials Laboratory of the University of Maryland in the form of an extruded rod.

From the extruded rod and plate, tensile samples were machined into a configuration as described elsewhere [4]. Prior to tensile testing, the samples were annealed for 12 h at 803 K and furnace cooled. All of the tensile testing was conducted at room temperature at a strain rate of $10^{-4}\,s^{-1}$.

Short sections of extruded rod (12 mm) and portions of as-pressed plate were annealed at 803 K for 12 h and furnace cooled. From these sections and portions, 0.5 mm thick disks were electrically discharge machined. The procedure for thinning the TEM foils and the method of determining the dislocation densities is given elsewhere [5]. The electron microscopy investigation involved the use of two microscopes, a JEOL 100 CX operating at 100 kV and the Argonne National Laboratory modified Kratos/AEI EM7 HVEM operated at 1 MV.

2.2. Cold rolled 0 V% 1100 Al alloy

The cold rolled strips were produced by taking 0 V% 1100 Al alloy material purchased from ARCO Silag and rolling without any intermediate annealing until a reduction in thickness of ~90% was obtained. From the cold rolled strips, "dog bone" shaped tensile samples were machined with a 24.5 mm gage length and a width of 2.6 mm and a thickness of 1.42 mm.

The tensile sample preparation and testing were the same as described in Section 2.1. This also applies to the TEM foil preparation and examination.

2.3. High purity Al

Relatively high purity Al (99.99%) was obtained in the form of a rod, 12.7 mm dia from ALCOA as a gift. This material was annealed for 12 h at 803 K and furnace cooled. The TEM foils of high purity Al were produced by two different procedures. Some of the foils were produced using the electrical discharge machining, dimpling and ion milling procedure, using the same operating parameters as used for the composite TEM foils (Section 2.1). The other samples, after being cut into 0.5 mm thick disks by electrical discharge machining, were electrochemically thinned using a jet polishing device. The foils were examined at 100 kV and 1 MV.

3. RESULTS

The discussion of the results will be divided into three portions:

3.1. Yield strength vs particle size and yield strength vs volume fraction;
3.2. Dislocation density determination;
3.2.1. Dislocation density due to foil preparation procedures and TEM operating voltage;
3.2.2. Dislocation density and subgrain size vs particle size and volume fracture;
3.3. Changes in dislocation density and subgrain size due to cold rolling and the determination of the yield strength.

3.1. Yield strength

Of interest is the incremental increase in the yield stress (which is defined as the stress at a plastic strain of 0.2%) due to the addition of the reinforcement. Therefore, the yield stress of the 0 V% matrix alloy is subtracted from the yield stress of the composite. The incremental yield stress ($\Delta\sigma_y$) is what is plotted and listed in all cases. The variations in $\Delta\sigma_y$ of the SiC whisker 6061 Al alloy composites were considerably less than that in the SiC/1100 Al alloy composites. This is simply due to the greater homogeneity of the reinforcement within the matrix in the 6061 Al alloy composites.

As expected, as the size of the SiC particulate increased, the strength decreased, as shown in Fig. 1. The squares represent the average of at least three tests and there could be as many as ten tests for a given particular size. The arrow bars define the range of scatter. The ultimate strength is only slightly larger than the yield strength indicating that the work hardening rate past yielding is small. The uniform strain was fairly constant, between 3 and 4% for the 0.5–9 μm composite materials, then increasing to 6–7% uniform strain for the 20 and 70 μm particulate and slightly larger on average for the 250 μm particulate size composites.

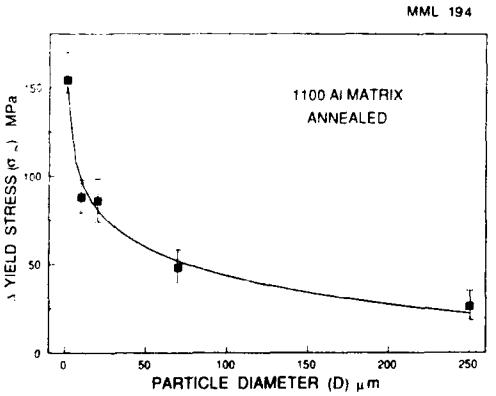

Fig. 1. The change in the yield stress as a function of SiC particulate size. The matrix is a 1100 Al alloy. The composite is in the annealed condition.

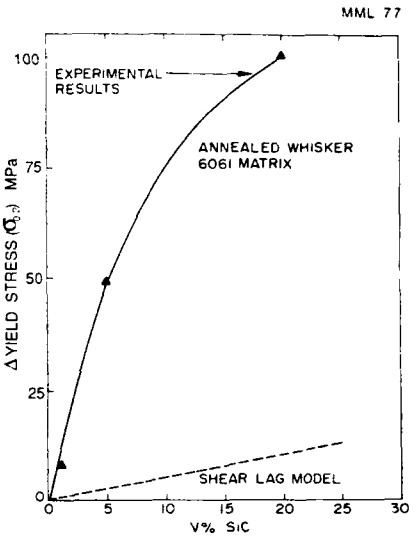

Fig. 2. The change in the yield stress as a function of the volume fraction of SiC (SiC whisker is ~0.5 μm in dia (and on average ~2 μm long). The matrix is a 6061 Al alloy. The composite is in the annealed condition.

Increasing the volume fraction of SiC resulted in an increase in strength (Fig. 2). Experimentally, it was observed that $\Delta\sigma_y$ increases to 100 MPa due to the addition of 20 V% SiC whisker. The classical-continuum-load transfer-shear lag model [10] would predict ~15 MPa increase in strength, which is indicated by the dashed line in Fig. 2.

3.2. Dislocation density determinations

3.2.1. Dislocation density due to foil preparation procedures and TEM operating voltage. The two different series of investigations were undertaken to determine if the TEM foil preparation procedure was introducing damage into the composite. The first investigation involved preparing TEM foils from annealed and furnace cooled high purity Al rods by two different routes. The first route involved electrical discharge machining, followed by dimpling using 0.25 μm diamond paste and then followed by ion milling, i.e. the same procedure which is used for the composites. The second technique involved electrical discharge machining, followed by electro-chemically thinning. Figure 3(a) is a micrograph taken of an ion milled thinned sample and Fig. 3(b) is taken from a sample which was electrochemically thinned. As can be seen, the dislocation densities are low in both cases, and the dislocation configurations are the same. The only recognizable difference between the ion milled and the electro-chemically thinning is the "mottled" appearance of the ion milled micrograph. This mottled appearance is the result of the non-uniform thickness of the ion thinned foil; the reason for the non-uniformity is not known.

Fig. 3. (a) A transmission electron micrograph of high purity Al in the annealed condition thinned by dimpling and ion milling. (b) A transmission electron micrograph of high purity Al in the annealed condition thinned by dimpling and jet polished.

However, it is safe to conclude that the dimpling and ion milling do not produce any detectable increase in the dislocation density.

The second investigation was related to foil thickness (viewing thickness) as related to dislocation density. If the operating voltage of the TEM is

100 kV, the thickness of the foil in which dislocations may be viewed is 0.2–0.4 μm. However, if the operating voltage is 1 MV, the thickness of the foil increases to 1–2 μm. If we consider the micrograph shown in Fig. 4, we can see the effect of foil thickness on the dislocation densities. Figures 4(a) and (b) are micrographs taken at 100 kV and the foil thickness in Fig. 4(b) in which a few dislocations are visible is 0.3 μm and the dislocation density is $1.6 \times 10^{13}\,m^{-2}$. Figure 4(c) and (d) are micrographs taken at an operating voltage of 1 MV. The dislocation density in Fig. 4(d) is $4.5 \times 10^{13}\,m^{-2}$ and the foil thickness is 0.9 μm. Figures 4(a), (b), (c) and (d) are micrographs taken from the same area of a foil under the same operating diffraction condition, only a thinner area around the rim of the hole is transparent for the 100 kV microscope. This is a general result for all composites examined. If a low operating voltage

Fig. 4.(a) *Caption overleaf.*

Fig. 4.(b,c) *Caption on facing page.*

Fig. 4. (a) A transmission electron micrograph taken at an operating voltage of 100 kV. (b) A transmission electron micrograph taken at an operating voltage of 100 kV. This micrograph is of the enclosed area in (a). (c) A transmission electron micrograph taken at an operating voltage of 1 MV. (d) A transmission electron micrograph taken at an operating voltage of 1 MV. This micrograph is of the enclosed area in (c).

is used, i.e. 100–200 kV, the apparent dislocation density is low compared to the dislocation density obtained from foils examined at 1 MV.

A factor which has to be recognized when examining foils at high accelerating voltages is the possibility of radiation damage resulting in the formation of dislocation loops. It was observed that if a given area was observed for $\sim\frac{1}{2}$ h at 1 MV and the dislocation density was low ($< 1 \times 10^{13}$ m^{-2}), then dislocation loops became visible from the condensation of the radiation damage. These dislocation loops were very small ($< 0.1\ \mu$m) and could be readily distinguished from the dislocation produced by the ΔCTE and were never counted when determining the dislocation density.

Therefore, in order to obtain realistic measures of dislocation density in SiC Al composites, it is necessary to examine thicker foils which needs a operating voltage (800 kV to 1 MV).

3.2.2. Dislocation density and subgrain size vs particle size and volume fraction. The determination of dislocation density by TEM is fraught with many perils. Two of the many possibilities have already been addressed, i.e. introduction of dislocations during sample preparation and the effect of the foil thickness on the observed density. There are certainly several others, especially if numerous slip systems are operative as they certainly are in composites. In a two-beam condition, this means that several operative $\boldsymbol{g}$-vectors have to be considered, but when operating at 1 MV, a many-beamed condition can easily be used and a larger fraction of the dislocations present become visible. However, it is still necessary to tilt the sample and take several different pictures. Also, there is an inherent variation of dislocation density from place to place within the matrix. For example, the dislocation density is higher near the particles and decreases with distance away from the particle. This variation is especially critical in large particle size and low volume fraction samples. In order to overcome this difficulty, it is necessary to make measurements on many micrographs. The procedure for measuring the dislocation density is given elsewhere [5]. The data given for each condition (i.e. particle size or volume fraction) in Figs 5 and 6 represent tens to hundreds

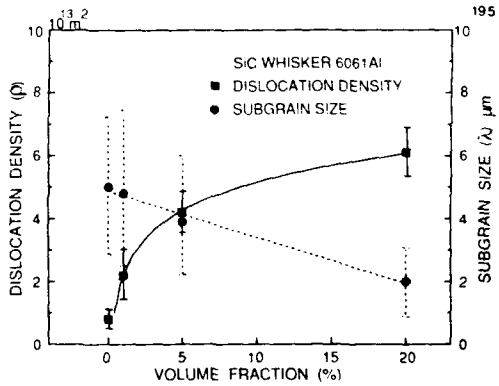

Fig. 5. The change in dislocation density as a function of volume fraction of SiC (SiC whiskers have a length to diameter on average of ~2 and the dia ~0.5 μm).

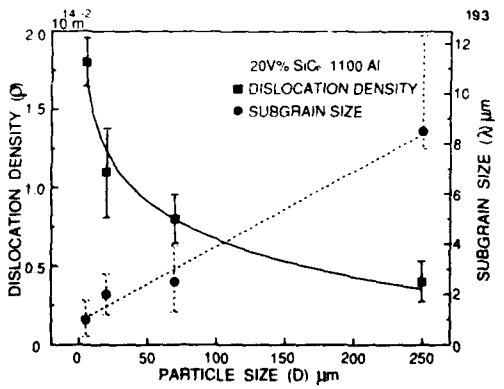

Fig. 6. The change in dislocation density as a function of particulate size.

Table 1. Comparison of 9 μm particle size 20 V% SiC Al composite with cold rolled 0 V% 1100 Al composite

Material	Dislocation density ($\rho \times 10^{14}$ m^{-2})	Subgrain size ($\lambda \times \mu$m)	Δ Experiment yield stress ($\Delta\sigma_{0.2\%}$, MPa)
20 V% SiC_p	1.1	2	88
0 V% CR	0.15	2	116

Δ Experimental yield stress = the yield stress of the composite minus the yield stress of 0 V% matrix.

of micrographs of a given foil and 5–6 different foils were examined for each condition. The dislocation densities reported are the *average* dislocation densities in the matrix of annealed samples. As stated above, the dislocation density is not uniform in the matrix.

Upon increasing the volume fraction, the dislocation density increases, but upon increasing the volume fraction, the subgrain size decreases as shown in Fig. 5, and upon increasing the particle size, the opposite is the case, the dislocation density decreases (and the subgrain size increases) as the particle size increases (Fig. 6).

3.3. *Effect of cold rolling*

The yield strength and the dislocation density were determined of a 0 V% 1100 Al alloy which had been cold rolled ~90%. The cold rolling reduced the subgrain size slightly from 5–10 μm to 2 μm, but there was a significant increase in dislocation from less than 10^{10} m^{-2} to 1.5×10^{13} m^{-2}. The cold rolling increased the yield strength from 30 to 146 MPa. If a comparison is made with the 9 μm SiC particle size in 20 V% 1100 Al alloy matrix composite, it can be seen that the $\Delta\sigma_y$ is greater for the cold rolling material than that of the SiC_p 1100 Al alloy composite (Table 1). However, the interesting point is that the dislocation density in the composite is much greater than that of the 0 V% 1100 Al alloy cold rolled material.

4. DISCUSSION

The discussion will follow along the lines of the questions raised in the Introduction.

4.1. *Dislocation and subgrain size determinations*

From the investigation of high purity Al, it was shown that the dislocation density in the foils, produced by dimpling and ion milling was the same as that in the electrochemically produced foils. A main concern of ion milling is that the heat generation occurs and that this heat generation would result in a decrease in the dislocation density. In terms of dimpling, which involves grinding the foil with 0.25 μm diamond paste, this could plastically deform the sample, i.e. introduce dislocations. These dislocations would have an entirely different appearance as compared to the remnant dislocations which remain from the long term high temperature annealing. The outcome of this investigation is that the dimpling and ion milling do *not* introduce any dislocations into the TEM foil.

In regard to the question raised concerning the viewing thickness of the TEM foil, it has been previously shown for the case of high purity Al that the viewing thickness of the TEM foil has to be greater than 1 μm in order to obtain a dislocation density representative of bulk samples [7–9]. High purity Al is a homogeneous material and the main factor contributing to lowering dislocation density is the image force acting on the dislocations within the foil. In thinner foils, the presence of the image force should remove a proportionately larger number of dislocations. In the case of SiC/Al alloy composites, we are not dealing with a homogeneous material. Besides the image force which is still present, there are other factors which contribute to the loss of dislocations from the thinned foil. There are thermal residual stresses within the SiC/Al alloy composite prior to thinning. If we consider the points labeled 1 and 2 in Fig. 7, there is a tensile residual stress acting in the direction A–A', B–B', C–C' and D–D'. If the sample is cut along the lines A–A' and B–B', the stress at the surfaces will have to relax to zero. A simple manner of stress relaxation is by dislocation motion, i.e. dislocation motion out of the foil. For a thinner foil, there will be a larger proportional dislocation loss from the sample. The image force is still present and would lead to a further reduction of the dislocation density in the thinner area of the foil, just as in the homogeneous material. Therefore, in order to obtain reasonable measures of the dislocation density of a SiC Al alloy composite, it is necessary to examine thicker portions of the TEM foil, which means examining the foil at 1 MEV. The determination of the subgrain size is not as dependent on foil thickness or the foil preparation procedure.

4.2. *Correlation between microstructural changes and yield stress*

The increase in the yield stress with an increase in the volume fraction or the decrease of yield stress with an increase in the particle size is to be expected. Correspondingly, the dislocation density and the subgrain change in the expected manner. However, it is necessary to consider if *the changes in the yield stress can be related to the changes in dislocation density and the subgrain size.*

Before considering these correlations, it is necessary to point out again that the dislocation density within the matrix is not uniform, and secondly, there can be a significant difference in stress at the proportional limit and the yield stress defined at a plastic strain of 0.2%. This would indicate that there is significant work hardening on a local scale occurring within the matrix. The reason for stating that it is on a local scale is due to the fact that very little plastic strain is occurring between the proportional limit and the defined yield stress. It has been observed that the initial, and in some cases, the entire plastic

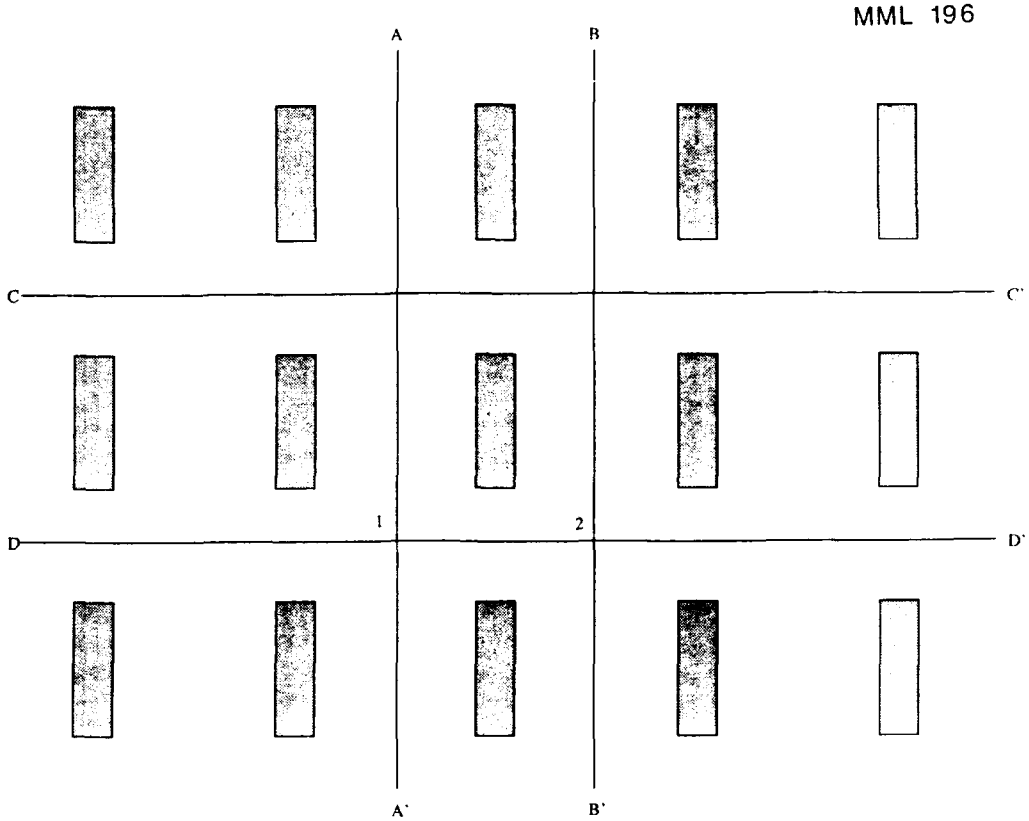

Fig. 7. A schematic arrangement of SiC whiskers and platelets with arbitrary thinning to a TEM foil.

Table 2. Predicted increase in yield strength of 20 V% SiC 1100 matrix and experimentally measured values

Particle size D (μm)	$\Delta\sigma_\rho$ (MPa)	$\Delta\sigma_{SG}$ (MPa)	$\Delta\sigma_{res}$ (MPa)	$\Delta\sigma_{ypred}$ (MPa)	$\Delta\sigma_{yexp}$ (MPa)
0.5	126.6	131	17	240.6	153
9	99	69	17	151	88
70	79	20	17	82	69
250	59.7	0-13.8	17	42.7-56.5	26

$\Delta\sigma_{yexp}$ = the yield stress defined at 0.2% plastic strain minus the 0.2% yield stress of the 0 V% 1100 matrix, $\Delta\sigma_\rho$ = the predicted increase due to the increased dislocation density; $\Delta\sigma_{SG}$ = the predicted increase due to the reduced subgrain size; $\Delta\sigma_{res}$ = the predicted average tensile residual stress; $\Delta\sigma_{ypred}$ = the sum of $\Delta\sigma_\rho + \Delta\sigma_{SG} - \Delta\sigma_{res}$.

deformation occurs in regions containing higher than average volume fraction of particulate or whisker [11]. The dislocation density is the largest on average in the regions of higher than average volume fraction of particulate or whisker, but, there is not an overall change in the density of dislocations in the sample. Therefore, an assumption is made that the *average* increase in the dislocation density is small due to the initial loading to a plastic strain of 0.2%, and that the stress field which opposes dislocation motion had a strain of 0.2% which is due to the average dislocation density of the annealed undeformed sample. Therefore, we can use the well-established relationship

$$\Delta\sigma_y = \alpha\mu b\sqrt{\rho}$$

where $\Delta\sigma_y$ is the increase in the yield stress of the composite over that of the 0 V% matrix material, α is a constant and Hansen [12] has shown that for Al, this is 1.25, μ is the shear modulus of the matrix (2.64×10^4 MPa), $\mathbf{b}$ is the Burgers vector (2.86×10^{-10} m) and ρ is the dislocation density.

Then we can calculate the incremental increase in the strength due to the presence of the increase in dislocation density. This is the increase which should be added to the annealed 0 V% Al alloy matrix yield stress. In Table 2 are listed the incremental increases in the strength due to an increase in dislocation density as a function of changes in particle size at a constant volume fraction of 20%. The incremental increase in strength is large for the case 0.5 μm particle size, and decreases as the particle size

Table 3. Predicted increase in yield stress of 6061 Al alloy as a function of volume fraction of SiC whisker

Volume ($V\%$)	$\Delta\sigma_\rho$ (MPa)	$\Delta\sigma_{SG}$ (MPa)	$\Delta\sigma_{res}$ (MPa)	$\Delta\sigma_{ypred}$ (MPa)	$\Delta\sigma_{yexp}$ (MPa)
1	37.7	0	1.7	36.0	6.9
5	56.6	7.0	8.6	55.0	52
20	70	48.3	34.5	83.8	100

$\Delta\sigma_{yexp}$ = the yield stress defined at 0.2% plastic strain minus the 0.2% yield stress of the 0 $V\%$ 1100 matrix; $\Delta\sigma_\rho$ = the predicted increase due to the increased dislocation density; $\Delta\sigma_{SG}$ = the predicted increase due to the reduced subgrain size; $\Delta\sigma_{res}$ = the predicted average tensile residual stress; $\Delta\sigma_{ypred}$ = the sum of $\Delta\sigma_\rho + \Delta\sigma_{SG} - \Delta\sigma_{res}$.

increases. In the larger particle size range, the predicted incremental increase in strength due to the increased dislocation density alone exceeds the increase in the experimental yield stress.

If we consider the increase in dislocation density with the increase in volume fraction, it is obvious that the strengthening due to the increase in dislocation density alone is very large (Table 3). In this case, it is necessary to subtract out the dislocation density of the 0 $V\%$ material, for this is appreciable when considering smaller volume fractions. In a case of particle size increase, this subtraction is not necessary for the dislocation density of the 0 $V\%$ annealed 1100 Al alloy matrix was very low.

In terms of strengthening due to a reduction in subgrain size, it is necessary to rely on the data of McQueen [3]. In Table 2 are listed the predicted increases in strength due to a reduction in the subgrain size $\Delta\sigma_{SG}$. The subgrain size of the 1100 Al matrix is much larger than the subgrain size of the composite so a subtraction is not necessary. The amount of strengthening due to a reduction in subgrain size in the small particle size range is greater than that in the large particle size range. If we consider the effect of volume fraction on the change in the subgrain size, in this case, it is necessary to subtract the increment of 0 $V\%$. The increase in strength due to the reduction in subgrain size becomes predominant at 20 $V\%$.

Although the increase in the dislocation density and the decrease in subgrain size are the major factors affecting the strength change of the matrix, there are other possible contributions to the strength change of the matrix [13]. These include residual stresses, differences in texture between the composite matrix and the matrix material without reinforcement, classical composite strengthening (i.e. load transfer) and dispersion strengthening.

The average residual stress is the only factor which has to be considered; the other factors are very small or zero [13]. The residual stress in the matrix is in tension [14] and the magnitude depends upon the volume fraction, morphology and size of the reinforcement, the type of alloy of the matrix, and the effective temperature change. In the calculations of Taya and Arsenault [14] it was assumed that the thermal stresses were completely relieved in the temperature range from the annealing temperature down to 473 K. From 473 K to room temperature, it was assumed that there was no plastic relaxation of the thermal stress and the thermal stress which developed between 473 K and room temperature became the residual stress. The residual stress increases almost linearly with an increase in volume fraction, and whiskers result in a larger residual stress than aligned platelets. In the case of spherical particles, the average residual stress in the matrix is pure hydrostatic tension which would have no effect on the long range dislocation motion (and hence, yielding). The analytical analysis of Arsenault and Taya [14] indicates that the size of the reinforcement would have no effect on the average residual stress, but in actuality, the average residual stress probably decreases as the size of the reinforcement increases. This reduction is due to greater than predicted dislocation generation because there would be less interference from dislocations generated by neighboring particles. To recap, the greater than predicted generation for the large particle size does not mean that the dislocation density is greater in larger particle size. It means that the average dislocation density, for example, for the 250 μm particulate SiC/1100 Al composite, would be greater than that predicted by the simple model of Arsenault and Shi [6]. The experimental average dislocation density is 3×10^{13} m^{-2}, whereas the predicted value is 3×10^{11} m^{-2}.

Since the average residual stress is in tension, it would be a negative contribution to strengthening of the composite. The values in Tables 2 and 3 are from the analytical predictions of Arsenault and Taya [14].

In general, the predicted increase in the yield strength is much larger than the experimentally determined yield strength. There are at least two possible explanations for this discrepancy. The first possibility is that the value taken for the constant α in equation (1) is too large. The values reported in the literature for α range from 0.5 to 1.25. The second possibility is that the assumption of using an average dislocation density is not valid for the plastic strain at 0.2% and may be due to the motion of dislocations in the matrix where the dislocation density is much lower than the average density. This certainly could account for the discrepancy in the 250 μm particle size composite and the 1 $V\%$ composite where the variation in the dislocation density is the greatest.

4.3. *Strengthening of the matrix*

As discussed in the Introduction, there is a question as to whether the matrix can be strengthened to the required levels by changes in the microstructure, i.e. can there be a sufficient increase in the dislocation density or a sufficient decrease in the subgrain size?

The cold rolled investigation has shown that the 0 $V\%$ 1100 Al alloy material can have a yield stress which is comparable in strength to a 20 $V\%$ SiC/Al alloy composite.

5. CONCLUSIONS

This investigation had as its purpose to address several questions concerning the observed strength of discontinuous SiC/Al alloys, especially related to the mechanism proposed which is based on the changes in the microstructure of the matrix due to differences in thermal coefficient of expansion between the reinforcement and the matrix.

From a consideration of the data, several conclusions were obtained:

- The observed strength of the discontinuous SiC/Al composite can be accounted for in terms of a mechanism based on a change in the microstructure of the matrix.
- This change in the microstructure, i.e. an increased dislocation density and a reduced subgrain size as compared to 0 V% matrix alloy, is due to the difference in coefficient of expansion between the reinforcement (SiC) and the matrix (Al).
- The procedure of TEM foil preparation of the composites which involves electrical discharge machining, dimpling and ion milling does not introduce dislocations into the matrix.
- In order to obtain realistic values of the dislocation density of SiC/Al alloy composites, it is necessary to view thick foils, i.e. an operating voltage of 1 MV.

Acknowledgements—This research was supported by the Office of Naval Research under contract No. N00014-K-85-0007. The positive interactions with Dr S. Fishman of the Office of Naval Research are to be greatly acknowledged. The authors wish to acknowledge the assistance of Dr S. B. Wu in the performance of the tensile tests. The authors also wish to acknowledge the continued support of the Argonne National Laboratory HVEM facility, especially that of Dr E. Ryan.

REFERENCES

1. G. I. Taylor, *Proc. R. Soc.* **A145,** 362 (1934); *J. Inst. Metals* **62,** 307 (1938).
2. G. Boas, *Helv. Phys. Acta* **23,** 159 (1950).
3. H. J. McQueen and J. E. Hackett, *Metal. Trans.* **1,** 2997 (1970).
4. R. J. Arsenault, *Mater. Sci. Engng* **64,** 171 (1984).
5. M. Vogelsang, R. Fisher and R. J. Arsenault, *Metall. Trans.* **17A,** 379 (1986).
6. R. J. Arsenault and N. Shi, *Mater. Sci. Engng* **81,** 175 (1986).
7. H. Fujita, Y. Kawasali and E. Furubayashi, *Japan J. appl. Phys.* **6,** 214 (1967).
8. H. Fujita, T. Tabata, K. Yoshida, N. Summida and S. Katagiri, *Japan J. appl. Phys.* **11,** 1522 (1972).
9. H. Fujita and T. Tabata, *Japan J. appl. Phys.* **12,** 471 (1973).
10. M. Taya and R. J. Arsenault, *Scripta metall.* **21,** 349 (1987).
11. R. J. Arsenault, N. Shi, L. Wang and C. R. Feng, *Mater. Sci. Engng.* To be published.
12. N. Hansen, *Acta metall.* **25,** 863 (1977).
13. R. J. Arsenault, *J. comp. Tech. Res.* **10,** 140 (1988).
14. R. J. Arsenault and M. Taya, *Acta metall.* **35,** 651 (1987).

Materials Science and Engineering, A138 (1991) 227–235

The fracture mode in SiC–Al composites

S. B. Wu* and **R. J. Arsenault**

Metallurgical Materials Laboratory, Materials and Nuclear Engineering Department, University of Maryland, College Park, MD 20742-2115 (U.S.A.)

(Received August 3 1990)

Abstract

At least four distinct separation fracture modes (mechanisms) have been proposed for the fracture of SiC–Al composites: firstly, cracking of the SiC particles or whiskers in front of an advancing crack tip and the linking of these cracks; secondly, SiC particles or whiskers cracking and this crack initiating a fracture; thirdly, void nucleation and growth at the interfaces of SiC particles or whiskers and the matrix; fourthly, fracture of the matrix. There is evidence which supports all these mechanisms, and conversely there are data which indicate that these mechanisms have no relationship to the actual fracture process. It was found that the mode of fracture is through the matrix.

1. Introduction

Crack initiation and propagation, *i.e.* the separation mechanism, in SiC–Al composites have been investigated to some extent over the last few years. Essentially, there are three different questions that have been raised concerning the crack initiation and propagation. These are as follows.

(1) Does the fracture of the SiC particles contribute to the separation of the composite, *i.e.* are they an integral part of the fracture mode?

(2) Does void nucleation at the SiC whisker or particle and growth contribute to the fracture process?

(3) What is the significance of the crack-tip-opening displacement?

The fracture of SiC whiskers or particles can conceivably initiate fracture of the composite. If the particle or whisker were large enough, then a crack of critical length could form and if the dynamic K_{Ic} of the matrix were low enough, the crack would continue to propagate into the matrix, leading to failure of the composite [1]. If the fracture of SiC could initiate fracture, then the fracture of SiC should aid in the propagation of the crack. It has been shown that large intermetallic inclusions can act as a fracture initiation site in SiC–Al composites [2]. The most recent and probably the most thorough examination of crack propagation in particulate SiC–Al which supports the concept that cracking of SiC particles in front of the end crack is the significant mode of separation in SiC–Al composite was carried out by Shang and Ritchie [3]. There have also been some prior investigations, *e.g.* by You *et al.* [4], in which it was concluded that the fracture of SiC particles was important. In these investigations they examined what are defined as post-mortem samples. The crack has been propagated and opposite sides of the fracture surface are examined for chunks of SiC particles and, indeed, they did see matching pairs. Also, in an investigation by Flom and Arsenault [5] of the fracture SiC–Al composites, it is shown that there are large numbers of particles on the fracture surface, especially in composites containing larger (20 μm) SiC particles. However, if one examines these fracture surfaces by scanning Auger microscopy, then the number of places at which it is possible to obtain a clear and coherent SiC peak is relatively rare but it should be pointed out that in some cases a clear and distinct Auger spectrum of SiC can be obtained from SiC particles on the fracture surfaces, as shown in Fig. 1.

Also, in an experiment to measure the bond strength, a tensile sample of aluminum (purity, 99.99%) was fabricated which contained a SiC

*Deceased.

0921-5093/91/$3.50

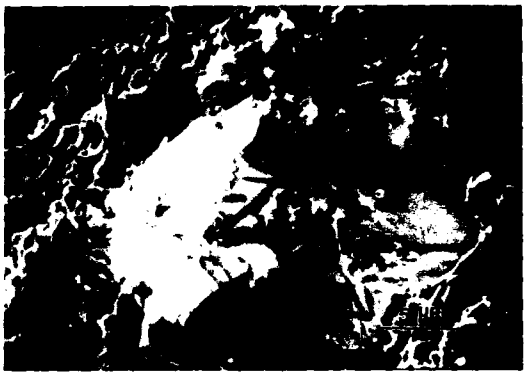

Fig. 1. A scanning electron micrograph of the fracture surface of a tension sample fractured in the scanning Auger microprobe (sample of 5 vol.% 5 μm SiC particulate in an aluminum alloy 2124 matrix).

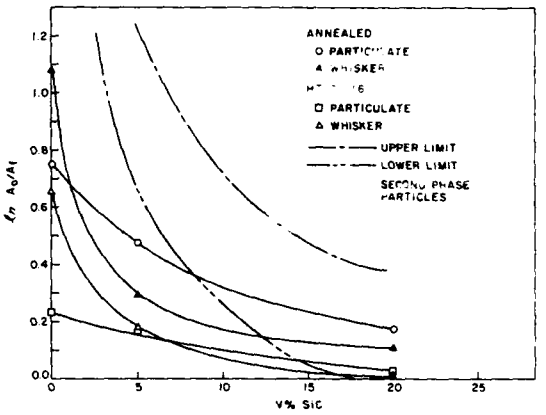

Fig. 2. A plot of the ductility *vs.* volume percentage of particulate in ductile matrix materials: – – –, – – – –, the upper and lower bounds respectively of a great deal of data which has been collected on particulate-in-ductile-matrix material: ———, particulate and whisker SiC in aluminum alloy 6061 in the annealed-and-heat-treated T6 condition.

sphere 3 mm in diameter in the center of the gauge section. The gauge section was 25 mm long and had a diameter of 6 mm. When the sample was tested, shortly after macro-yielding, the SiC sphere fractured perpendicular to the tensile axis with a small drop in load. The test was continued and the sample finally failed, but the sample did not fail by extension of the crack in the SiC into the aluminum matrix, even though there was a 25% reduction in the cross-sectional area as a result of the fractured SiC sphere. The sample failed at another place in the gauge length [6].

Another mechanism which has been proposed by numerous investigators is related to void nucleation at SiC particles and subsequent growth of these voids [7] as the separation mechanism. If we consider Fig. 2 which is a plot of the logarithm of the initial cross-sectional area of the sample divided by the area of fracture (as a measure of ductility) *vs.* volume fraction of particulate, then it can be seen that as the volume fraction increases, the ductility decreases. The area between the two broken curves in Fig. 2 contain a great deal of data which has been generated on numerous systems in which there is a hard particle (inclusion or precipitate) in a relatively ductile matrix. SiC particles in an aluminum matrix would satisfy this criterion, *i.e.* a hard particle in a ductile matrix and, as can be seen, for various types and conditions of particulate and whisker SiC–Al composites, the results show the same general trend, *i.e.*, as the volume fraction increases, the ductility decreases.

Further, if we can continue this discussion, the work by Gerberich [8] and several other investigators have shown that, if the particle size increases and the volume fraction is held constant, then K_{Ic} should increase. However, experimental observations by Flom and Arsenault [5] have shown that K_{Ic} in the small particle range, *i.e.* 20 μm and less in size, is not dependent upon the particle size or the interparticle spacing. For a much larger particle size (250 μm), then the mode of fracture changes drastically; there is a significant amount of fracture of the SiC particles.

Finally, a remaining topic is related to crack tip opening and displacement. The question is: what is the crack-tip-opening displacement, if any, and what does it mean? It has been argued by several individuals [3, 7] that crack-tip-opening displacement is a real value which has real meaning. If it is assumed that void nucleation at SiC particles and whiskers and subsequent growth of the void are the dominant mode of fracture, then the crack tip opening should be some large fraction of the whisker or particle spacing. However, work on post-mortem samples indicates that the crack-tip-opening displacement is vanishing small (Fig. 3), but a counter-argument could be made that, when examining post-mortem samples, the sample is not under load and therefore there may be significant closure of the crack.

Thus an investigation was undertaken to determine whether cracking of SiC particles did or did not occur during crack propagation of SiC–Al deposits. Also, as part of this investigation, the possible role of void nucleation and growth at SiC

Fig. 3. A scanning electron micrograph of a post-mortem compact tension sample showing the crack tip.

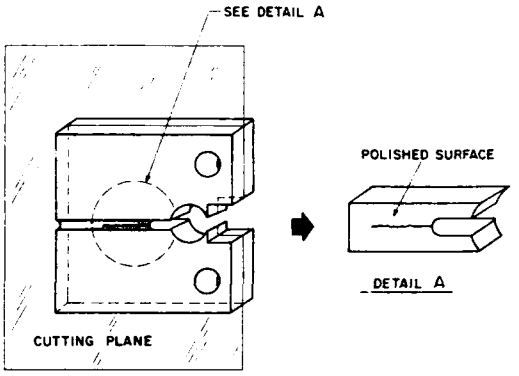

Fig. 4. A schematic view of a compact tension sample also showing the plane on which the sample was sliced in half for examination of the crack tip and subsequent deformation in the mini-tensile stage.

particles was considered. Finally, measurements of crack-tip-opening displacements were undertaken.

2. Materials and test procedures

Particulate SiC ranging in size from 2.4 to 20 μm was mixed with aluminum alloy 1100 powder (44 μm in diameter) and this mixture was then hot compacted and extruded into a bar which was 6 mm thick by 31 mm wide. The actual details of production have been described elsewhere [9]. The 250 μm SiC particulate composite was purchased from DWA Composites Specialities, Chatsworth, CA. Also, commercial aluminum alloy 6061 heat treated to the T6 condition was rolled to a 75% reduction in thickness.

The composite material and the aluminum alloy 6061 were machined into compact tensile samples as shown in Fig. 4 and tested in an Instron testing machine until a crack propagated into the matrix. After crack propagation, the sample was sliced in half by electrical discharge machining. Each half of the sliced compact tension sample was glued to an individual sample holder, so that the cut surface could be polished. In other words, the cutting plane (Fig. 4) was the surface which was polished. The samples were then placed on a Vibramat with a Buchler Mastermet™ polishing compound for approximately 3–4 days to obtain a polished surface. Attempts were made to use diamond paste and diamond sawing to reduce the time required for polishing the samples, but these proved to be unsatisfactory for they produced "chunks" of SiC in the matrix and also, in some cases, the diamond paste actually became embedded into the surface of the sample. After polishing, the samples were mounted in a mini-tensile stage. The method of loading the sample was by means of pins through the holes in the compact tension sample. The stage was constructed such that these pins move either toward or away from each other by the screw drive system. The displacement of the pins was calibrated, and one revolution of the main drive feed resulted in the pins being displaced by 11 μm. A drive system was constructed for this tensile stage with feedthroughs so that it could be mounted in the scanning electron microscope.

The crack tip region was then photographed, producing a map for the purpose of determining where and which of the SiC particles were fractured. Then the crack was opened at the pins in increments.

Transmission electron microscopy (TEM) foils were produced from annealed 2.4, 3.2, 8 and 20 μm SiC particulate–Al composite in the same manner as described elsewhere [10]. The foils were examined in the high voltage electron microscope at Argonne National Laboratory in the *in situ* tensile stage. A video tape was produced during the straining of the foil.

3. Results

Composite samples containing various sizes of SiC particulates were investigated; however, only a few of them will be considered.

The specific case to be discussed in detail is a composite containing 20 vol.% 8 μm SiC par-

Fig. 5. A scanning electron transmission micrograph of the crack tip in the unloaded condition of a 20 vol.% 8 μm particulate SiC–Al composite.

Fig. 6. A scanning electron micrograph of the propagation of a crack of a 20 vol.% 8 μm SiC particulate–Al alloy 1100 matrix composite.

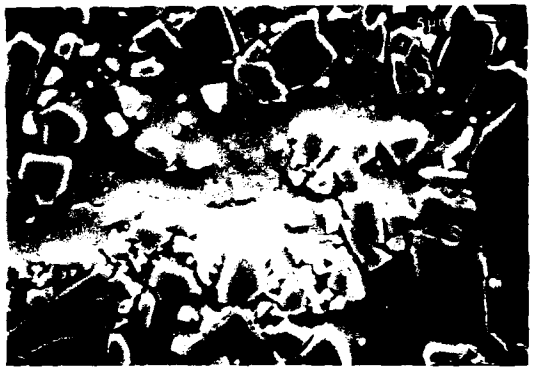

Fig. 7. A scanning electron micrograph of the propagation of a crack of a 20 vol.% 8 μm SiC particulate–Al alloy 1100 matrix composite.

Fig. 8. A scanning electron micrograph of the propagation of a crack of a 20 vol.% 8 μm SiC particulate–Al alloy 1100 matrix composite.

ticles. Figure 5 shows the crack tip in the pre-crack condition, *i.e.* in the unloaded condition. The sample was then loaded by displacing the pins by 22 μm and the crack propagated 250 μm; Fig. 6 is a micrograph of the crack tip area. (In all subsequent discussions of the crack tip, the load is applied.) The pins were displaced by another 6 μm. Figure 7 again shows the crack tip area. The crack has advanced about 5 μm. If Fig. 7 is considered in detail, it can be seen that the crack-tip-opening displacement is a small fraction of a micron, and the load is still being applied to the sample. The crack opening is extremely small; even at a distance of 5–10 μm behind the crack tip, the crack-opening displacement is less than 1 μm and probably less than 0.1 μm. With another 33 μm pin displacement, the crack has progressed, as shown in Fig. 8. In this particular case, the crack has stopped in front of a rather large particle. Continued loading of the sample results in no apparent change in the crack, except that the crack tip has opened further. When the pins are opened by an additional 22 μm, the crack displaces upward, as shown in Fig. 9 and the crack has made a significant advance of about 90 μm.

Upon further loading of the sample, as shown in Fig. 10, the crack tip has stopped somewhere in front of a particle which apparently is cracked in three different locations. The crack proceeds, as shown in Fig. 11, through one of pre-existing cracks in the cracked sample. Figures 12 and 13 are continuations of the crack. Figure 14 is of the same area as Figs. 12 and 13, except after further displacement of the loading pins. In this case, there is a distinct crack-tip-opening displacement. This is a typical result when the crack has propa-

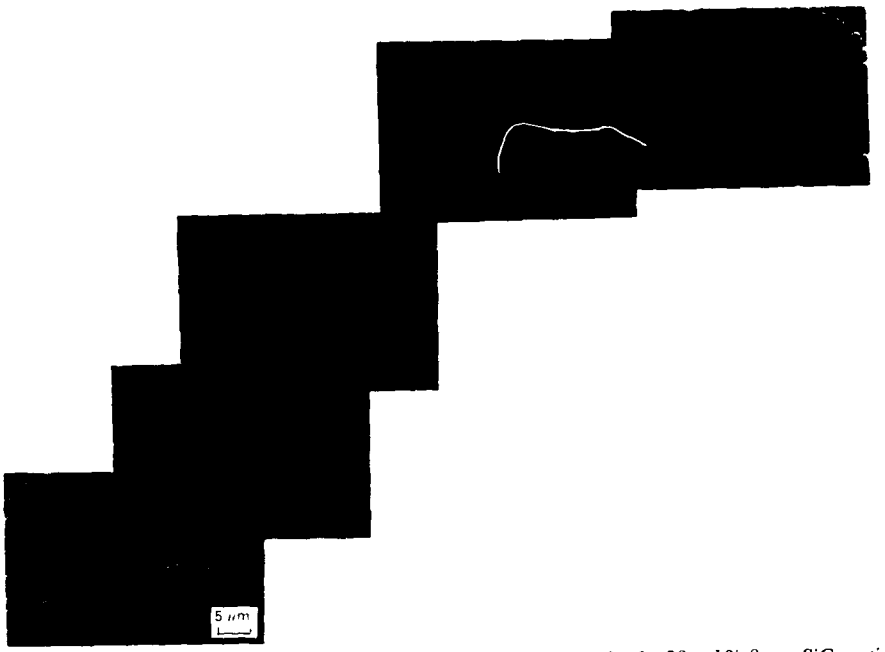

Fig. 9. A scanning electron micrograph of the propagation of a crack of a 20 vol.% 8 μm SiC particulate–Al alloy 1100 matrix composite.

Fig. 10. A scanning electron micrograph of the propagation of a crack of a 20 vol.% 8 μm SiC particulate–Al alloy 1100 matrix composite.

Fig. 11. A scanning electron micrograph of the propagation of a crack of a 20 vol.% 8 μm SiC particulate–Al alloy 1100 matrix composite.

gated a significant distance from its initial pre-cracked position in the bulk compact tension sample.

An observation which occurs infrequently was evident in the sample which contained 3.2 μm SiC particulate. In this particular case, there is evidence of cracking around the existing sub-grains within the material (Fig. 15). Also in this particular sample, there happens to be an inclusion, presumably of Al_2O_3, which cracks as shown in Fig. 16.

Another result which is not typical but seems to occur more frequently in the smaller particulate size (in this particular case, 2.4 μm SiC) is the greater appearance of the separation of the matrix about SiC particles in front of the crack tip. This is evident if we consider Figs. 17 and 18 of a 2.4 μm SiC composite. Also, Fig. 19 shows a good example where the crack has propagated a significant distance, and the crack-tip-opening displacement becomes much more pronounced. However, if you consider the crack-tip-opening

Fig. 12. A scanning electron micrograph of the propagation of a crack of a 20 vol.% 8 μm SiC particulate–Al alloy 1100 matrix composite.

Fig. 13. A scanning electron micrograph of the propagation of a crack of a 20 vol.% 8 μm SiC particulate–Al alloy 1100 matrix composite.

Fig. 14. A scanning electron micrograph of a propagation of a crack in a 20 vol.% 8 μm SiC particulate–Al alloy 1100 matrix composite.

displacement, these displacements are trivial compared with the crack-tip-opening displacements which occur in the cold-rolled aluminum alloy 6061.

Fig. 15. A scanning electron micrograph of a 20 vol.% 3.2 μm particulate SiC–Al alloy 1100 matrix.

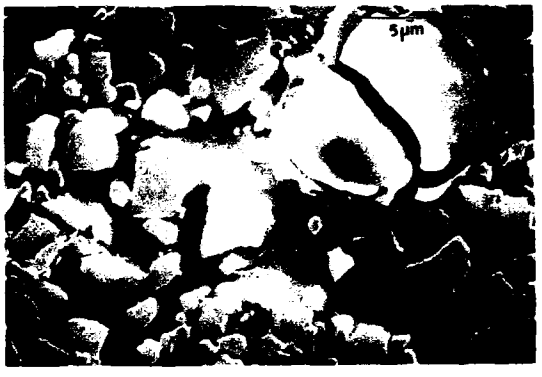

Fig. 16. A scanning electron micrograph of a 20 vol.% 3.2 μm particulate SiC–Al alloy 1100 matrix.

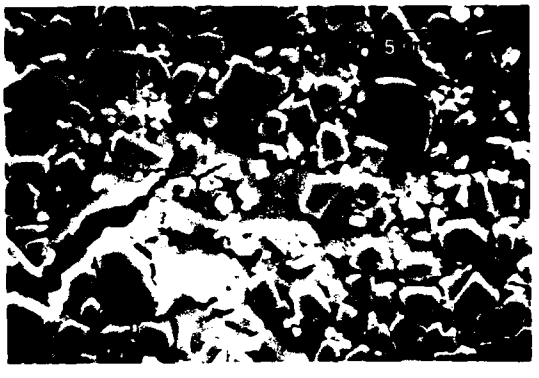

Fig. 17. A scanning electron micrograph of a 20 vol.% 2.4 μm particulate SiC composite.

Figure 20 is a micrograph of the unloaded crack in the pre-crack compact tension sample of cold-rolled aluminum alloy 6061. Figure 21 is after the sample has been loaded to a pin-opening displacement of 200 μm; the crack tip has not

Fig. 18. A scanning electron micrograph of a 20 vol.% 2.4 μm particulate SiC composite.

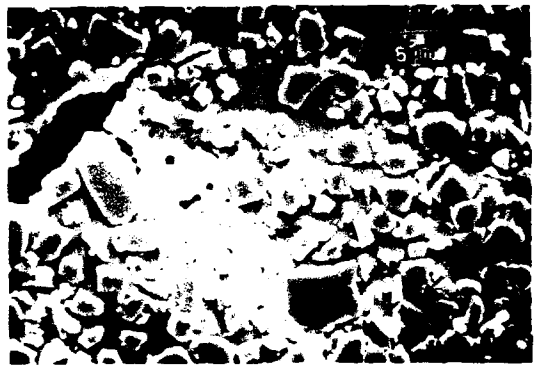

Fig. 19. A scanning electron micrograph of a 20 vol.% 2.4 μm particulate SiC composite.

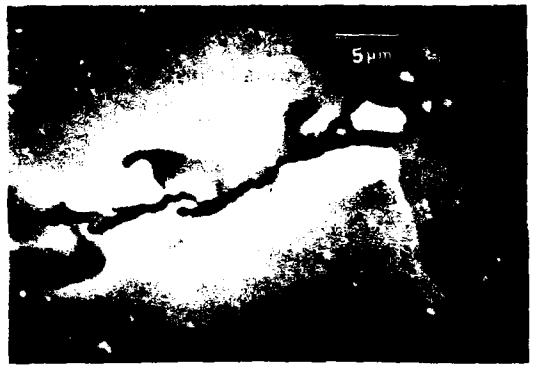

Fig. 20. The crack tip propagation in cold-rolled aluminum alloy 6061 heat treated to the T6 condition.

Fig. 21. The crack tip propagation in cold-rolled aluminum alloy 6061 heat treated to the T6 condition.

progressed at all, but now there is measurable (1–2 μm) crack-tip-opening displacement right at the crack tip and at about 2–10 μm behind the crack tip. This crack-tip-opening displacement is significantly different from that of the composite material which contains a small SiC particle size. Also, we observed measurable voids associated with the inclusions which occur in this particular material which is not evident in the composite material. There were no similar observations in the SiC–Al composites, *i.e.* there is no evidence of void formation at SiC particles in the front of the advancing crack.

The *in situ* TEM straining of the SiC–Al composites resulted in the formation of a crack at the edge of the hole and then crack propagation into the foil. In most cases, the propagation was very similar to that observed by scanning electron microscopy (SEM), *i.e.* the crack propagated around the SiC particles. However, in some cases an opening, *i.e.* a void, forms near an SiC particle leaving a distinct aluminum layer in the SiC particle. The location of the void was predicted by Wilner [11].

4. Discussion

From a consideration of the above experimental results it is obvious that there are differences from some of the previously generated data on the fracture characteristics of SiC–Al composites, but these differences can be readily accounted for. Also, a clearer explanation of some of the previous data is now possible.

The previous data from matching fracture surfaces and unloaded propagated cracks supported the concept that fracture of SiC particles in front of the advancing crack played a significant role in the fracture process and can be readily explained or accounted for. The above-mentioned previous data are based on the examination of post-mortem samples. The basic problem associated

with examining post-mortem samples is that it is impossible to know whether the SiC particle or whisker was broken owing to processing prior to the actual fracture test. In the present investigation there was no case where it could be shown that the advancing crack resulted in the fracture of SiC particles.

It was clearly observed that, as the crack advances, it has a distinct preference to proceed through existing cracked SiC particles. This would be entirely logical, since with the crack advancing through existing cracked SiC particles there is no need to create two new surfaces since they already exist. Therefore matching fracture surfaces would have a matching "fractured" SiC particle. Also, the observation by Flom and Arsenault [5] that the number of SiC particles along the fracture path is greater than a random line through the composites is simply a consequence that the crack would rather propagate through an existing cracked (fractured) SiC particle.

In terms of the sharpness of the crack tip in the composites, *i.e.* lack of crack tip blunting, this can be traced back to the lack of plastic deformation which does not occur in these composites. In order to have crack tip blunting, it is necessary to have in-plane plastic deformation. If plastic deformation in the crack tip region (which can occur) is very small, there will be no blunting. Considering a very simple case, if the crack was initially very sharp and then blunted to a crack-tip-opening displacement of 2 μm, as in the case of the cold-rolled aluminum alloy 6061, the effective plastic strain required would be 15–30% as obtained by McMeeking [12] in a finite element method investigation of crack tip blunting. It may be argued that the analysis of McMeeking is not valid since his analysis is for a stationary crack. The cracks in the SiC–Al composite propagate in a discontinuous manner. The major component of this effective plastic strain is a tensile strain perpendicular to the crack plane. However, Davidson [13] believes that the tensile strain is very small in SiC–Al composites. The tensile strain is small because of the elastic constraint of the high modulus (in comparison with aluminum) SiC particulate present in the composite, and the fact that the matrix within the composite has a very high dislocation density, *i.e.* equivalent to a highly cold-worked condition.

Even though the aluminum alloy 6061 was cold rolled 75%, it is still possible to have significant plastic strain occurring at the crack tip in the plane stress condition. Prior to slicing the sample in half, the crack propagates in a nearly plane strain condition. As a result of the greater plastic strain, there is significant crack tip opening (several orders of magnitude) in comparison with the SiC–Al composites.

The lack of void nucleation and growth at the SiC matrix interface is more than likely due to very high bond strength [14] between SiC and aluminum.

5. Conclusions

From a consideration of the experimental results obtained in this investigation, the following conclusions can be arrived at.

(1) The crack appears to go around intact SiC particles, leaving a distinct outer coating on the SiC particles which is in agreement with *in situ* TEM investigations of crack propagation in this particular material.

(2) The observance of cracking of the SiC particles in front of the crack tip due to the advance of the crack tip is a rare event. If there are pre-existing fractured SiC particles, the crack proceeds through the pre-cracked SiC particles.

(3) The existence of void nucleation and growth in front of the crack at the SiC particles was not observed in the SEM investigations; however, voids some distance from the SiC particles were observed in the TEM investigations.

(4) The crack-tip-opening displacement at the crack tip and 5–15 μm behind the crack tip as it initially propagates in the composites containing SiC particles of 2.4–20 μm size was extremely small, *i.e.* less than 0.1 μm.

(5) If a crack is propagated under the same conditions in cold-rolled aluminum alloy 6061-T6, then there is significant blunting at the crack tip, *i.e.* crack-tip-opening displacement becomes measurable (1–2 μm) and, in this particular case, void nucleation occurs at the oxide inclusion which occurs in this alloy.

Acknowledgments

The authors wish to acknowledge the continued support and encouragement of Dr. S. G. Fishman of the Office of Naval Research. This research was supported by the Office of Naval Research under contract No. N00014-85-K-0007.

References

1 G. T. Hahn, *Metall. Trans. A*, *15* (1984) 947.
2 Y. Flom and R. J. Arsenault, *J. Met.*, *38* (1986) 31.
3 J. K. Shang and R. O. Ritchie, *Metall. Trans. A*, *20* (1989) 897.
4 C. P. You, A. W. Thompson and I. M. Bernstein, *Scr. Metall.*, *21* (1987) 181.
5 Y. Flom and R. J. Arsenault, *Acta Metall.*, *37* (1989) 2413.
6 Y. Flom, *Master's Thesis*, University of Maryland, 1984.
7 C. R. Crowe, R. A. Gray and D. F. Hasson, in W. Harrigan, J. Strife and A. K. Dhingra (eds.), *Proc. 5th Int. Conf. on Composite Materials*, Metallurgical Society of AIME, Warrendale, PA, 1985, p. 843.
8 W. W. Gerberich, in J. M. Wells and J. B. Landis (eds.), *Proc. 113th AIME Conf.*, AIME, New York, 1985, p. 49.
9 Y. Flom, *Ph.D. Thesis*, University of Maryland, 1987.
10 M. Vogelsang, R. J. Arsenault and R. M. Fisher, *Metall. Trans. A*, *17* (1986) 379.
11 B. Wilner, *J. Mech. Phys. Solids*, *36* (2) (1988) 141.
12 R. M. McMeeking, *J. Mech. Phys. Solids*, *25* (1977) 357.
13 D. L. Davidson, Annual report to Office of Naval Research, *Rep. 06-8602/5*, January 1989; personal communication, March 1990.
14 Y. Flom and R. J. Arsenault, *Mater. Sci. Eng.*, *77* (1986) 191.

Analytical Evaluation of the Thermal Residual Stresses in SiC/Al Composites*

Ning SHI and Richard Joseph ARSENAULT**

An analytical investigation of the difference in the constitutive behavior of SiC-Al composites under uniaxial compressive and tensile loading was carried out and the associated changes of the residual stresses were studied. It is suggested that the observed asymmetric response of the constitutive behavior is primarily due to the existence of residual stresses in the composite, and the residual stresses are initially introduced due to the differences in the coefficients of thermal expansion (ΔCTE), and subsequently changed after the external load is applied. A two-dimensional finite element analysis of a hexagonal array of SiC whiskers in an Al matrix was performed, the result of which testifies to the appropriateness of the proposed explanation. It is concluded that the 2-D finite element analysis is an economical way of adequately reproducing the most prominent features of the material's constitutive behavior. Based upon the theory of mechanics of composite material, simplified analytical models were developed which can be used to investigate the influences of the whisker-matrix interface shear load transfer and the volume mismatch on the residual stresses. It is concluded that the mechanism of load transfer in terms of normal stress at the whisker tip, which is governed by the volume (bulk) mismatch between the matrix and the whisker, is predominantly responsible for altering the specific pattern of the residual stresses under the applied load. In contrast, the effect of shear load transfer at the longitudinal whisker-matrix interface is only restricted to a very small region in the vicinity of the whisker and does not significantly influence the overall proposed asymmetric constitutive behavior.

Key Words: Metallurgical Materials Laboratory, Department of Materials and Nuclear Engineering

I. Introduction

A previous investigation of the deformation behavior of short whisker reinforced SiC-Al composites[1] has indicated that the constitutive behavior of these composites is distinctly different under uniaxial compressive deformation as compared to tensile deformation. It was generally found that the compressive yield strength of these composites was larger than that of the tensile yield strength, while the Young's modulus for compression was smaller than that in tension. If monolithic aluminum is initially deformed plastically in tension, then reverse deformed in compression, a difference in stress is required to continue plastic deformation. Usually, this stress is less upon reverse loading. This reduction in stress (or the strain necessary to reach the previous level of flow stress) is defined as the Bauschinger Effect. In the case of monolithic aluminum, the direction of initial deformation (i.e., tension or compression) does not have any effect on the Bauschinger Effect. The SiC-Al composites exhibit a remarkable characteristic, i.e. the flow stress drop (or alternatively, the Bauschinger strain) is larger when the composite is first pre-compressed plastically and subsequently deformed in tension than when the composite is first deformed in tension and then compressed[1].

It is the opinion of the authors that the aforementioned differences in the constitutive behavior under tensile and compressive loading as well as the asymmetric Bauschinger phenomenon are primarily due to the influence of the residual stresses. It has been shown that thermal residual stresses affect not only the elasto-plastic deformation behavior of the composites[1], but also the fracture behavior[2]. Therefore, it becomes increasingly important to investigate the deformation process in terms of residual stresses.

The material to be simulated in this investigation consists of an annealed 6061 aluminum alloy matrix reinforced by silicon carbide whiskers. The primary goal of this paper is to analytically investigate the generation, arrangement and magnitude of the residual stresses due to the difference in coefficients of thermal expansion (ΔCTE) during cooling process; then, to study the changes in the residual stress as a result of external deformation either in tension or compression; and also, to investigate the differences in the constitutive behavior under different external loading, i.e., deformation conditions. In the experimental procedure described elsewhere[1][3], the materials are annealed at 773K and then tested either in

* Received 2nd October, 1990

** University of Maryland at College Park, Maryland 20742-2115, U. S. A.

uniaxial tension or compression at room temperature. Our commitment in this investigation is to adhere to this physical process and, thereby, to simulate the constitutive behaviors of the composites and to monitor the change of the residual stresses. These residual stresses were induced by the thermal cooling process due to the mismatch of the coefficients of thermal expansion between the matrix and the reinforcement, and subsequently, they were altered by the external load.

While several investigators have concentrated their work on the thermal residual stresses[4]~[8], others[9]~[18] have worked on the elasto-plastic behaviors of the short whisker reinforced composites with emphasis on the stress-strain relationships, i. e., constitutive behaviors, of the composites. Their research includes numerical treatments which utilize the finite element procedures[9]~[13]. Some of them paid special attention to the microstructural change in the matrix[10],[13] while others were based on various theoretical bases with different assumptions[14]~[18].

Recently, Arsenault and Taya[19] and Withers et al.[20] employed the Eshelby method[21],[22] to explain the yielding behavior of the short whisker reinforced metal matrix composites (MMC) under the influence of the thermal residual stresses. They found that the residual stresses are totally responsible for the difference in the yield strength of the whisker reinforced MMC between tension and compression. However, despite the effort by the previous investigators[19],[20], the role of residual stresses played on the constitutive behavior of the composites or the effect of external loading on the formation of residual stresses has never been systematically investigated. Nevertheless, these experimental or theoretical results[19],[20] have provided us with a clear indication that the residual stresses may be a dominating factor which accounts for the differences of constitutive behavior as a funtion of loading direction.

It is, therefore, of interest to investigate the constitutive behavior of the composites under the influence of the residual stresses due to the ΔCTE, and to evaluate the changes that occur in the magnitude of residual stresses when the composite is subjected to either a uniaxial tensile or compressive deformation. The analytical investigation in this study is carried out by two distinct methods : a finite element analysis, and a phenomenological modelling scheme involving two models. The main objective of the finite element analysis is to monitor the stress-strain relationship and the changes that occur in the value of the residual stresses due to the external deformation. The purpose of the phenomenological models, on the other hand, is to obtain some physical insight into the various factors which control the processes of residual stress generation and alteration and the role these play in influencing the composites' constitutive behavior.

II. The Finite Element Model

In order to determine the material's response under the influence of residual stresses, a simplified two-dimensional finite element analysis was carried out using the ADINA code. Particular interest was paid to determining the macroscopic stress-strain behavior of the composites and to perform a microscopic analysis of the subsequent changes that occur in the values of the internal residual stresses after the external load was removed.

In a recent study, Takao and Taya[23] have shown that the use of the volume-average aspect ratio will provide an accurate account for overall composite properties, and the employment of the perfect alignment will give rise to satisfactory results, although not as accurate as the volume-average aspect ratio representation. Therefore, in the analyses, the value of the volume fraction of the whiskers as well as the whisker aspect ratio were held constant ($V_w = 20\%$ and $l/d = 4$). The value of $l/d = 4$ is typical of the average values observed experimentally[24],[25]. Furthermore, it was assumed that the composites consists of a hexagonal arrangement of arrays of parallelepiped SiC whiskers embedded in a 6061 aluminum alloy matrix (Fig. 1). Previous investigations[9],[11] and our current analysis have indicated that within a particular region, a small variation in the values of interparticle spacing does not significantly affect the material behavior (e. g., for the influence on yield stress, see Fig. 2). The value of V/H in Fig. 1, therefore, was not selected as a critical parameter in the analysis and was kept as a constant (0.29) throughout the analyses.

Figure 3 indicates the exact details of the finite element mesh where six to eight node isoparameter elements were employed. Only a quadrant of the composite material which contains the SiC whisker was selected to represent the whole infinite array of fibers in the matrix, and a multi-constraint boundary condition was employed accordingly in the analysis which corresponds to the bounday condition indicated as the following :

$$\int_{l_k} \sigma_{ij} n_j dl = 0$$

where σ_{ij} is the stresses at the boundary, n_j is the unit outward normal and l_k represents four different sides of the boundary of the unit cell.

Since the constitutive behavior of the SiC whisker/Al matrix composites has been extensively investigated experimentally[1],[25],[26], it will be appropriate

to compare our FEM results with those obtained from experimentation. Because the differences in constitutive behavior of the composites are believed to be due mainly to the presence of the residual stresses, by considering the initial thermal residual stresses which are generated during the cooling process, the FEM model should reproduce such differences. On the other hand, if such differences are predicted, then the residual stresses which are responsible for producing such differences should be reasonably well predicted.

The FEM simulation is set up in such a way that the matrix and reinforcement material is assumed to be stress-free at 773K. Then a temperature change of −480K was applied uniformly on the FEM mesh, which corresponds to the cooling process from annealing temperature to the room temperature at a very slow rate. This is actually true for the furnace cooling condition. During the entire cooling process, it is assumed that the SiC whisker reinforcement behaves perfectly elastic in response to the incompatibility between the Al matrix and the SiC whisker reimforcement due to ΔCTE. On the other hand, the Al matrix becomes softer and softer as the temperature goes up. The detailed material constants are listed in Table 1.

After the composites were cooled to room temperature, the FEM mesh was externally loaded incrementally. Figure 4 shows the uniaxial stress-strain curves produced by the FEM analysis where the global stress and strain are defined as:

$$\varepsilon = \frac{u_i}{V+l}\ ;\ \sigma = \langle \sigma_i \rangle$$

where u_i and $\langle \sigma_i \rangle$ (in this case, i is equal to 3) are the average displacement and the normal stress along the boundary whose normal is parallel to the uniaxial

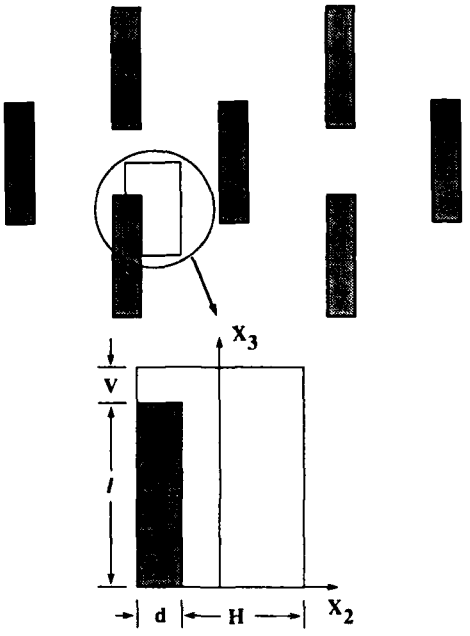

Fig. 1 The whiskers are so arranged in a periodic hexagonal packed infinite array that by considering symmetry, only a quadrant of the particle is needed, as indicated in the figure.

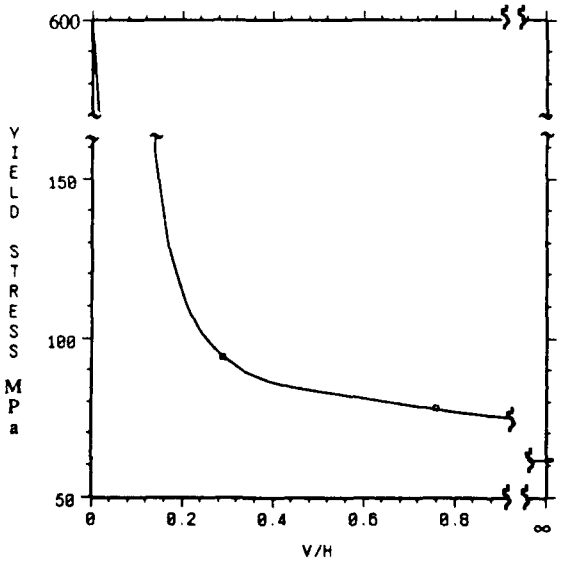

Fig. 2 FEM results indicate that the yield stress of the composites is not sensitive to the ratio of V/H defined in Fig. 1.

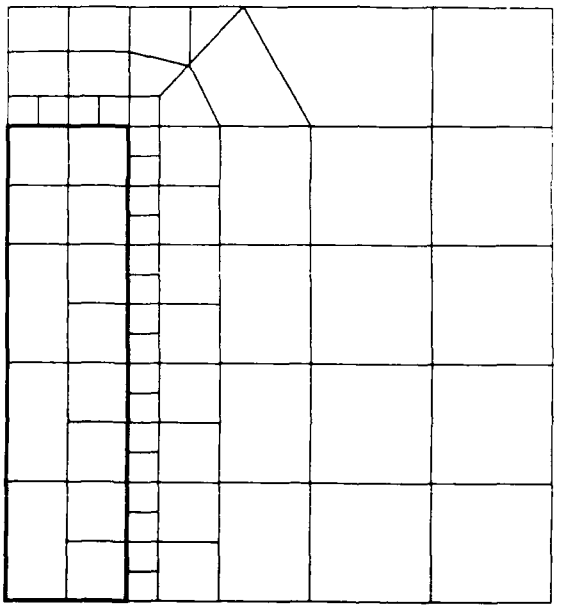

Fig. 3 FEM mesh where six to eight-node elements were employed.

loading direction. $\langle\sigma_i\rangle$ can also be defined as the applied load intensity, (q), and V and l are defined in Fig. 1.

From these curves, we can see that the FEM results are in reasonable agreement with the experimental data[1]. For example, the apparent Young's modulus for tension is larger than that in compression and the compression yield strength is larger than that of tensile yield strength, which are both apparent in the experimental curves[1].

A Bauschinger test can also be carried out by FEM. There are many indicators for the Bauschinger Effect; one of them is the Bauschinger strain (ε_b), which is conveniently defined as the strain difference required for reverse flow stress to reach the previous level of forward flow stress. An easy visualization of the Bauschinger strain can be made by replotting the complete stress strain cycle so that the reverse loading portion of the stress-strain curve was plotted symmetrically against the unloaded state form the forward straining cycle on the stress strain curve, so that the complete stress strain curve (forward and reverse loading) would appear on the same first quadrant of the cartisian coordinate system, as can be seen in Fig. 5. From the FEM results, it can be easily revealed that the direction of initial loading has an effect on the magnitude of the Bauschinger strain (ε_b). If initially tested in tension and then reverse loaded into compression, the Bauschinger strain is smaller compared to the case where initial loading is in compression followed by tension [Fig. 5]. If we just consider the reverse loading curves, then the σ vs. ε for the reverse loading curve in the case of tension first has a higher yield stress than that of tension reverse loading of compression first [Fig. 5].This has been observed experimentally[1].

In the study of the internal stresses in composite materials, it is a common practice to employ the concept of volume average both experimentally[29],[30] and theoretically[19],[20],[31]. Consequently, the authors would like to adopt the same methodology in dealing with this issue. Because the longitudinal thermal residual stress is much larger than the transverse residual stress[19], it is believed that the observed differences in constitutive behavior are mainly due to the longitudinal residual stress. The longitudinal thermal residual stress in the composites was therefore found by first evaluating the residual stress in a typical finite element mesh and then averaging these values over the whole specimen. The overall average residual stress in the matrix was calculated through a simple averaging scheme given by the following equation:

$$\langle\sigma_{ij}\rangle=\frac{\sum_k(\sigma_{ij})_k A_k}{\sum_k A_k} \qquad (i=j=3) \qquad (3)$$

where $(\sigma_{ij})_k$ is the stress in element k, and A_k is the area of that element.

Using this simplified averaging scheme, it was found that upon application of 1% plastic strain, if the applied loading is tensile, the average matrix residual stress changes from its initial tensile value of 47.5 MPa to the compressive value of -10.8 MPa, while if the applied loading is compressive, the average matrix longitudinal (tensile) residual stress drops from its as-annealed value of 47.5 MPa to 20.1 MPa at $\sim 0.3\%$ strain and then increases back up to 29.3 MPa when it reaches 1% plastic strain. The overall change in resiual stress as a function of applied strain is shown Fig. 6. It is clear that the primary effect of compressive loading is merely to intensify the residual stress in the matrix after an initial reduction while tensile deformation produces an overall reduction in

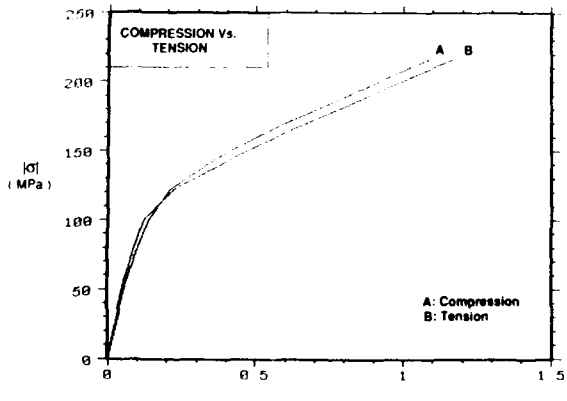

Fig. 4 Stress-strain curves predicted by FEM where the apparent Young's modulus of the composite is higher when it is in tension load, whereas the yield stress is greater when the sample is under compresion load.

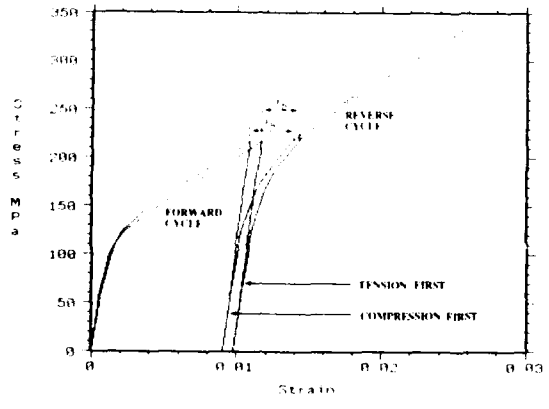

Fig. 5 FEM prediction of Bauschinger strain (ε_b) where ε_b is larger if the sample is under the compression-first loading scheme.

the tensile residual stress, and eventually such a reduction will lead to changes in the residual stress from tensile to compressive. That is, the change in residual stress does not occur monotonically with increasing deformation. To recap, in the case of compression deformation, there is an initial decrease in the tensile residual stress due to deformation, at a total strain of $\sim 0.3\%$ which is within close proximity of 0.2% strain of yielding and the tensile residual stress reaches a minimum at this point. Upon further deformation, there is an increase in the tensile residual stress. In the case of tensile deformation, the tensile residual stress initially decreases at a more rapid rate to $\sim 0.3\%$ total strain, and then the rate of decrease slows down. At a total strain of $\sim 0.7\%$, the residual stress becomes compressive. Even though the total average longitudinal thermal residual stress is in tension, previous FEM results[13] have indicated that in whisker-reinforced composite materials, the residual stress distribution is such that near the tip of the whisker, the matrix is under compression while the rest of the matrix is in tension, thus giving rise to an overall tensile average residual stress in the matrix. Interestingly enough, our finite element analysis indicated that under applied tensile load, the compression and tension zones exchanged their signs within a reasonable range of strain (Fig. 7), while compressive loading led to a residual stress increase in both regions. Another persuasive fact to be noted is that while the global average residual stress exhibited a non-monotonic behavior, the residual stress near the whisker matrix interface never showed an initial drop after loading as it did in the case of global average residual stress. The response of the residual stress to the external load near the interface was such that the longitudinal residual stress increased upon an initial compressive plastic prestrain and decreased with an initial tensile plastic prestrain, as can be seen in Fig. 8.

Although the simplified averaging scheme discussed above is easy to use, it works best only with a uniform field. It is evident that this scheme does not reflect the fact that the deformation upon loading is inhomogeneous in the matrix, and because of this deformation inhomogeneity, the influence of the residual stress on the yield point of that particular part of matrix will vary depending on the local deformation rate or deformation gradient. The higher the deformation rate, the more important the role the residual stress will play. Therefore, to best evaluate the effect of the thermal residual stress on the subsequent loading, the authors believe that application of a weighted-averaging scheme is more appropriate and will lead to more accurate accounting of the actual physical process. To do so, the local loading rate ($\partial\sigma_{ij}/\partial q$), as a measure of deformation gradient, can be directly incorporated into the average stress formula.

An averaging formula of the type

$$\bar{\sigma}_{ij}=\frac{\Sigma_k\left[\frac{\Delta\sigma_{ij}}{\Delta q}\right]_k^2(\sigma_{ij})_k A_k}{\Sigma_k\left[\frac{\Delta\sigma_{ij}}{\Delta q}\right]_k^2 A_k} \tag{4·a}$$

where

$$(\Delta\sigma_{ij})_k=(\sigma_{ij})_k|_{t+\Delta t}-(\sigma_{ij})_k|_t \tag{4·b}$$

and

$$\Delta q=q|_{t+\Delta t}-q|_t \tag{4·c}$$

was then used, where q is the applied load intensity and $\bar{\sigma}_{ij}$ now denotes the new average residual stress in the matrix.

From Eq (4), it can be easily seen that as compared with Eq. (3), the effect of residual stresses at each point is weighted literally by the magnitude of the stress rate. Since the stress rate, which is defined as a stress increase at a local point per unit external load increment, is a measure of the local stress concentration, Eq. (4) gives a scalar value which indicates an overall impact of residual stress on the subsequent loading. In other words, Eq. (4) puts

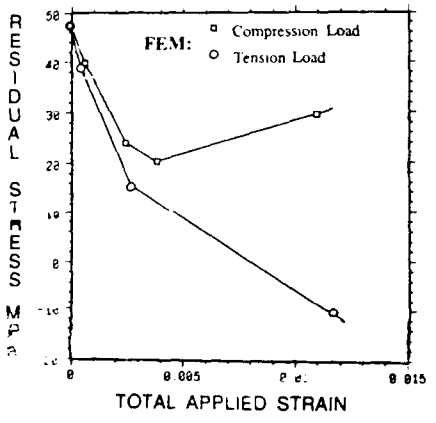

Fig. 6 As a result of tension loading, the arrangement of residual stress alters so that, at the whisker tip, the sign of the residual stress changes from tension to compression.

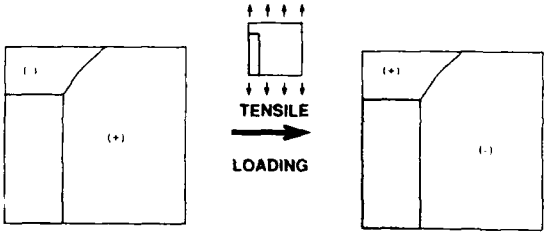

Fig. 7 The residual stress versus total strain of a whisker composite.

more emphasis on the residual stress value at locations where it will have higher stress concentration during subsequent loading, and at the same time, plays down the importance of those with lower stress concentration. Besides what is illustrated above, another significance of Eq. (4) is that by comparing it with Eq. (3), an indicator of the degree of deformation inhomogeneity can be worked out. Such an indicator is important because in analytical elasto-plastic analyses involving the Eshelby-type mean field theory, one of the key assumptions is that the deformation in the matrix does not deviate greatly from the state of homogeneous deformation. One easy way to obtain such an indicator is to take the ratio of the outcome of the simple average [Eq. (3)] over the weighted average [Eq. (4)] since in a homogeneous deformation process, Eq. (3) is equivalent to Eq. (4).

To apply the above illustration to the current analysis, it was found that upon an initial load, the ratio between the two averages is:

$$\frac{\langle \sigma_{ij} \rangle}{\bar{\sigma}_{ij}} = 1.55 \qquad (i=j=3) \tag{5}$$

The factor 1.55 is an indicative of the degree of deformation heterogeneity of the composite material, which undoubtedly contributes to the change in residual stress upon unloading. Equation (5) indicates that the simplified average thermal residual stress is greater than that produced from the weighted scheme, which means that the weighting factor is larger in the compressive residual stress region where the residual stress has a negative value. That simply means that the compression zone at the tip of the whiskers is responding faster to the external loading than the rest of the matrix. In order to better understand the heterogeneous deformation field in the matrix due to the existence of the whiskers, a stress rate $(\partial\sigma/\partial q)$ diagram was constructed for the composite in different parts of the matrix when the composite is initially loaded in tension, as shown in Fig. 9. In particular, three regions within the matrix were of interest. The analysis indicated that the average stress rate within the regions A, B and C were, respectively, 6×10^{-2} (MPa/MPa), 9×10^{-2}(MPa/MPa) and 13×10^{-2} (MPa/MPa). These results support the notion that the compressive zone at the tip of the whisker responds faster to external loading than any other region in the matrix. On the other hand, in the vicinity of the longitudinal whisker-matrix interface, the response of the internal stress to applied loading is the slowest. Finally, in region B, where some interaction with the whisker tip is expected, the response to applied loading falls within a somewhat intermediate state. The finding that there is a stress concentration at the whiskers tips is consistent with what was observed experimentally. N. Sato et al.[32] have reported extensive damages at short fiber tips due to excess plastic deformation.

In consideration of the deformation process in the

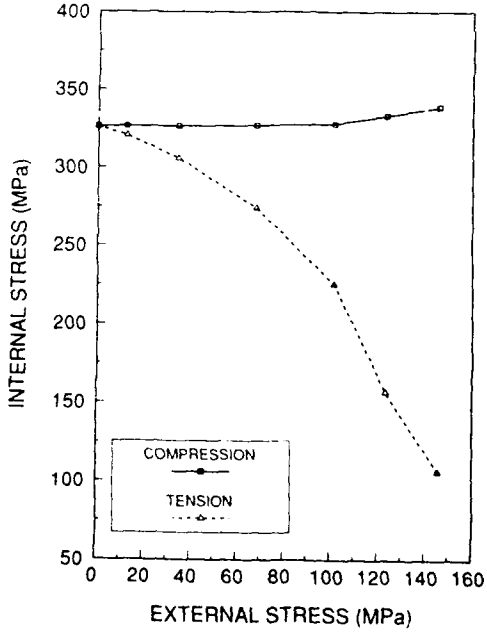

Fig. 8 Average residual stress near the longitudinal matrix whisker interface as a function of applied stress. The residual stress is taken from an area of $0.3l\times0.2d$ around the transverse center line of the whisker ear the interface.

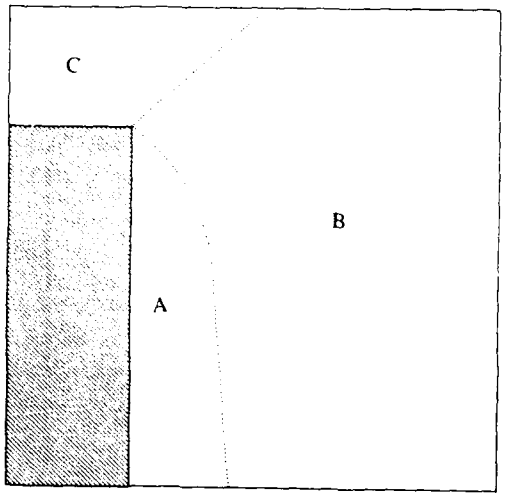

Fig. 9 FEM results indicated that the residual stress field can be characterized into three regions in terms of stress rate, where at the whisker tip, the stress rate is highest.

matrix, it is believed that the differences in micro-strain rate in different parts of the matrix are solely due to the presence of the whiskers. That is, near the longitudinal whisker-matrix interface, deformation will be restricted due to the high stiffness of the SiC whisker, and at the same time, the matrix material at the whisker tip will have to deform more to accommodate the global strain. The microstress rate in the initial compression zone at the end of the whisker is always larger than the microstress rate in the initial tension zone, irrespective of the global strain. It is also important to note that because of the differences in the micro-strain rates in different regions of the matrix and because the changes made by plastic deformation cannot be recovered, the compatibility condition between different regions will be permanently altered as a result of external loading. Therefore, the corresponding residual stress will change after unloading.

The finite element analysis presented in this paper has been performed with the sole intention of obtaining a better understanding of the effect of the residual stresses on the constitutive behavior of discontinuously reinforced metal matrix composites. It is evident that the most prominent characteristics of the composite constitutive behavior have been adequately predicted using such an approach. Although the 2-D FEM model provides a good economical tool for understanding how the system operates, it was not the intention of the authors in the present investigation to quantitatively compare the analytical results with those obtained experimentally. It is evident that the plane-strain representation of an otherwise much more complex three-dimensional array of whiskers in a matrix is an over-simplification.

III. Phenomenological Modelling

The results of the finite element analysis discussed in the previous section indicate that the change of the magnitude of the residual stress induced by ΔCTE and its subsequent change under the influence of mechanical deformation are primarily governed by the plastic strain gradients in the matrix. It is our belief that the existence of the initial compression zone is a direct consequence of volume mismatch between the whisker and the matrix, which occurs as a result of ΔCTE in the composite. On the other hand, the fact that the average matrix residual stress is in tension can also be obtained through interface shear load transfer. It is, therefore, clear that the processes of residual stress generation and residual stress change are basically controlled by two factors: the nature of the interfacial shear load transfer between the SiC whiskers and the Al matrix and the volume mismatch between the two constituents. The mismatch of the volume is introduced by either the CTE mismatch when under thermal loading or the differences in Young's modulus when under external loading.

In order to maintain overall compatibility, the two factors must work together. The volume difference is matched through interfacial normal stress and the interfacial compatibility is satisfied by means of interfacial shear stress. In order to comprehend the separate roles of "interface effect" and "volume mismatch" on the residual stress response after the mechanical loading, two distinct analytical models were developed. The first model, subsequently referred to as the "interface model", is shown in Fig. 10, which assumes that the material consists of a discontinuous filament embedded in the matrix. It is essentially the same as the shear lag model with an additional consideration of thermal stress and average plastic deformation. It is also assumed that there is full elastic continuity across the whisker-matrix interface. The whiskers, therefore, remain fully bonded to the matrix, causing complete load transfer between the two constituents. The primary purpose of this type of modelling is to understand the effect of load transfer at the interface on the residual stress due to the applied loading.

In the second model, it is assumed that a discontinuous whisker is embedded in the matrix. Interfacial sliding is allowed across the whisker-matrix interface along the direction of the whisker axis, but there is full elastic continuity at the tip of the whisker between the whisker and the surrounding matrix provided by normal interfacial stress. This model, which is referred to as the "volume mismatch model", is shown in Fig. 11. The main purpose of this model is to explain how the volume mismatch affects the residual stress arrangement as a result of temperature change and external loading.

As in the case of FEM analysis, a bilinear stress-strain materials model is assumed for the matrix and a perfectly elastic model is assumd for the whisker in both of the analyses. The two analytical models are discussed in more detail below.

The Shear Lag Model

The simplest and yet most effective approach to account for the mechanism of shear load transfer at the matrix-reinforcement interface is the "shear lag" theory introduced by Cox[33]. Ever since the advent of this theory, it has been widely used due to its simplicity. Some investigators[34],[35] have claimed it to be quite accurate in predicting mechanical properties of the composites; others[25],[36] have found it less attractive. In this section, a modified "shear lag" method is

employed to try to account for the generation of the residual stresses.

In developing a modified shear lag theory, as in Ref.[33], the change of the normal fiber stress can be equated to the interface shear stress through an equilibrium condition. Furthermore, because the matrix material is assumed to follow the bilinear stress strain model, an assumption was made that the amount of unrecoverable interfacial shear strain (plastic) will induce a proportional amount of the interfacial shear stress in the matrix because of a constant work hardening rate. It is also assumed that the overall constitutive response of the matrix remains elastic until the average matrix stress state satisfies the Tresca yielding criterion.

When the composite is cooled down from the annealing temperature, longitudinal thermal residual stresses are developed in the matrix and the whisker. These will be denoted as $\langle\sigma_m^r\rangle$ and $\langle\sigma_w^r\rangle$, respectively. Using a modified shear lag model which incorporates temperature effect and plasticity, appropriate expressions may be readily derived for $\langle\sigma_m^r\rangle$ and $\langle\sigma_w^r\rangle$. The governing equation for the modified shear lag model is (further details are given elsewhere[37]) :

$$\frac{d\sigma_w}{dz}=h(|\Delta\alpha|\,|\Delta T|z+\Delta w-\Delta w_v)-\frac{4D}{d^2}\tau_p=\frac{-4\tau_0}{d} \tag{6}$$

where $\Delta\alpha$ is ΔCTE, ΔT is the magnitude of temperature change, $\Delta w=u-v$ where u and v are the displacements along whisker axes at and away from the interface in the matrix, respectively, Δw_v represents Δw when interface shear stress τ_0 approaches yielding (τ_p), σ_w is the whisker stress and h is a constant to be determined. As shown in Fig. 10, D and d are the diameters of the unit cell and the whisker, respectively. If the temperature differential ($|\Delta T|$) is such that the strains in both the matrix and the whisker remain elastic, then Δw_v and τ_p may be taken away from Eq. (6), and Eq. (6) will be reduced to the form given by Cox[33] with a new thermal mismatch term ($h|\Delta\alpha|\,|\Delta T|$). For 20% SiC/Al composite, it is likely that the matrix will be plastically deformed as a result of the cooling process. Following the procedure summarized by Kelly[38], the general form of the solution is obtained as follows[37] :

$$\begin{cases}\langle\sigma_m^r\rangle=\\ \quad E_w\left\{1-\dfrac{\tanh(\beta l/2)}{(\beta l/2)}\right\}\left[\sigma_{ym}\left[\dfrac{1}{E_m}-\dfrac{1}{E_{mp}}\right]\right]\\ \quad\Big/\left\{1+\dfrac{V_w}{1-V_w}\dfrac{E_w}{E_{mp}}\left\{1-\dfrac{\tanh(\beta l/2)}{(\beta l/2)}\right\}\right\} & (7\cdot a)\\ \langle\sigma_w^r\rangle V_w+\langle\sigma_m^r\rangle(1-V_w)=0 & (7\cdot b)\\ \beta=\sqrt{\dfrac{h}{E_w}} & (7\cdot c)\end{cases}$$

where V_w is the volume fraction of the whiskers, E_m and E_w represent the Young's moduli of the matrix and whisker, respectively, E_{mp} is the work hardening rate of the matrix, σ_{ym} is the matrix yield stress, l is the total length of the whisker and h and β can be determined as follows :

$$h=\frac{8G_{mp}}{d^2\ln(D/d)} \tag{8\cdot a}$$

$$\beta=\frac{2\sqrt{2}}{d}\sqrt{\frac{G_{mp}/E_w}{\ln(D/d)}} \tag{8\cdot b}$$

where G_{mp} is the tangential shear modulus of the matrix.

When a uniaxial loading (σ_{ca}) corresponding to the total strain (ε_{tot}) is applied along the whisker's direction in either tension or compression, and the composite is then unloaded, it may be shown that the matrix residual stress ($\langle\sigma_m^{ru}\rangle$) as a result of applied loading now becomes :

$$\begin{cases}\langle\sigma_m^{ru}\rangle=\langle\sigma_m^r\rangle-\dfrac{V_wE_w(E_m-E_{mp})}{E_c}\\ \qquad\varepsilon_{cap}^p\left\{1-\dfrac{\tanh\left[\dfrac{\beta l}{2}\right]}{\left[\dfrac{\beta l}{2}\right]}\right\} & (10\cdot a)\\ \langle\sigma_w^{ru}\rangle=-\dfrac{V_m}{V_w}\langle\sigma_m^{ru}\rangle & (10\cdot b)\\ \beta=\dfrac{2\sqrt{2}}{d}\sqrt{\dfrac{G_{mp}/E_w}{\ln(D/d)}} & (10\cdot c)\end{cases}$$

where ε_{cap}^p represents the applied plastic strain and E_c is the Young's modulus of the composites [$E_c=E_m(1-V_w)+E_wV_w$]. Since $E_{mp}<E_m$, clearly, the matrix residual stress decreases upon tensile loading ($\varepsilon_{cap}^p>0$) and increases on compressive loading ($\varepsilon_{cap}^p<0$). The overall changes in the residual stress remain

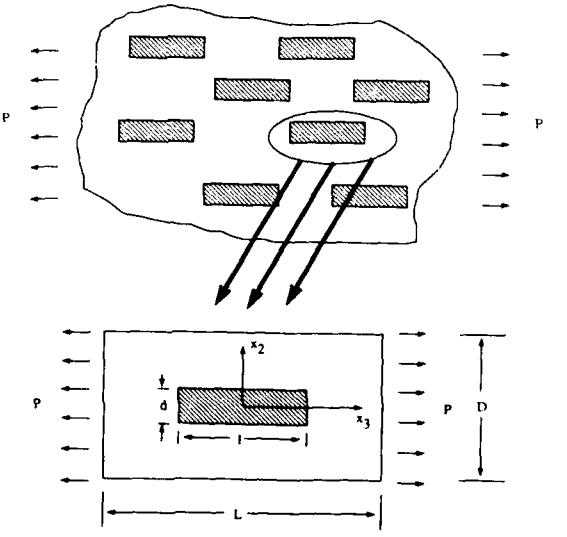

Fig. 10 Schematic diagram for the interface model.

monotonic.

The set of equations stated above applies equally to both cases of compressive and tensile loading provided we consider the transformation:

$\varepsilon_{cap} \longrightarrow -|\varepsilon_{cap}|$

This means that $\langle \sigma_m^{ru} \rangle$ is symmetric about $\langle \sigma_m^r \rangle$ assuming only that plastic deformation is considered. It also can be seen that Eq. (10) is only a function of applied plastic strain which means that elastic strain will not alter the value of the residual stress which contradicts the fact that there is an initial residual stress drop regardless of the loading directions predicted by FEM. It is, therefore, clear that the modified shear lag model cannot adequately predict the effect of the loading directions on the asymmetric behavior of the average residual stress. In other words, the mechanism of load transfer through the matrix-whisker interface cannot have a predominant effect on the average value of the residual stress and the residual stress change and, consequently, on the constitutive behavior. In fact, the outcome of this model matches the results of the finite element analysis given earlier, in that, within the immediate proximity of the longitudinal matrix reinforcement interface, the change of the residual stress is monotonic (Fig. 8). This signifies that the influence of the interface effect is primarily restricted to a very small region in the close vicinity of the whisker-matrix interface and does not significantly influence the bulk of the composite.

The Volume Mismatch Model

In this model (Fig. 11), it will be assumed that when a whisker is embedded in the matrix, no bonding exists between the matrix and the whiskers along the axis of the whisker. Therefore, no load transfer can occur between the whisker and the matrix at their longitudinal interface, and hence the interface effect can be separated from current consideration. On the other hand, full continuity of stress from the matrix to the whisker is assured at the interface of the whisker and the matrix at the tip of the whisker so that the normal stress continuity would be provided. It is further assumed that a boundary is made along the extension of the SiC/Al interface along the whisker's axis to separate the compressive and tensile residually stressed region. Considering that the thermal residual stress is in compression at the tip of the whisker, the material, therefore, may be regarded as being composed of three distinct zones: the region of the matrix which is under tension (denoted by subscripts "mt"), the region of the matrix which is under compression (denoted as "mc") and the whisker zone (denoted by "w"). The combination of the two regions in the matrix (mt + mc) makes up the entire matrix region in the unit cell.

Although the local field in each zone is not uniform, since our interest is the average residual stress, it is often convenient to work with volume averages of the non-uniform field in each zone defined by Eq (11), which is equivalent to Eq. (3) defined in a previous section:

$$\langle \cdot \rangle_{A_n} = \frac{1}{A_n} \int A_n (\cdot) dv \tag{11}$$

where A_n is the area of each zone, i. e., $n = mt$, mc and w.

Considering virtual work and Gauss' theorem, it can be shown that the following relationship exists:

$$\iint_{A_n} \sigma_{ij} dA = \int_{|A_n|} \sigma_{ik} n_k x_j dl \tag{12}$$

i. e.,

$$\langle \sigma_{ij} \rangle_{A_n} A_n = \langle \sigma_{ik} n_k x_j \rangle_{|A_n|} |A_n| \tag{13}$$

where n_k is the normal to the boundary $|A_n|$.

Furthermore, it is a common practice to assume that the average strain ($\langle \varepsilon_{ij} \rangle_{A_n}$) and the average stress ($\langle \sigma_{ij} \rangle_{A_n}$) are related in the same way as in a local field by a set of effective constants[20].

$$\begin{aligned} \langle \sigma_{ij} \rangle_{A_n} &= C^m_{ijkl} \langle \varepsilon_{kl} \rangle_{A_n} && |\langle \sigma_{33} \rangle_{A_n} - \langle \sigma_{11} \rangle_{A_n}| \le \sigma_{ym} \\ \langle \varepsilon_{ij} \rangle_{A_n} &= \varepsilon^0_{ij} + C^{mp}_{ijkl}{}^{-1} [\langle \sigma_{kl} \rangle_{A_n} - \sigma^0_{kl}] && |\langle \sigma_{33} \rangle_{A_n} - \langle \sigma_{11} \rangle_{A_n}| > \sigma_{ym} \end{aligned} \tag{14}$$

where C^m_{ijkl} and C^{mp}_{ijkl} are the stiffness and the tangential stiffness of the matrix, and ε^0_{ij} and σ^0_{ij} are the average strains and stresses on the yield surfaces in the strain and the stress space, respectively.

T. Yano et al.[39] stated that the lateral stress generated by the difference in Poisson's ratio is small with a Al/Al$_3$Ni fiber reinforced eutectic composite system which has a Poisson's ratio of $\nu_f = 0.16$ and $\nu_m = 0.33$. Since a SiC/Al system has a Poisson's ratio of

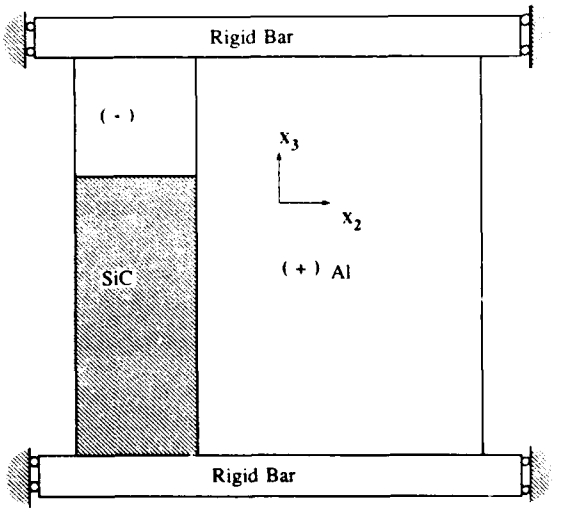

Fig. 11 Schematic diagram for the volume mismatch model.

$\nu_{SiC}=0.19$ vs. $\nu_{Al}=0.33$, we shall adapt their statement. Therefore, if only the longitudinal normal stress is considered, Eq. (14) will reduce to the following:

$$\langle \varepsilon_{33}\rangle_{A_n}=\frac{\langle \sigma_{33}\rangle_{A_n}}{E_m} \qquad \langle \sigma_{33}\rangle_{A_n}\le \sigma_{ym}$$
$$\langle \varepsilon_{33}\rangle_{A_n}=\frac{\langle \sigma_{33}\rangle_{A_n}-\sigma_{ym}}{E_{mp}}+\frac{\sigma_{ym}}{E_m} \qquad \langle \sigma_{33}\rangle_{A_n}>\sigma_{ym} \tag{15}$$
$$A_n=mt,\ mc$$

From the above simplifications, it is easily revealed that the concept of volume mismatch has been reduced to the mismatch between the whisker and the matrix at the whisker end. Because all the quantities we are interested in are along the whisker axis, we may substitute a simpler notation for the element to be investigated, i.e.,

$$\langle \varepsilon_{33}\rangle_{A_n}=\langle \varepsilon_{A_n}\rangle;\ \langle \sigma_{33}\rangle_{A_n}=\langle \sigma_{A_n}\rangle \tag{16}$$

It is clear that Eqs. 12 and 13 define the relationship between average stress over the area of one particular zone and the line average of the stress on the boundary $|A_n|$. Therefore, the global equilibrium condition (equilibrium between zones) can be expressed in terms of volume average stress, and the equilibrium is automatically satisfied when adapting Eq. (13)[37]. Furthermore, during the entire analysis, the continuity condition at the interfaces between zones is satisfied on an average basis.

From the requirement of the condition of equilibrium of stresses, it may be shown that the average residual stress in the whisker is related to the average residual stress in the matrix by the following equation:

$$\langle \sigma_w^r\rangle=-\frac{1-V_w}{V_w}\langle \sigma_m^r\rangle \tag{17}$$

where again, V_w refers to the volume fraction of the whiskers and $1-V_w=V_{mc}+V_{mt}\equiv V_m$ denotes the total volume fraction of the matrix portion. The overall average residual stress in the matrix is, in turn, related to the residual stress in the tensile part of the matrix, $\langle \sigma_{mt}^r\rangle$:

$$\langle \sigma_m^r\rangle=\frac{V_{mt}}{1-V_w}F_w\langle \sigma_{mt}^r\rangle \tag{18}$$

where F_w is defined by:

$$F_w=\frac{V_w}{V_w+V_{mc}}=\frac{V_w}{1-V_{mt}}. \tag{19}$$

It may also be shown that the residual stress in the compressive part of the matrix is given by:

$$\langle \sigma_{mc}^r\rangle=-\frac{V_{mt}}{1-V_{mt}}\langle \sigma_{mt}^r\rangle. \tag{20}$$

Considering the cooling process, it is known that the mismatch of thermal expansion coefficients is large enough to induce plastic deformation around the reinforcement[40]. By considering equilibrium and compatibility, in an average sense, it can be seen that the following equations can be obtained when $|\Delta T_c|\le|\Delta T|<|\Delta T_t|$ (The details of the derivation is shown elsewhere[37]) where:

$$|\Delta T_t|=\frac{\sigma_{ym}\left[(1+F_c)\dfrac{1}{E_m}-\dfrac{1-2V_{mt}}{1-V_{mt}}\dfrac{F_c}{E_{mp}}+\dfrac{V_{mt}}{1-V_{mt}}\dfrac{F_w}{E_w}\right]}{\Delta\alpha F_w}$$
$$|\Delta T_c|=\frac{\sigma_{ym}\left[\dfrac{1}{E_m}\dfrac{1-V_{mt}}{V_{mt}}+\dfrac{F_c}{E_m}+\dfrac{F_w}{E_w}\right]}{\Delta\alpha F_w} \tag{21}$$

Therefore, the thermal residual stress along the longitudinal direction is:

$$\langle \sigma_m^r\rangle=\frac{V_{mt}F_w}{1-V_w}\cdot\frac{\sigma_{ym}\left[\dfrac{1}{E_{mp}}-\dfrac{1}{E_m}\right](1-F_w)+F_w|\Delta\alpha|\,|\Delta T|}{\dfrac{1}{E_m}+\dfrac{V_{mt}}{1-V_{mt}}\left[\dfrac{1-F_w}{E_{mp}}+\dfrac{F_w}{E_w}\right]} \tag{22}$$

This means that within a certain range of temperature variation ($|\Delta T_c|\le|\Delta T|<|\Delta T_t|$), plastic deformation will be introduced in the matrix. However, until $|\Delta T|\ge|\Delta T_t|$, the matrix will remain partially plastically deformed. For $|\Delta T|=773K$, it is both predicted by Eq. (21) and experimentally observed by Vogelsang et al.[41] in terms of generation of dislocations that the matrix is partially plastically deformed. The predicted average residual stress in the matrix is given by Eq. (22).

It is of particular interest to evaluate the new residual stresses in the composite when a uniaxial loading (σ_{ca}) corresponding to the total applied strain (ε_{tot}) is applied along the axis of the whisker (x_3 direction) and is subsequently removed. Clearly, the applied stress changes the residual stress pattern when plastic deformation is involved. If the conditions, as stated before, are such that only portions of the matrix have initially yielded due to the thermal residual stresses, it may be shown that when the applied load is tensile, the overall average residual stress in the matrix after unloading is given by (for derivation details, refer to[37]):

$$\langle \sigma_m^{ru}\rangle=\begin{cases}\langle \sigma_m^r\rangle & \varepsilon_{cap}=0\\ \langle \sigma_m^r\rangle-\dfrac{V_w}{1-V_w}\dfrac{E_wE_m}{(1-F_w)E_w+F_wE_m}\left[\dfrac{\sigma_{ym}}{E_m}-\dfrac{1-\nu_w}{V_w}\dfrac{\langle \sigma_m^r\rangle}{E_m}+\varepsilon_{cap}-\dfrac{\sigma_{ca}}{E_{ce}}\right] & \varepsilon_{cap}\le\varepsilon_{cap1}\\ -\langle \sigma_m^r\rangle-\dfrac{V_w}{1-V_w}\left[\dfrac{E_wE_{mp}(\varepsilon_{cap}-\varepsilon_{cap1})}{(1-F_w)E_w+F_wE_{mp}}-\dfrac{E_wE_m}{(1-F_w)E_w+F_wE_m}\left[\dfrac{\sigma_{ca}}{E_{ce}}\right]\right] & \varepsilon_{cap}>\varepsilon_{cap1}\end{cases} \tag{23-a}$$

where

$$\varepsilon_{cap1}=\frac{1-V_w}{V_w}\left[\frac{2(1-F_w)E_w+2F_wE_m}{E_w}+\frac{1-V_{mt}}{V_{mt}}\right]$$

$$\frac{\langle\sigma_m^r\rangle}{E_m}=\frac{\sigma_{ym}}{E_m} \tag{23·b}$$

and

$$E_{ce}=\frac{(1-V_{mt})E_wE_m}{(1-F_w)E_w+F_wE_m}+V_{mt}E_m \tag{23·c}$$

and E_{ce} represents the all-elasic modulus of the composite in the absence of any plastic thermal residual stresses.

When the applied load is compressive:

$$\langle\sigma_m^{ru}\rangle=\langle\sigma_m^r\rangle-\frac{V_w}{1-V_w}\left[\frac{E_wE_{mp}\varepsilon_{tot}}{(1-F_w)E_w+F_wE_{mp}}-\frac{E_wE_m}{(1-Fw)E_w+F_wE_m}\left[\frac{\sigma_{ca}}{E_{ce}}\right]\right] \tag{23·d}$$

Equation (23) clearly indicates that $\langle\sigma_m^{ru}\rangle$ is no longer a monotonic function. These equations, therefore, predict a non-monotonic change in the residual stresses in the composite depending on whether the system is subjected to a compressive or tensile loading.

By considering applied composite stress (σ_{ca}) and the corresponding composite strain ($\varepsilon_{tot}=\sum_i\varepsilon_{cai}$)

$$\sigma_{ca}=\sum_i E_{ci}\varepsilon_{cai} \tag{24}$$

where E_{ci} is the composite Young's modulus or composite tangential Young's modulus depending on the nature of the applied strain (ε_{cai}), i.e., elastic or plastic, as listed in Table 1. The result is shown in Fig. 12. It is clear, by comparing with Fig. 5, that the most prominent features predicted by the FEM are reproduced by the volume mismatch model.

Using Eq (23), the average values of the residual stress in the matrix were plotted in Fig. 13 after the application of tensile and compressive loadings. For the purpose of comparison, the results of the finite element analysis described before have also been superimposed on the same diagram.

Discussion

The results of the FEM modelling, which have been duplicated by the phenomenological modelling, indicate that the residual stress produced by the ΔCTE and cooling is affected even at initial levels of external deformation. If the deformation is the result of compressive loading, the residual stress at first decreases and then increases with increasing deformation, whereas, if the deformation is the result of tensile loading, the residual stress decreases initially at a rapid rate and the rate slows down upon further

Table 1 Tensile material properties for different constituents of the composites

	Temp (C)	E (10^4 MPa)	ν	σ_y (MPa)	E_p (10^4 MPa)	α (10^{-6})
Al*	0	6.83	3	55.2	2.08	233
	50	6.83	3	55.2	2.08	234
	100	6.83	3	55.2	2.08	234
	250	5.66	3	40.3	1.51	274
	350	4.21	3	14.4	1.13	302
	450	2.76	3	11.6	.8	337
	550	1.10	3	5.5	.4	374
SiC**	All Temp	48.3	19	Elastic	Elastic	038

* Tensile properties of the annealed 6061 Al as a function of temperature were obtained from reference [27]

** Tensile properties of the SiC whiskers were obtained from reference [28]

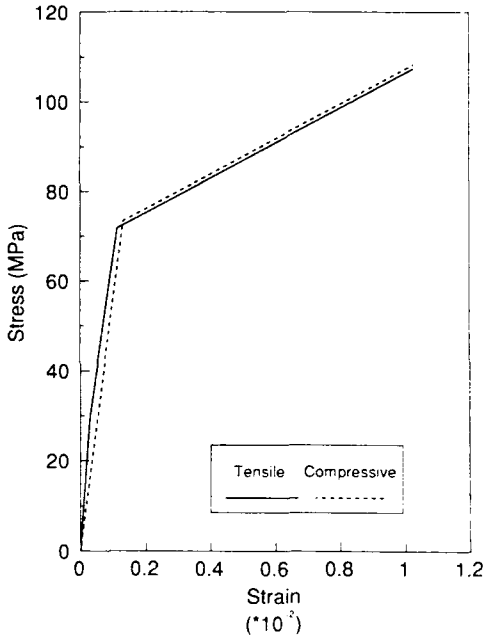

Fig. 12 Stress-strain curves predicted by volume mismatch model which are in general agreement with the FEM prediction shown in Fig. 5.

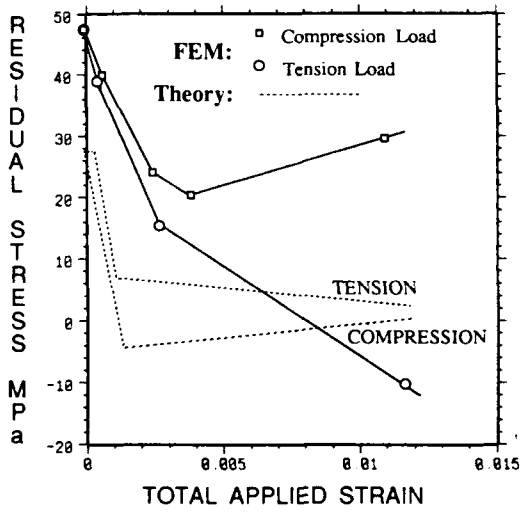

Fig. 13 Comparison of average residual stress predicted by FEM and "volume mismatch" model. Note the similarities of slope change between the two models.

deformation. If the tensile deformation is continued, the residual stress changes sign from tensile to compressive.

From the phenomenological analyses, it is clear that the volume mismatch model gives qualitative agreement with the finite element analysis on the general trend of the residual stress change. Not only the immediate average residual stress drop upon loading is apparent, but the slope change can also be predicted. Note that in the case of compressive loading, there is a sign change in the slope after the composite has started yielding, which could not be predicted by the interface model. Furthermore, by comparing Figs. 4 and 12, the constitutive behaviors of the composite predicted by FEM and the volume mismatch model are generally in agreement.

To understand the underlying mechanism for the change in residual stress, it is helpful to retrieve the argument of weighted residual stress discussed in section II. Since the ratio of the simple average stress over the weighted average stress is greater than 1 (1.55), this means that the magnitude of the weighting factor (stress rate $\partial\sigma_{33}/\partial q$) is greater in the compressive region. This is equivalent to stating that in order to maintain compatibility between the whisker tip region of the matix and the rest of the matrix, the compression zone at the whisker tip will respond faster than the rest of the matrix, i. e., higher stress (strain) rate, and result in localized plastic deformation before global yield. This local stress (strain) rate gradient will, therefore, explain the pre-global-yield residual stress rearrangement which is represented by the initial residual stress drop (Fig. 13).

It is also interesting to note that the current Eshelby method does not predict such a residual stress reduction after an initial prestrain. Withers et al.[20] in their recent mean field investigation implied that the residual stress stays as a constant within a pre-global-yield region and that there is an overall monotonic change in residual stress as a result of prestraining. The discrepancy lies in that, first, in the mean field theory, the yielding criteria is satisfied in an average sense. However, well before the average global yielding criteria is satisfied, localized micro-yielding has already occurred, e. g., at the whisker end, as pointed out previously, and incompatibilities between different parts of the matrix which are responsible for the generation of the matrix residual stress have already developed. Therefore, residual stress alteration is induced prior to the global yielding. However, by considering only a global average field, such localized microplastic deformation can not be taken into account. Secondly, the ratio of simple average stress over average stress weighted by the initial stress rate gives a value of 1.55, a 55% deviation from unity. This indicates that there is a high gradient in the initial deformation field which means that, in this particular case (with a large deformation gradient within the matrix phase) the assumption of uniform plastic strain before and at the onset of the global plastic deformation is probably unsubstantiated. Such an assumption may be employed at the post-yield region. In fact, if the initial non monotonic behavior of the change of the residual stress is set aside, the latter portion of the residual stress as a function of applied strain at higher strain value is largely monotonic.

In the post yield region, it is worthwhile to point out that in the case of compressive loading, there is a sign change in the slope $\partial\langle\sigma_m^r\rangle/\partial\varepsilon_{Total}^A$ after the yielding of the composite yielding, which is predicted by both FEM and the volume mismatch composite model. This is an indication that due to plastic deformation, the deformation gradient across the tension and compression zones in the matrix becomes totally different in order to maintain the deformation compatibility. The initial compressive load will produce a geometric compromise between tension and the compression zone, and therefore, there will be a reduction in residual stress. After the matrix material has begun deforming plastically throughout, the two zones become more and more imcompatible as the compressive load increases followd by unloading and, as a result, the residual stress will increase again. It is also important to point out that while the tendency of residual stress change is in agreement with both FEM and volume mismatch models, the actual magnitude of the residual stresses predicted by the analytical model is much smaller than that predicted by the FEM and the relative positions between tension and compression curves predicted by FEM, are not in agreement with the volume mismatch model. It is speculated that the absence of interfacial bonding in the volume mismatch model is the key reason for the discrepancy. For example, the discrepancies of relative positions of the curves of residual stress after tension or compression between the FEM and volume mismatch can be explained by the fact that the effect of the interface will enhance the initial residual stress drop when under an external tension load, and oppose such a drop when under compression. Such an effect can be verified easily through Eq (10), which is directly derived from shear load transfer. However, the pattern of the residual stress changes is solely determined by the volume mismatch mechanism.

Conclusion

In summary :

(1) The predicted change of the average residual

stress is not monotonic with respect to the applied pre-stress (strain), i.e., regardless of the sign of the loading. The average residual stress drops upon the initial elastic deformation, and it will increase or decrease depending on whether the loading history is compressive or tensile.

(2) The results predicted by FEM are generally comparable to that predicted by the theoretical model which is based on the volume mismatch between the reinforcement and the matrix. This indicates that the volume incompatibility is the controlling factor regarding the change in residual stress.

Acknowledgement

This reseach was supported in part by the Office of Naval Research under Contract N00014-85-K-0007. The authors wish to acknowledge the continued support and encouragement of Dr. S. Fishman of the Office of Naval Research. The authors would also like to thank Prof. C. Schwartz of the University of Maryland for his encouragement in using the ADINA program and the Computer Science Center of the University of Maryland for its support of computer time.

References

(1) Arsenault, R. J. and Wu, S. B. *Materials Science and Engineering*, Vol. 96, 1987, p. 77.
(2) Cao, H. C., Thouless, M. D. and Evans, A. G., *Metallurgica*, Vol. 36, No. 8, 1988, pp. 2037-2046.
(3) Y. Flom and R. J. Arsenault, *Acta Metallurgica*, Vol. 37, 1989, p. 2413.
(4) Mura, T. and Taya, M., in *Recent Advances in Composites in the United States and Japan*, J. R. Vinson and M. Taya, Eds., ASTM, STP 864.
(5) Dvorak, G. J. and Rao, M. S. M., *Journal of Applied Mechanics*, Vol. 98, No. 4, Dec. 1976, p. 619-624.
(6) Garmong, G., Metallurgical Transactions S, Oct. 1974, p. 2183-2190.
(7) Takao, Y., *Journal of Composite Materials*, Vol. 21, No. 2, Feb. 1987, p. 140 156.
(8) Hoffman, C. A., *Journal of Engineering Materials*, Vol. 1, 1974, p. 55-62.
(9) Levy A. and Papazian, J. M., *Metallurgical Transactions*, Vol. 21A, Feb. 1990, p. 411-420.
(10) Dutta, I. and Bourell, D. L., *Journal of Composite Materials*, Vol. 22, Sept. 1988, p. 829-849.
(11) Christman, T., Needleman, A. and Suresh, S., *Brown University Report No. NSF-ENG-8451092-1-89.*
(12) Flow, E. C., *Military Application*, Sept. 1988, p. 1-5.
(13) Arsenault, R. J., Shi, N., Feng, C. R. and Wang, L., Submitted to *Materials Science and Engineering.*
(14) Aboudi, J., *Solid Mechanical Archives, 11/3* 1986, p. 141-183.
(15) Teply, J. and Dvorak, G. J., *Journal of Mechanical Physical Solids*, Vol. 36, No. 1, 1988, p. 29-58.
(16) Tvergaard, V., *Acta Metallurgical Materials*, Vol. 38, No. 2, 1990, p. 185-194.
(17) Tandon, G. P. and Wong, G. J., *Journal of Applied Mechanics*, Vol. 55, March 1988, p. 126-135.
(18) Clegg, N. J., *Acta Metallurgica*, Vol. 36, No. 8, 1988, p. 2141-2149.
(19) Arsenault, R. J. and Taya, M., *Acta Metallurgica*, 35, 1987, p. 651.
(20) Withers, P. J., Stobbs, W. M., Pedersen, O. B., *Acta Metallurgica*, Vol. 37, No. 11, 1989, p. 3061-3084.
(21) Eshelby, J. D., *Proceedings of the Royal Society*, Vol. 241A, 1957, p. 376.
(22) Eshelby, J. D., *Proceedings of the Royal Society*, Vol. 252A, 1959, p. 561.
(23) Takao, Y. and Taya, M., *Journal of Composite Materials*, Vol. 21, 1987, p. 140.
(24) Papazian, J. M. and Adler, P. N., *Metallurgical Transactions A*, Vol. 21A, 1990, p. 401-410.
(25) Arsenault, R. J., *Materials Science and Engineering*, Vol. 64, 1984, p. 171-181.
(26) McDanels, D. L., *Metallurgical Transactions A*, Vol. 16A, June 1985, p. 1105.
(27) ALCOA (Aluminum Company of American) Aluminum Handbook, 1967.
(28) Mahan, R. L. and Herzog, J. A., "Whisker Technology", J. Wiley-Interscience, New York, NY, 1970.
(29) Ledbetter, H. M. and Austin, M. W., *Materials Science and Engineering*, Vol. 89, 1987, p. 53.
(30) Majumdar, S., Kupperman, D. and Singh, J., *Journal of the American Ceramics Society*, Vol. 71, (10) 1988, p. 858.
(31) Pedersen, O. B., *Acta Metallurgica*, Vol. 31, No. 11, 1983, p. 1795-1808.
(32) Sato, N., Kurauchi, T., Sato, S. and Kamigaito, O., *Journal of Composite Materials*, Vol. 22, Sept. 1988, p. 850-873.
(33) Cox, H. L., *Journal of Appled Physics*, Vol. 3, 1952, p. 72.
(34) Nairn, J., *Journal of Composite Materials*, Vol. 22, June 1988, p. 561-587.
(35) Nardone, V. C. and Prewo, K. M., *Scripta Metallurgica*, Vol. 20, 1986, p. 43-48.
(36) Taya, M. and Arsenault, R. J., *Scripta Metallurgica*, Vol. 21, 1987, p. 349-354.
(37) Shi, N. Ph. D. thesis, University of Maryland.
(38) Kelly, A., *Strong Solid*, 2nd Ed., Clarendon Press, Oxford, 1973.
(39) Yano, T., Yanagisawa, O. and Ohmori, M., *Metallurgical Transactions*, JIM, Vol. 30 (5), 1986, p. 345-353.
(40) Arsenault, R. J. and Shi, N., *Materials Science and Engineering*, Vol. 81, 1986, p. 175-187.
(41) Vogelsang, M., Arsenault, R. J. and Fisher, R. M., *Metallurgical Transactions A*, Vol. 17A, 1986, p. 379-389.

Transient and Residual Stress in Porcelain/Alloy Strip for Dental Use as Affected by Tempering*

Kenzo ASAOKA**

Porcelain-fused-to-metal (PFM) restorations may develop cracks during processing or in-mouth service if the relative physico-mechanical properties of the porcelain and alloy are highly mismatched. The precise conditions when it might occur are not known. Many processing and property variations can affect the stresses developed throughout a porcelain-alloy system. To understand this, a computer simulation of stress in a PFM strip was conducted. The simulation considers cooling from temperatures higher than the porcelain sag point. The following temperature-dependent factors were incorporated : the elastic modulus, shear viscosity (porcelain), and coefficient of thermal expansion. Cooling rates during tempering of porcelain were measured. The cooling rate dependencies of the glass transition temperature and temperature distribution during cooling were also included in the simulation. The results suggest that tempering with a high cooling rate make up for compressive residual stress in body porcelain and the high curvature of the composite beam.

Key Words: Biomaterials, Laminated Construction, Residual Stress, Thermal Stress, Viscoelasticity, Transient Stress

1. Introduction

Porcelain fused-to-metal (PFM) restorations were presented to the dental profession about three decades ago. This technological advance precipitated a change to the era of full coverage restorations that serve both the functional and cosmetic requirements of patients with carious, disfigured, or missing teeth. PFM restorations consist of a cast metal coping onto which a porcelain veneer is fired. With this technique, opaque porcelain is fused against the casting to mask the metal. The opaque is heavily loaded with metallic oxide opacifiers and may be applied with a thickness of 0.1 to 0.2 mm. Since the opaque porcelain is reflective, it must be covered with at least 1 mm of body porcelain if reasonable esthetics are to be achieved.

Currently, the use of PFM restorations represents a significant component of dental restorative practice. However, the dental practitioner has been faced with the clinical problem of occasional failure of the porcelain-alloy system during function ; a problem of small magnitude in terms of the frequency of occurrence, but of serious consequence when it does occur. Failures can be attributed to a variety of clinical, processing and material system deficiencies. With the continuous presentation of more and different types of alloys and porcelains for use by the dental profession, it becomes of increasing clinical importance to assess their compatibility with existing problems.

For this study, a computer simulation using a viscoelastic stress analysis was developed to clarify the effect of tempering and thermal expansion of alloy on transient and residual stresses in the PFM strip.

2. Materials and Methods

2.1 Cooling rate

The powder of the porcelain was formed into a cylindrical shape (5.0 mm in diameter and 10.0 mm in length) in a steel die by dry-pressing. Thermocouples of 0.13 mm in diameter were embedded in the porcelain compacts. The porcelain was fired according to the manufacturer's recommended procedure. After firing once in a furnace, the porcelain was reheated to

* Received 19th November, 1990

** School of Dentistry, Tokushima University, 3-18-15 Kuramoto-cho, Tokushima 770, Japan